# Università degli Studi di Napoli *Federico II*

DOTTORATO DI RICERCA IN

## FISICA

**Ciclo XXX**

Coordinater: prof. Salvatore Capozziello

## THz Time-Domain Spectroscopy of Ionic Liquids and THz-Pump/Second-Harmonic-Probe Experiment in Solids

## By Sen Mou

Settore Scientifico Disciplinare: FIS/01

Year 2014/2017

# Abstract

THz indicates an electromagnetic wave whose spectrum locates between the microwave and infrared range. In the last two decades the advent of benchtop THz sources filled the so-called 'THz gap'. The properties of THz radiation such as low photon energy, transparence to it of packaging materials and so on make it suitable for many applications in industrial and scientific fields. In this work we generated intensive broadband THz pulses radiated from femtosecond laser induced plasma via four-wave-mixing process coupling fundamental laser light and its second harmonic.

In chapter 1 we generally introduce the principles of THz generation and detection. We also introduce the application of our THz source in static THz time-domain spectroscopy and time-resolved THz spectroscopy.

In chapter 2 we present THz generation based on air plasma and THz detection through different methods and sensors, including ZnTe, GaSe, LAPC single crystals and air-based methods. The results show that the detected upper frequency edge with 500 µm ZnTe is limited by the phase mismatch between THz and probe beam. 250 µm ZnTe expands the detected frequency range but the detection efficiency is restricted by phonon absorption at 5.3 THz. GaSe can detect THz up to 30 THz with a deep gap due to phonon mode around 6.5 THz. Another dip around 19.1 THz due to silicon absorption is also found. LAPC is capable of measuring THz up to around 17 THz without gap. The air-based method results in ultra-broadband detection of short unipolar pulses.

In chapter 3 we develop a precise contactless micro-distance measurement method based on THz pulses. The resolution of the measurement can achieve 1.5 µm with scanning step equal to 0.01 ps. A comparison between ZnTe detection sensor and air-based sensor indicates that the air-based detection technique has advantages that include the ability to measure smaller distance and the immunity to distortion introduced by vapor absorption in air. We also compare distance measurement with ZnTe in air and in nitrogen. We find that the measurement in nitrogen leads to a more straightforward extraction of the distance as compared to the measurement in air

where additional analysis is needed to take into account the coherent oscillations produced by air absorption.

In chapter 4 we investigate the mixing behavior of the dielectric function of mixtures of ionic liquids (ILs). In the investigation we measure the cell thickness with the method developed in chapter 3 and detect the THz radiation with electro-optic sampling in a 250 μm ZnTe crystal. The results show that the complex permittivity of ionic mixtures obeys linear mixing law. We also find that all the complex permittivity spectra of mixtures can be simulated with a combination of three oscillators which are assigned to different vibrational modes of the ionic liquids.

In chapter 5 we discuss broadband THz time-domain spectroscopy applied to pure imidazolium-based ionic liquids. The broadband THz detection was realized thanks to the use of a LAPC crystal. We find in the absorption spectra of a series of pure ionic liquids clear signatures of both inter- and intra-molecular vibrational modes. This is the first time that inter- and intra-molecular modes of ionic liquids are measured in one shot without combining different techniques. We have assigned these vibrational modes to different processes in ionic liquids. We find an interesting correlation between the specific anion of IL and the peak frequency shift and bandwidth variation observed for the intermolecular absorption band. We discuss these correlations in terms of the ability of the specific anion in forming hydrogen bonds.

In chapter 6 we discuss our experiments of THz-pump/second-harmonic-generation in single crystals of quartz. The experiments on quartz show that the second harmonic signal oscillates coherently at several frequencies in the THz frequency range and these oscillations depend on the specific combination of the probe and THz linear polarization, and orientation of quartz axis. We also find that the intensity and bandwidth of the spectrum of second harmonic are enhanced in presence of the THz, i. e., side-bands appears in the second harmonic spectrum.

# Publications

## Publications Covered in This Thesis

1. **Sen Mou**, Andrea Rubano and Domenico Paparo, "Complex Permittivity of Ionic Liquid Mixtures Investigated by Terahertz Time-Domain Spectroscopy", The Journal of Physical Chemistry B vol. 121, 7351-7358 (2017).

2. **Sen Mou**, Andrea Rubano and Domenico Paparo, "Broadband Terahertz Spectroscopy of Imidazolium-Based Ionic Liquids" (submitted to The Journal of Physical Chemistry B)

3. **Sen Mou**, Andrea Rubano and Domenico Paparo, "Micro-distance measurement using THz and application in THz Time-Domain spectroscopy of liquids" (In Preparation)

## Other Publications

1. Andrea Rubano, **Sen Mou** and Domenico Paparo, "Monitoring the interfacial electric field in pure and doped SrTiO3 surfaces by means of phase-resolved optical second harmonic generation" Optics and Lasers in Engineering (published online)

## Conference Paper:

1. **Sen Mou**, Andrea Rubano and Domenico Paparo, "A new THz-Pump /Second Harmonic Probe experimental setup: characterizations and first results", 2016 Fotonica AEIT Italian Conference.

# Content

# List of Tables

# List of Scheme

# List of Figure

# Chapter 1.  Introduction and Overview

## 1.1.  GENERAL INTRODUCTION

Terahertz (THz) indicates electromagnetic radiation whose spectrum is located between the microwave and far infrared range. The THz frequency band is usually referred to the range from ~0.1 to 10 THz[1]. As generation of THz is challenging for both electronic and photonic technologies this interval of frequencies has been known as 'THz Gap'[2] and often described as the final unexplored spectral range. However, this gap has been filled up within the last two decades with the advent of benchtop THz sources based on femtosecond laser. With photon energy in the range from ~1 to ~100 millielectronvolt (meV) THz strongly interact with physical processes whose typical lifetime is in the picosecond range and those whose energy is in meV range. Examples of such processes and systems include phonons in crystalline solids[3], relaxation dynamics in aqueous liquids[4-6], weekly bonded molecular crystals[7-10], transient molecular dipoles[11], excitons[12-15], bound electrical charges[16], free charge plasmas[17-19] and so on.

## 1.2.  THZ SOURCE AND DETECTION

### 1.2.1. Generation

Femtosecond laser based THz radiation can be realized using photoconductive antennas[20-23], electro-optic materials such as ZnTe[24-25], DAST (4-dimethylamino-N-methyl-4-stilbazolliumtosylate)[26-28] and LiNbO$_3$[29-32]. In addition, THz can be produced in air[33-39]. A THz source can be based on oscillator or amplifier lasers. Photoconductive antennas are usually used in oscillator-based THz source and cannot be used with amplifier since high pulse energy delivered by amplifiers can damage photoconductive antennas[2]. In contrast, electro-optic materials are usually used in amplifier-based THz sources and the laser oscillator isn't powerful enough as nonlinear electro-optic effects are generally too weak. ZnTe is the most common electro-optic material since the mismatch of group velocity between optical and THz pulse is relatively low in ZnTe[2]. Tilted-front THz generation has been proposed to match the group velocity in LiNbO$_3$

to generate high energy THz pulse[31-32]. Broadband and intensive THz pulse has been created in air[35, 39-40].

Continuous THz wave can be generated based on beam beating scheme in biased semiconductor photomixers[41]. Two laser beams whose wavelengths are $\lambda_1$ and $\lambda_2$ can generate electromagnetic wave having frequency of $\nu = c|1/\lambda_1 - 1/\lambda_2|$ , which is the beating frequency of the exciting lasers. The beating frequency can fall in the THz range by selecting proper laser sources. Continuous THz wave can be radiated into free space by connecting properly designed antenna to photomixer. Constable and Lewis[42] measured the optical parameters of ZnTe by applying continuous THz wave radiated by gallium-arsenide / low-temperature-grown gallium-arsenide heterostructure.

### 1.2.2. Detection

Field-resolved detection of THz can be realized by electro-optic sampling. The detection of THz pulse can be seen as the inverse process for THz generation. Field resolved detection was first demonstrated independently in 1995 by three groups utilizing $LiTaO_3$[43-44] and poled polymer[45] as electro-optic media. Subsequently, ZnTe was introduced since it can effectively address the problem of phase mismatch[46].

ZnTe shows good phase match up to a few THz in generation and detection but its application in higher frequency range is limited by strong phonon absorption at 5.3THz[47-48]. One method to expand THz spectrum is to use nonlinear optical material in which phonon absorptions appear in higher frequency region. With GaP[49] it is possible to expand THz spectrum up to 7-8 THz. In order to generate and detect THz with even higher bandwidth, thinner nonlinear crystals are necessary to achieve phase match all over the entire broad band. However, thinner crystals lead to smaller electro-optic response and result in complications due to multiple reflections of THz in crystals[41]. Generation and detection of THz transients with bandwidth exceeding 30 THz was demonstrated in thin ZnTe crystals whose thickness is less than 30 $\mu m$ [50]. Detection of THz generated in a 90-mm-thick Z-cut GaSe crystal beyond 41 THz was reported later with a 10.3- $\mu m$ -thick <110> ZnTe crystal optically contacted to 200- $\mu m$ thick <100> ZnTe substrate[51]. Generation and detection beyond 100 THz was

demonstrated by combining laser pulse shorter than 10 fs and thinnest nonlinear crystals[52].

## 1.3. **THZ SPECTROSCOPY**

### **1.3.1.** Terahertz Time-Domain Spectroscopy

With THz it is possible to conduct static terahertz time-domain spectroscopy (THz-TDS) and transient THz spectroscopy. THz-TDS [53]can be carried out with transmission and reflection configuration. Furthermore, THz-TDS can also be conducted by applying the technique of attenuated total reflection (ATR) in the THz range. In a reflection configuration the reference signal can be recorded by replacing the sample with reflector such as dielectric and metallic surfaces. Reference signal can also be recorded by contacting a window to the sample. With the latter method, the THz beam reflected by the front surface of the window is used as reference and the THz reflected from the interface between the sample and the sample itself is used as sample signal. Jeon et al.[54] measured complex conductivity of n-type GaAs and n-type Si wafer using as reference the signal reflected by an aluminum mirror at the positon of the sample. Thrane et al.[55] investigated temperature-dependent far-infrared spectrum of water using the signal reflected from air-silicon interface as reference.

ATR THz-TDS can be implemented with a silicon dove prism. ATR THz-TDS is well compatible with transmission THz-TDS as silicon Dove prism can be directly put at the focal region of THz-TDS setup in transmission geometry, thus only resulting in minimal disturbance of the THz beam path. In the configuration of ATR THz-TDS, THz is totally reflected at the top surface of the prism. The sample is placed on this surface. Optical constants can be calculated by comparing the signal reflected from the interface in contact with sample and that in contact with air. In 2004 Hirori et al.[56] proposed the method of ATR THz-TDS and applied it to measure complex dielectric constants of InAs and liquids. Nagai et.al.[6] measured dielectric constants of distilled water and sucrose solution with ATR THz-TDS.

In crystalline materials THz properties are determined by long-range order. In polar liquids the THz spectrum is dominated by the relaxation of permanent dipoles,

while by collision-induced dipole moments in nonpolar liquids[41]. THz-TDS can be applied to investigate lattice modes in polyatomic and molecular crystals. Potential application of the scientific achievements in this field is to recognize dangerous and/or illicit chemicals with compact and portable THz-TDS instruments. Meanwhile, THz-TDS can unveil the relaxation of dipoles in liquids which is of great importance to chemical and biological processes[57-58].

### 1.3.2. Time-resolved THz Spectroscopy

Time-resolved THz spectroscopy (TRTS) is a powerful technique to characterize ultrafast dynamics occurring on time scale from femtosecond to nanosecond. One type of TRTS is time-resolved THz emission spectroscopy[59]. With this method, the THz waveform radiated from optically excited sample is analyzed to reveal the underlying physical processes. Hirakawa et. al.[60] characterized the decay time of optically exited plasma oscillations in A1GaAs/GaAs heterojunctions by time-resolved THz emission spectroscopy and suggested that non-equilibrium hot 2-dimensional plasmon modes relax trough strong carrier-carrier interactions. Roskos et. al.[61] unveiled electromagnetic wave radiated by coherently oscillating electrons in coupled-quantum-well semiconductor structure. With time-resolved THz emission spectroscopy it is also possible to characterize dynamics of cooper pair in high transition temperature superconductors[62].

Another type of time-resolved THz spectroscopy is optical pump / THz probe. The first of such experiments was conducted in 1986 by Nuss and co-workers[63] to investigate the transient photoconductivity in GaAs. With optical pump / THz probe it is possible to map out THz waveform at different delay times of photonic excitation. Zielbauer et al.[64] investigated dynamics of optically excited carriers in silicon with optical pump / THz probe spectroscopy at various temperatures and they deduced carrier scattering rate by comparing experimental and theoretical numerical results. Beard et al.[65] investigated the onset and decay of photoconductivity in bulk GaAs with TRTS and found the electron mobility obtained by fitting the experimental data to a modified Drude model agrees with the value in literatures. Beard et al. also demonstrated that TRTS is a contactless electrical probe with subpicosecond

resolution. Averitt et al. [66] revealed optically induced two-component relaxation in $La_{0.7}M_{0.3}MnO_3$ thin films (M=Ca, Sr). They also found the lifetime of the slower component relating to spin-lattice relaxation increases as temperature approaches $T_C$.

# Chapter 2. Experimental Setup and THz Detection

## 2.1. **INTRODUCTION**

Through the ionization and a nonlinear optical process, ambient air is capable of generating terahertz (THz) electromagnetic field strengths greater than 1 MV/cm, useful bandwidths of 30 THz or more (the bandwidth is solely limited by the pulse duration) and highly directional emission patterns[33-34, 38]. The band including those frequencies was historically termed the "THz gap," due to the relative difficulty of generating and detecting this elusive electromagnetic radiation, which lies at the borders of the two realms of Electronics and Optics. Laser-induced air-plasma can be used to generate THz waves through a four waves mixing optical process and the air can be used as well as a THz wave-sensor by means of a technique termed THz Air Biased Coherent Detection (THz-ABCD)[67-72]. Both processes are based on the third-order non-linear wave sources described in Eq.(2-1) and Eq.(2-3) as follow.

$$P_i^{NL}(\omega_{THz}) = \chi^{(3)}{}_{ijkl} \cdot E_j(2\omega) \cdot E_k(\omega) \cdot E_l(\omega) \qquad (2\text{-}1)$$

with

$$\omega_{THz} = 2\omega - \omega - \omega \qquad (2\text{-}2)$$

$$P_i^{NL}(2\omega) \approx P_i^{NL}(2\omega \pm \omega_{THz}) = \chi^{(3)}{}_{ijkl} \cdot E_j(\omega_{THz}) \cdot E_k(\omega) \cdot E_l(\omega)$$

$$= \chi^{(2)}{}_{eff} \cdot E_k(\omega) \cdot E_l(\omega) \qquad (2\text{-}3)$$

where **P**$^{NL}$ is the non-linear polarization vector oscillating at THz frequency $\omega_{THz}$ or at frequency of $2\omega \pm \omega_{THz}$, which is approximately equal to $2\omega$ as $\omega_{THz}$ is much smaller compared to $\omega$. **χ**$^{(3)}$ is the 3$^{rd}$ order susceptivity of air, **E** is the optical electric field and **χ**$^{(2)}_{eff}$ = **χ**$^{(3)}$·**E**($\omega_{THz}$) is the effective 2$^{nd}$ order susceptivity induced in centro-symmetric materials (such air) by the presence of an electric field, a mechanism often called Electric Field Induced Second Harmonic Generation (EFISH). THz radiation can serve as a unique tool for non-invasive material classification, particularly since it easily penetrates many optically opaque materials such as paper, plastics, and clothing.

More recently, the ability to generate very intense sources with peak $E_{THz}$ of the order of 1 MV/cm as in our case, opened the route to the use of the THz pulse to actively induce low-energy excitations in solids, as for instance spin waves in anti-ferromagnets[73], or to trigger ultrafast phase transitions in oxides[74].

In this chapter, we report an intense THz generation setup capable of carrying out THz pump experiment. We characterized the system with two ZnTe crystals of different thickness, 30 µm GaSe, air sensor and LAPC[75-77], which is an electro-optic polymer film made from Lemke (2-(3-(2-(4-dialkylaminophenyl) vinyl)-5, 5-dimethylcyclohex-2-enylidene) malononitrile) and APC (poly (bisphenol A carbonate-co-4, 4'-(3, 3, 5-trimethylcyclohexylidene) diphenol carbonate)). Lemke and APC are respectively a dye molecule and an amorphous polycarbonate. In the following the different methods are tested and compared.

## 2.2. EXPERIMENT SETUP
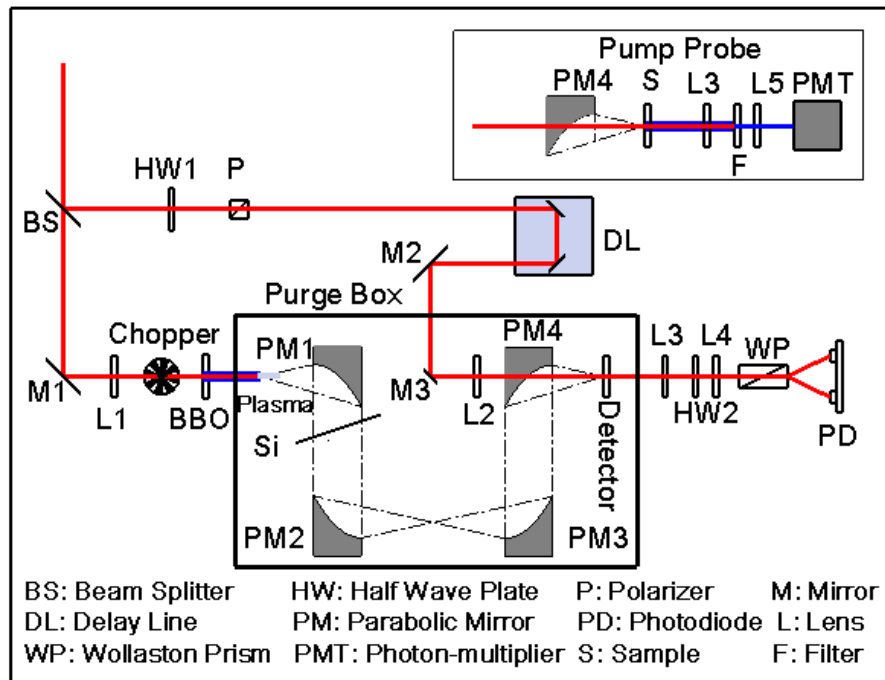


**Figure 2-1.** Experimental setup of high-field broadband THz spectrometer. Main panel: electro-optic detection with ZnTe, GASe and LAPC. Inset: EFISH detection and THz-pump / SHG-probe configuration.

The experimental setup is schematically depicted in **Figure 2-1**. In the setup, a regenerative amplified Ti: sapphire laser system (Coherent Legend), delivering linearly polarized pulses with duration time around 35 fs and central wavelength at 800 nm, was used to generate and detect THz radiation.

The power of the laser is 3.7 W and repetition rate is 1 kHz. The laser is split into pump and probe beams by an 80 / 20 beam splitter. The stronger pulse is used as pump and the other one is used as probe. The pump is focused by a 200mm lens and a Beta Barium Borate (BBO) crystal is inserted between the focus and the lens, so to generate the doubled frequency pulse. The pump pulse is modulated at 500 Hz by a mechanical chopper, mounted between the lens and the BBO, in order to have a signal every second pulse.

At the focus, air plasma is created by the pump pulse and the THz wave is radiated by the plasma. Subsequently, the THz is collected and collimated by a 90° off-axis parabolic mirror (PM). The idle pump beam is blocked by a silicon wafer situated in the THz beam between PM1 and PM2. The THz then is directed to PM4 by the third mirror PM3 for the detection. The THz is focused by PM4 and propagates collinearly with the probe beam to the detection point. In order to obtain absorption-free spectra, all the THz path is covered by a purge-box, which is supplied by continuous nitrogen flow to avoid water vapor absorption. In the probe beam path, a half wave plate and a polarizer cube are inserted to adjust the power of the probe. Then the probe is routed to a retroreflector mounted on a delay line and focused by a lens to the same point as the focus of PM4. In the main panel of **Figure 2-1**, the THz is detected by a detector which can be ZnTe crystal, GaSe crystal or LAPC. However, the THz can also be detected by the air itself. With the crystal detection method, the detection crystal is mounted at the focus of PM4. The probe passing through the crystal is collimated by a lens and then passes through a Wollaston prism which splits it into two beams. The split beams are finally detected by a pair of balanced photodiodes. When the THz is detected by air sensor, the THz generation part remains the same and the only difference is the detection part. The detection subsystem for air sensor is constituted by a blue-filter, a monochromator and a photon-multiplier as depicted in the inset of **Figure 2-1**.

## 2.3. **THZ DETECTION**

### **2.3.1.** THz Detection with ZnTe
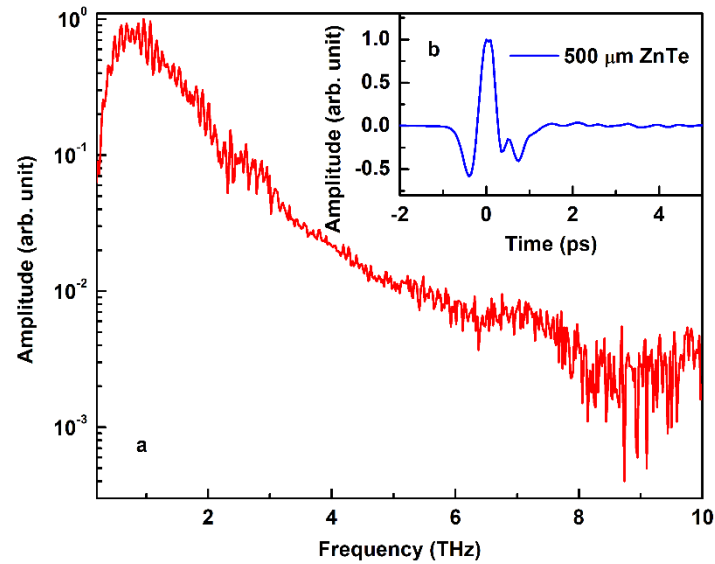


**Figure 2-2.** THz EO-detection with 500 μm ZnTe crystal. The FFT spectrum is shown in the main panel, the pulse temporal profile is shown in the inset.
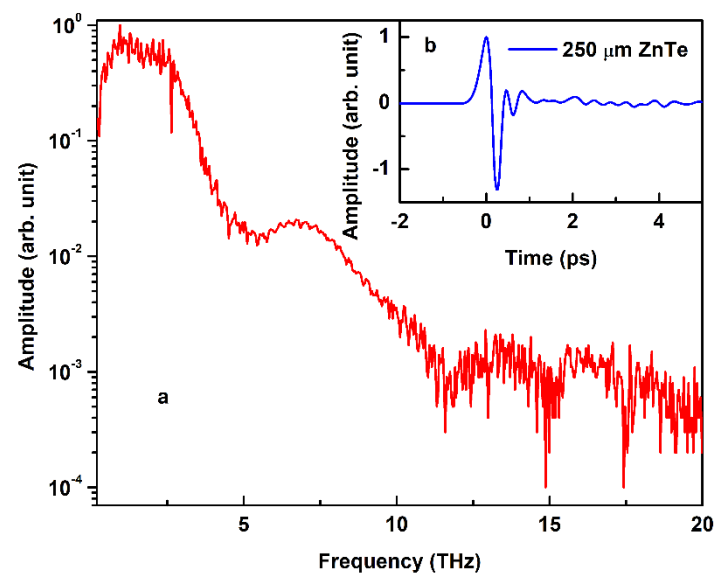


**Figure 2-3.** THz EO-detection with 250 μm ZnTe crystal. The FFT spectrum is shown in the main panel, the pulse temporal profile is shown in the inset.

The power of the THz radiation was found to be ~150 µJ, as measured with a commercial THz power sensor, and the corresponding peak electric field amplitude was estimated to be 1 MV/cm. **Figure 2-2** shows the Fourier transformation of the THz pulse detected with 500 µm ZnTe. The detected THz pulse in time domain is shown in the inset. It is possible to observe that the distinguishable upper frequency band-edge is ~8 THz. The sample interval is 0.05ps, enough since after 8 THz the signal drops to noise floor. Consequently, we can sample the THz pulse with larger sampling time interval. It is necessary to reduce the sampling time interval when the signal spectrum is higher, which is the case for all the other detectors.

**Figure 2-3** shows the Fourier transformation of the THz pulse detected with 250 µm ZnTe crystal, using sampling time of 0.02 ps. The detected THz pulse in time domain is shown in the inset. It is seen that the distinguishable upper frequency band-edge is 15 THz and there is a dip around 5.3 THz[47-48]. This dip can be assigned to the well-known transverse optical phonon absorption in the ZnTe detection crystal. The spectrum band is almost the double of that detected with 500 µm ZnTe. However, the spectrum width detected with 250 µm ZnTe is still narrow when comparing with the result reported in literature with the ABCD method[68]. The detected spectrum width can be broadened by reducing the thickness of the sensor crystal as shown in Ref. [[51]]. The limited distinguishable spectrum with thick ZnTe is due to the phase mismatching of the probe laser and THz wave inside the crystal.

## 2.3.2. THz Detection with GaSe

**Figure 2-4** show typical detection result with Z-cut GaSe having 30 µm thickness. The surface of the crystal is tilted around 45 degrees with respect of incident collinearly propagating THz and probe beams. As shown in panel (b) of **Figure 2-4**, the detected THz band is expanded over 30 THz with two obvious dips around 6.5 and 19.1 THz. The dip around 6.5 THz probably stems from of phonon absorption and that around 19.1 THz from absorption of silicon wafer. Chen et al.[78] observed an intensive absorption band in GaSe in the range from ~ 6 to ~ 8 THz. It is also worth noting that the sensitivity and detected band depend on the angle between probe and crystal

surface. Liu et al.[79] investigated the influence of the tilted angle on THz detection with GaSe. Here we only show the typical result obtained in our lab.
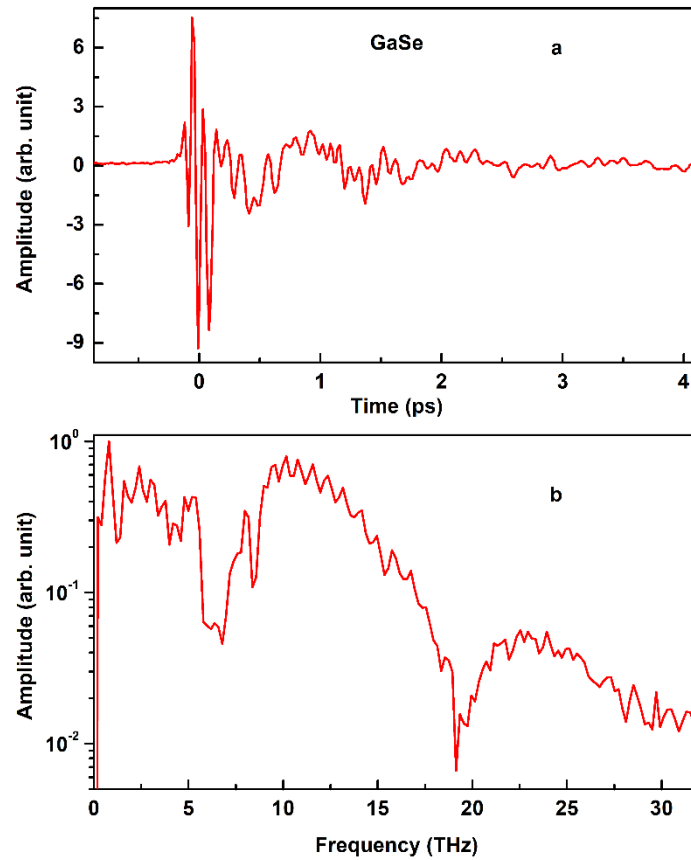


**Figure 2-4.** THz EO-detection with 30 μm GaSe crystal of Z-cut direction. The pulse temporal profile is shown in panel (a), the FFT spectrum is shown in the panel (b). The surface of the crystal is normal to the experimental table surface and tilted ~45 degrees with respect to the incoming probe and THz beams.

### 2.3.3. THz Detection with LAPC

**Figure 2-5** shows THz detection result with LAPC. The spectrum presented in panel (b) indicates that LAPC is capable of measuring THz up to approximate 17 THz without gap. In chapter 5 we will use LAPC to carry out broadband THz-TDS on imidazolium-based ionic liquids. Similar to GaSe, the surface of LAPC is tilted to obtain higher sensitivity. In addition, the sensitivity also depends on polarization combinations of THz and probe. The result shown in **Figure 2-5** is a typical result with horizontally polarized THz and probe, surface of LAPC normal to experimental table surface and tilted around 45 degrees with respect to THz and probe beams.
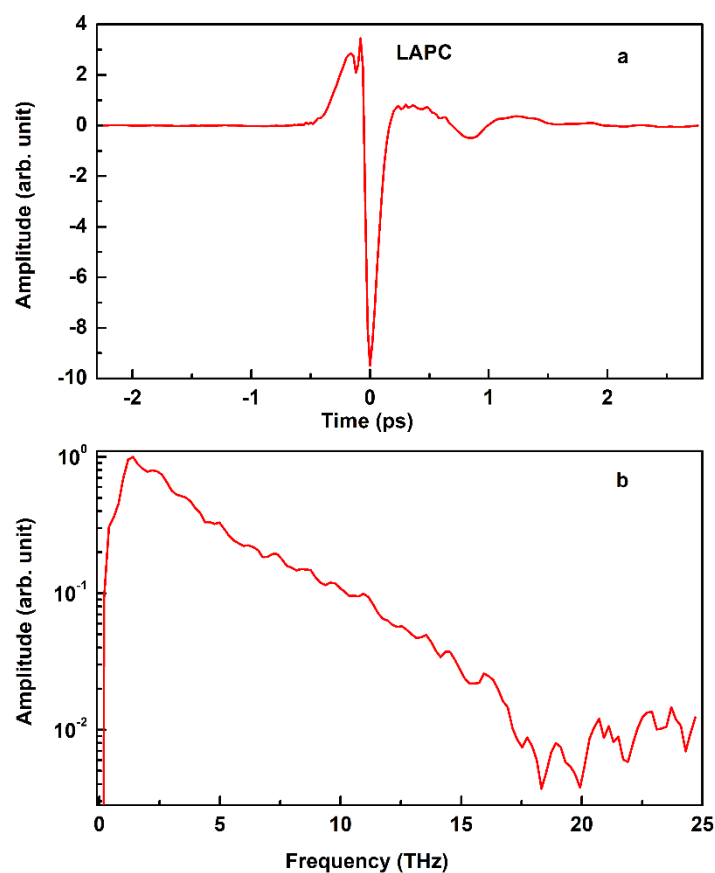
**Figure 2-5.** THz EO-detection with LAPC. The pulse temporal profile is shown in panel (a), the FFT spectrum is shown in the panel (b).

## 2.3.4. THz Detection with Air Sensor

We also measured the THz pulse with air sensor (without applied electric field). The temporal profile is displayed in **Figure 2-6.** The profile corresponds to the intensity of the THz electric field (often called "unipolar detection mode") rather than the field amplitude and phase, because the EFISH effect alone cannot discriminate the sign of the THz electric field. The field-and phase-resolved detection can be realized by applying a strong external electric field, introducing thus a local oscillator which can interfere with the SHG induced by THz[68]. Nonetheless, the time duration of the unipolar pulse allows us to estimate a 30 THz bandwidth, which is expected also by the laser pulse duration and the comparison with existing literature. In chapter 3 we

will demonstrate that this incoherent detection shows advantages in the application to measure micro-distance with THz pulse.
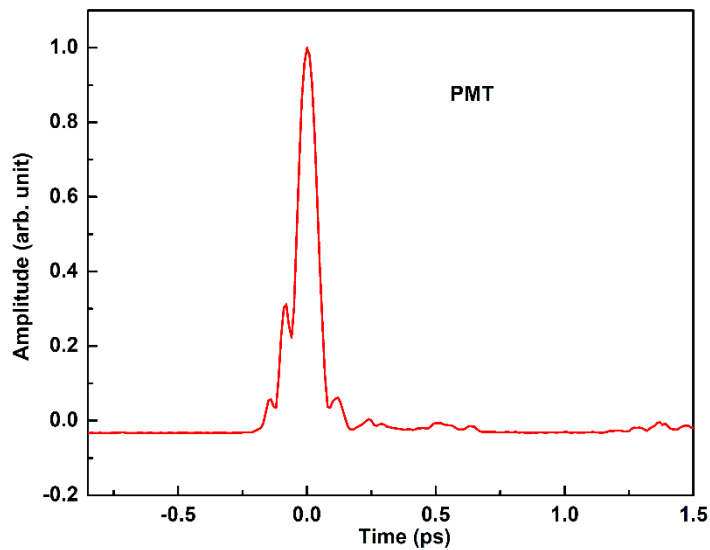


**Figure 2-6.** THz detection with air sensor. Temporal profile of incoherent THz detection with PMT using EFISH effect.

## 2.4. **CONCLUSION**

In summary, we built a high-energy broadband THz pulse generation setup, capable of delivering THz pulses having 1 MV/cm peak field amplitude and a ~30 THz bandwidth. We detected the THz field with both ZnTe, GaSe, LAPC and air sensor. The bandwidth detected by 500 μm ZnTe is narrower than that obtained with 250 μm ZnTe due to phase mismatch between THz and probe in thicker crystals. GaSe can measure THz spectrum up to ~30 THz but the spectrum has a deep gap around 6.5 THz due to phonon modes in the crystal. LAPC is capable of detecting THz up to around 17 THz without any gap. The air sensor measurement shows that the spectral bandwidth is about 30 THz.

# Chapter 3.    Micro-distance Measurement with Ultrashort THz Pulse

## 3.1.  INTRODUCTION

To measure the space length of liquid cell made of silicon wafers using mechanical tools such as vernier caliper and micrometer screw gauge we need to contact the tool with the cell. The pressure on silicon wafers when the tool touches wafers can shrink the space between wafers. Furthermore, the resolution of mechanical tools is limited. Vernier caliper has resolution of either 50 $\mu m$ (1/20 mm) or 20 $\mu m$ (1/50 mm), which is not accurate enough to measure distance in the range from tens of micrometers to several hundred micrometers. Micrometer screw gauge can reach resolution of 1 micrometer but the last digit of reading depends on users' care. Consequently, precise contactless methods are desired to measure the distance between silicon wafers.

Optics-based distance measurement techniques are contactless and can be used to measure absolute distance, displacement and other related parameters such as velocity and vibration of periodically moving objects[80]. Optics-based distance measurement are generally classified into three categories: interferometry, triangulation and time-of-flight methods[81]. Interferometry method measures distance by analyzing the fringe pattern created by two interfering beams. Usual interferometry is only capable of measuring displacement. Absolute distance measurement with interferometry requires other techniques such as frequency scanning interferometry[82]. Triangulation method determines distance based on triangular geometry. Conventional time-of-flight method[83] measures distance by means of measuring the round-trip transit time which short pulse light spends to accomplish the round-way travel. Other time-of-flight techniques include phase shift method using amplitude modulated continuous light[84] and frequency modulated continuous wave time-of-flight[85].

Optics-based distance measurement is contactless and can be very accurate. Michelson interferometers can reach subwavelength resolution. However, visible light is not applicable to measure the distance between silicon wafers. Compared with

other THz materials such as Teflon and quartz silicon wafers are perfect to construct liquid cell for broadband THz-TDS spectroscopy. Teflon is transparent for THz but susceptible to deformation. Quartz is transparent for visible light and narrowband THz but attenuates a lot the high-frequency part of broadband THz.

In summary, silicon wafers are perfect to make liquid cells but precise and contactless technique to measure the distance between two wafers is unavailable. In this chapter we introduce a precise and contactless distance measurement technique which is capable of measuring the distance between objects which is opaque to visible light but transparent to THz wave.

## 3.2. **EXPERIMENT**
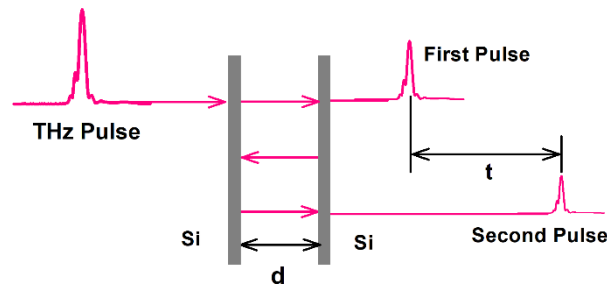


**Figure 3-1.** Process that THz pulse passes through silicon wafers. Part of THz pulse transmits through wafers directly (first pulse). Part of THz pulse reflected by wafers and travels one round trip between wafers (second pulse). Time delay between first and second pulse is t. The distance between the two silicon wafers is enlarged in the figure to show the reflection process more clearly.

**Figure 3-1** shows the process that THz pulse transmits trough silicon wafers. When THz reaches silicon wafers part of THz pulse passes silicon wafers directly (first pulse). Part of THz pulse is reflected and travels a round trip in the space between wafers before it leaves wafers (second pulse). Time delay between first and second pulses (t) can be measured with the same techniques to detect THz. This process of transmission and reflection can happen many times and consequently the transmitted THz pulse can travel any number of round trips between the wafers. The intensity of THz decreases with increasing round trips. To measure the distance between wafers (d) we select first and second pulses which are the most intensive ones. Besides the reflections between the two wafers there are also multiple reflections inside silicon

wafers. However, the reflections inside silicon wafers can be easily distinguished since the thickness of the wafers is much bigger than the distance between them and the refractive index of silicon in the THz range is around 3 times of that of air. The relation between d and t can be written as follow based on elementary physics.

$$d = c \times t/2\,, \qquad\qquad (3\text{-}1)$$

where c is the speed of light. Eq. (3-1) can be rewritten as follow to calculate expected time delay when distance is known.

$$t = 2 \times d/c \qquad\qquad (3\text{-}2)$$

## 3.3. RESULTS AND DISCUSSION

### 3.3.1. Confirmation of Method
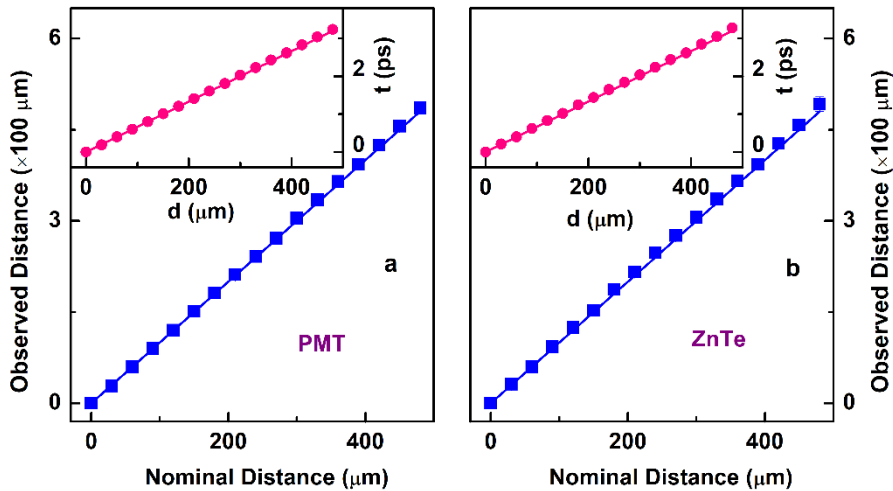


**Figure 3-2.** Observed distance as function with nominal distance measured with PMT (a) and ZnTe (b).The insets are observed time delay as function of nominal distance. The symbols are experimental results and the lines are theoretical results. The red lines are calculated with Eq. (3-2). The error bars are within the size of symbols.

In order to confirm the validity of the method to measure the distance between silicon wafers. We put one silicon wafer at the focus of parabolic mirror 2 in the setup show schematically in **Figure 2-1** and fixed its position. Then we mounted another silicon wafer on a stage. The distance between the two wafers is changed manually by moving the stage. The distance change is recorded by reading the micrometer screw

gauge of the stage, which is called as nominal distance. We increased the distance between wafers by a step of 30 $\mu m$ every time starting from a reference distance. For the simplicity we set the reference distance as zero. After each increase of distance of wafers we measured the time delay between first and second pulse and calculated the distance (observed distance) with Eq.(3-1). Totally we measured 17 distances including the starting point.

In the experiment THz time-domain waveforms are recorded with step equal to 0.01 ps. In order to measure the distance precisely the temporal pulse shape is taken into consideration. Time delay between first and second pulses are the time interval between the maxima points in first and second pulses. The resolution of distance measurement calculated with Eq.(3-1) is 1.5 $\mu m$.

We measured distance first with PMT in air and we repeated the process with ZnTe having thickness of 250 $\mu m$. Panel (a) and (b) of **Figure 3-2**respectively show the measured results with PMT and ZnTe. In the figure, the full square symbols are experimental results and the solid lines are theoretical results calculated with Eq.(3-1) and Eq.(3-2). We used the difference between experimental and theoretical results as measurement error. The error is so small that error bar is within the size of the symbols. Main panels of **Figure 3-2** plot the observed distance as function of nominal distance. The insets in **Figure 3-2** plot the time delay as function of nominal distance. It can be seen that the experimental results overlap the theoretical results very well with error bar being within the size of symbols. **Figure 3-2** demonstrates that the distance between silicon wafers can be precisely measured by THz pulse either with PMT or ZnTe. In the following section we discuss the difference of these two methods.

### 3.3.2. Comparison of ZnTe and PMT

As shown in the above section, we can precisely measure distance with either ZnTe or PMT. However, it is worth noting that the THz pulse detected by ZnTe is much wider than that detected by PMT. In addition, the THz pulse detected by ZnTe is bipolar and that detected by PMT is unipolar. These differences lead us to speculate that PMT is more applicable when measuring small distances since we can distinguish first and second pulse when time delay is small. In the case of ZnTe the peaks of second

pulse could be blurred by the first one when the positive peak of second pulse overlaps minus peak of the first one and vice versa
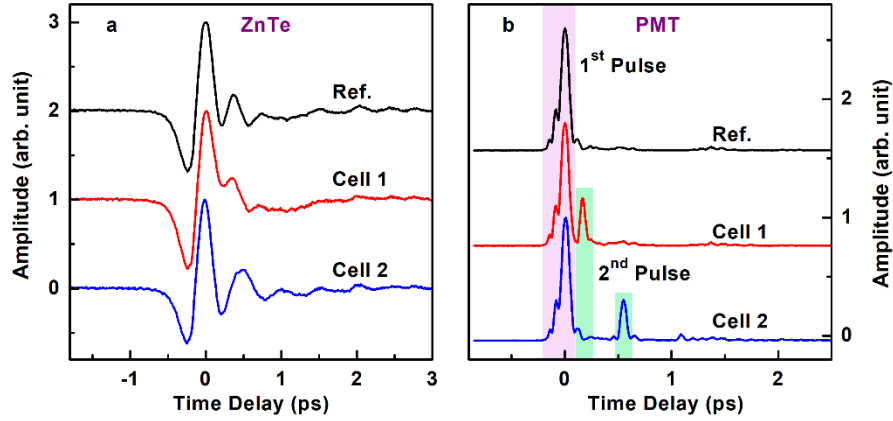


**Figure 3-3.** Comparison of the ability to measure micro-distance for ZnTe (a) and PMT (b). Reference is measured with two silicon wafers far enough that second pulse is out of the scan window. First and second pulses cannot be distinguished for cell 1 and cell 2 with ZnTe while they are separated very well with PMT.

In order to verify the ability of PMT and ZnTe to measure small distance we made two cells with two kind of spacers whose nominal thickness are 20 and 50 $\mu m$. **Figure 3-3** shows the measurement result with ZnTe and PMT. In the figure the black curve in both panel (a) and (b) are measured with two silicon wafers far from each other enough that second pulse is out the scan window. Panel (a) shows the measurement with ZnTe. From panel (a) we cannot distinguish second pulse from the first as the time delay is too short that the peaks of second pulse are blurred by those of first one. Panel (b) shows measurement of the same cells with PMT. In panel (b) the second pulse is well separated from the first one so we can measure the thicknesses of cell 1 and cell 2 even though they are too small for ZnTe. The comparison of the ability of the two methods to measure small distance shows that PMT is capable of measuring small distances while ZnTe cannot distinguish first and second pulses when the distance is small.

### 3.3.3. Comparison ZnTe in Air and Nitrogen

The measurements with ZnTe in the former two sections are conducted in nitrogen while those with PMT are always conducted in air. In this section we discuss how much the measurement environment affects experimental results. In order to investigate the effect of environment on distance measurement we measured distance of two silicon wafer with ZnTe both in air and in nitrogen. The measurement results are shown in **Figure 3-4**. In the figure the red curve are measure with two silicon wafers far enough that second pulse is out the scan window as reference. Panel (a) is the measurement results in nitrogen and panel (b) is measured in air.
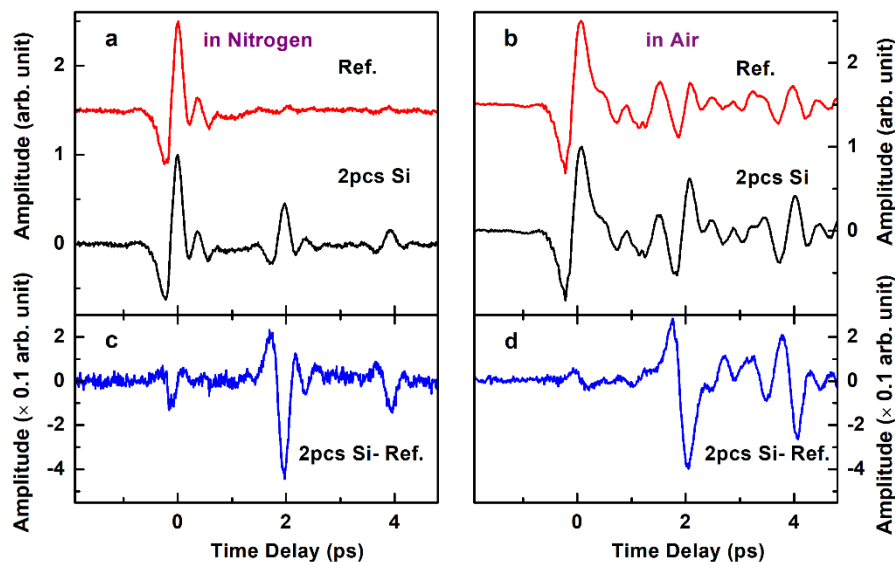


**Figure 3-4.** Distance measurement with ZnTe in nitrogen (a) and air.(b). Panel (a) clearly shows first, second and third pulses. Second and third pulse cannot be distinguished in panel (b). Subtraction of the reference curve from the curve of two pieces silicon measured in nitrogen (c) and air (d).

It is clear that there are no obvious oscillations in the reference curve in panel (a) after the pulse located at time delay equal to zero while in panel (b) there are continuous oscillations following the first pulse. From the black curve of two pieces of silicon in panel (a) we can see second pulse and even third pulse clearly. However, we cannot distinguish second pulse from the black curve in panel (b). Close observation of black curve in panel (b) shows some different details in the oscillations following the first pulse compared with the reference curve. To single out these small

differences in oscillations we subtracted red reference curve from black curve and drew the result in second row of **Figure 3-4**. Obviously, panel (c) duplicates second and third pulse in the blue curve. Panel (d) recovers second and third pulse even though they are hidden in oscillations in the black curve of panel (b). From the recovered pulse in panel (d) we can also calculate the distance between silicon wafers. Comparison of the measurement in nitrogen and air shows that measurement in nitrogen can show peaks immediately while further analysis is necessary to display second and third peaks for measurement in air.

### 3.3.4. Application Example
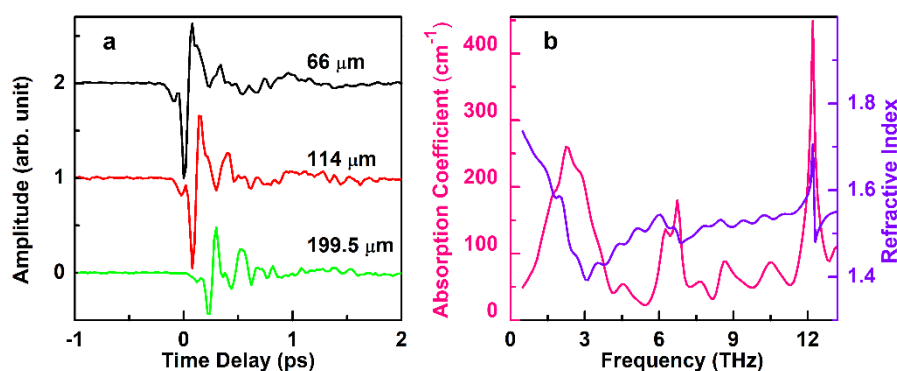


**Figure 3-5.** Application of micro-distance measurement method. Time-domain waveform of THz through samples having different thicknesses (a). Absorption coefficient and refractive index extracted based on the precise thickness measurement (b).

In this section, we use the PMT method described above to measure the absorption coefficients and refractive index of 1-butyl-3-methylimidazolium bis(trifluoromethylsulfonyl)imide ([C4C1im][Ntf2]), which is one type of ionic liquids. We first made liquids cells using silicon wafers and measured the thickness of the cells with PMT in air. Then we filled the cells with [C4C1im][Ntf2] and measured the THz pulse transmitted the sample. Panel (a) of **Figure 3-5** shows the time-domain THz waveform passing samples with different thicknesses. Absorption coefficient and refractive index are extracted with the method described in appendix. The method we developed in this chapter provides a powerful means to measure cell thickness. We can precisely measure absorption coefficient and refractive index of liquids based on the accurate thickness measurement.

## 3.4. **CONCLUSION**

In this chapter we described precise micro-distance measurement method based on THz. We found that the measurement resolution can reach 1.5 $\mu m$. Compared with vernier caliper whose resolution is 50 $\mu m$ or 20 $\mu m$ micro-distance measurement method described in this chapter is much more accurate. The resolution of micrometer screw gauge is 1 $\mu m$ but the last digit dependent on user's care can result in lager uncertainty in measurement. Method proposed herein has comparable resolution with micrometer screw gauge and the reading doesn't depend on user's care. More importantly, distance measurement using THz is contactless and it's the only choice where contact measurement is not applicable.

We also compared the ability of PMT and ZnTe to measure micro-distance. When measuring bigger distance there is nearly no difference between the measurement with ZnTe and PMT. However, ZnTe cannot measure small distance due to the wider resultant THz pulse while PMT is capable of measuring distance down to ~20 $\mu m$. In addition, we compared distance measurement in nitrogen and in air with ZnTe. It is revealed that reflected THz pulses can be directly shown with the measurement in nitrogen while they are hidden in residual oscillations in the measurements in air. Further data analysis is necessary to display the reflected pulses for the measurement conducted with ZnTe in air. Finally, we showed an application example to apply the method developed herein to measure absorption coefficient and refractive index of liquid. From the comparison between ZnTe and PMT, the advantages of PMT include shorter pulse, ability to measure micro-distance down to ~20 $\mu m$ and immunity to water vapor absorption in air.

# Chapter 4.    THz-TDS of Mixtures of Ionic Liquids

## 4.1.  INTRODUCTION

Although ionic liquids (ILs) can be any molten salt composed of only cations and anions, the term more often refers to molten salt at ambient temperature. They are also termed as room temperature ionic liquids[86]. Their outstanding unique characteristics such as enhanced thermal and chemical stability, high solvation ability, low volatility and low combustibility make ILs suitable for many invaluable applications in scientific and industrial fields. ILs are increasingly used as electrolytes for lithium battery[87], catalysts[88] and lubricant additive[89]. They have gained the reputation as 'designer solvents' since their structures and physicochemical properties may be tailored by selecting constituent ions from a wide range of available cations and anions[90]. In order to tune the physical and chemical properties of ILs, one option is to synthesize neat ILs consisting of different constituent ions. Another solution is to mix different neat ILs. Mixtures may have properties outside the boundaries defined by neat components or obey ideal or quasi-ideal mixing laws.[91] Either results have potential applications since a detailed knowledge of the mixing laws may help in tailoring specific physicochemical properties and functionalities.

Neat ILs and their mixtures have been investigated with different techniques including calorimetry[92], infrared spectroscopy[93-94], Raman spectroscopy[95], dielectric relaxation spectroscopy[96-99], optical Kerr effect spectroscopy[100-103], X-ray photoelectron spectroscopy[104], terahertz spectroscopy[105-109]. For what concerns the mixing behavior of ILs mixtures, the investigated properties include viscosity, density, molar volume, conductivity, thermal stability, enthalpy and so on. The reported data show that most of the aforementioned properties follow 'ideal' or 'quasi-ideal' mixing law. In 2015, Clough et al.[91] evaluated physicochemical properties including density, phase behavior, viscosity, conductivity and thermal stabilities in ILs mixtures and observed that these characteristics comply with ideal mixing laws with some consistent deviation. In 2016, Almeida et al.[110] investigated the density and viscosity of several ILs mixture systems containing the same cations and reported that there were nearly null deviations from ideal mixing rule of the molar volume. Moreover,

Villar-Gracia et al. [104] presented their investigation of electron density distribution in ILs mixtures and found that the binding energies of carbon and nitrogen atoms in the cation head varied in a quasi-linear way as a function of the concentration ratio. Following this observation, the authors proposed a way to tune electronic environment of the constituent ions by mixing ILs.

ILs have been investigated by THz spectroscopy in order to study their intermolecular interactions which show vibrational signatures in the THz interval of frequencies. In 2007, Yamamoto et al.[109] investigated the interaction between cation and anion in 1-ethyl-3-methylimidazolium trifluoromethanesulfonate and 1-ethyl-3-methylimidazolium tetrafluoroborate with THz-TDS. The authors concluded that the dielectric spectra of the two ILs are dominantly determined by intermolecular vibrations. In 2011, Chakraborty et al.[105] reported dielectric spectra in THz band of novel metallocenium ionic liquids. In their work, they revealed the intermolecular dynamics by simulating the imaginary part of dielectric spectra with different combinations of model functions. In 2015, Yamada et al.[107] investigated the vibrational modes of ILs bearing imidazolium cations with different alkyl-chain lengths and several molecular anions using THz-TDS. Koeberg et al.[111] investigated the behavior of mixture containing 1-butyl-3-methylimidazolium tetrafluoroborate and water with THz-TDS. Asaki et. al.[112] studied the mixture of acetonitrile and 1-ethyl-3-methylimidazolium triflate with THz spectroscopy. Fumino et al.[113] investigated mixture of ammonium-base protic ILs with low-frequency infrared spectroscopy and found characteristic deviation from ideal mixing law. Stoppa et al.[114] studied imidazolium-base ILs mixture in the frequency range $0.2 \leqslant v/\text{GHz} \leqslant 20$ and found a gradual structural change, enhanced rotational and translational dynamics in the mixtures. However, to the best of our knowledge, a detailed study on the THz complex permittivity of imidazolium-base aprotic ILs mixtures and its corresponding mixing law has not been reported yet. In general, the real part of the complex permittivity indicates the ability of the material to store energy while the imaginary part indicates the capability to convert the absorbed electromagnetic energy into heat[115]. On the other hand, complex permittivity is intimately related to the dynamics of intermolecular and intramolecular motions. Therefore the knowledge of complex

relative permittivity is essential to predict the solubility of a substance, which is valuable in many technological and scientific applications. As an example, in pharmaceutical science, drug's attributes such as solubility, chemical stability and acid dissociation can be better interpreted with the aid of permittivity constant[116]. In this chapter, we discuss the mixing law of the THz permittivity spectra of binary ILs mixtures.

## 4.2. EXPERIMENTAL SECTION
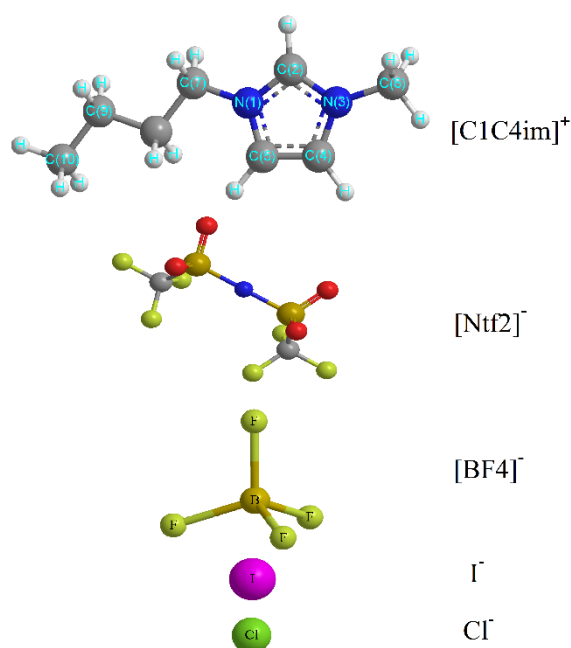


**Scheme 4-1.** Structure of the common cation of [C4C1im][Ntf2], [C4C1im][BF4], [C4C1im]I and [C4C1im]Cl and their anions. Serial numbers of the carbon and nitrogen atoms in the imidazolium ring and side chains are shown in the structure model of cation.

Before mixing, commercial ILs with a purity of 99% were further purified in a vacuum chamber at room temperature for 12 hours to remove volatile impurities and water. In this chapter we focus on binary mixtures made of 1-butyl-3-methylimidazoulium iodide ([C4C1im]I) and 1-butyl-3-methylimidazoulium bis (trifluoromethylsulfonyl) imide ([C4C1im][NTf2]). The structures of these two ILs together with 1-butyl-3-methylimidazolium tetrafluoroborate ([C4C1im][BF4]) and 1-butyl-3-methylimidazolium chloride ([C4C1im]Cl) are shown in **Scheme 4-1**. [C4C1im][BF4] and [C4C1im]Cl including the two ILs investigated in this chapter are

the samples of broadband THz spectroscopy in chapter 5. Various mixtures of these neat ILs were prepared. Samples of mixtures were filled in handcrafted cells of different thicknesses and silicon windows which are almost transparent in the THz range. Complex permittivity spectra in the frequency range 0.15–4.5 THz were measured by means of a fs-laser-based THz-TDS spectrometer as described in chapter 2. The THz optical field transmitted through the sample is measured in amplitude and phase by means of time-domain electro-optic sampling. The complex permittivity spectra, whose real part is known as relative permittivity and imaginary part is named dielectric loss, are obtained by Fourier transforming the transmitted THz pulses in the time domain, and normalizing them with respect to a reference spectrum. More details data extraction can be found in appendix and detailed description of experimental set-up is presented in chapter 2.

## 4.3. **RESULTS AND DISCUSSION**

### **4.3.1.** Complex Permittivity: The Ideal Mixing Law

The definition of the ideal permittivity behavior of a mixture is a long-standing yet unsolved question. In order to investigate the permittivity of liquid mixtures, several models have been discussed[115, 117-120]. R.J. Sengwa et. al.[115] used a molar scale to describe the permittivity behavior of mixtures of formamide and N,N-dimethylformamide in microwave frequency region while Buep[121] showed that the ideal complex permittivity in a liquid mixture can be defined as the volumetric weighted average of the complex permittivities of the individual components by adopting a thermodynamic point of view. Moreover, Iglesias et al.[122] stressed that the permittivity can be expressed as a sum of individual component permittivities, weighted with the volume fraction other than mole fraction. Joao Carlos R. Reis et. al.[123] demonstrated that ideal relative permittivity of liquid mixtures is a volume-fraction-weighted average of the pure-component relative permittivities, finding confirmation in experiments. In addition, some effective permittivity theories are also available[124-125]. In this chapter, the definition proposed by Buep is adopted to analyze the binary mixtures of [C4C1im]I and [C4C1im][NTf2]. The complex permittivity of a material can be written as

$$\tilde{\varepsilon} = \varepsilon' - i\varepsilon", \qquad (4\text{-}1)$$

where $\varepsilon'$ is the relative permittivity function and $\varepsilon"$ is usually called the dielectric loss function.

Let's consider a binary mixture made by substance A and substance B. According to Buep's theory, the complex permittivity of an ideal binary mixture obeys the following linear equation:

$$\tilde{\varepsilon}_M^{id} = \tilde{\varepsilon}_A \phi_A + \tilde{\varepsilon}_B \phi_B, \qquad (4\text{-}2)$$

where $\phi_A$ and $\phi_B$ denote the volume fractions of substance A and B, respectively, while $\tilde{\varepsilon}_M^{id}$, $\tilde{\varepsilon}_A$ and $\tilde{\varepsilon}_B$ represent the ideal complex permittivity of the mixture, and the complex permittivity of substance A and substance B, respectively. The ideal relative permittivity and ideal dielectric loss are obtained by writing the real and imaginary parts of Eq. (4-2) separately:

$$\varepsilon'^{id}_M = \varepsilon'_A \phi_A + \varepsilon'_B \phi_B, \qquad (4\text{-}3)$$

$$\varepsilon"^{id}_M = \varepsilon"_A \phi_A + \varepsilon"_B \phi_B, \qquad (4\text{-}4)$$

where $\varepsilon'^{id}_M$ and $\varepsilon"^{id}_M$ are the ideal relative permittivity and the ideal dielectric loss of the mixture. $\varepsilon'_A, \varepsilon'_B$, $\varepsilon_A"$ and $\varepsilon_B"$ are the relative permittivity of A and B, and the dielectric loss of A and B, respectively. The so-called "excess" relative permittivity and "excess" dielectric loss is defined as the deviation from the ideal behavior and therefore can be written as:

$$\varepsilon'_E = \varepsilon'^{exp}_M - \varepsilon'^{id}_M = \varepsilon'^{exp}_M - (\varepsilon'_A \phi_A + \varepsilon'_B \phi_B), \qquad (4\text{-}5)$$

$$\varepsilon''_E = \varepsilon"^{exp}_M - \varepsilon"^{id}_M = \varepsilon"^{exp}_M - (\varepsilon"_A \phi_A + \varepsilon"_B \phi_B), \qquad (4\text{-}6)$$

where $\varepsilon'^{exp}_M$ and $\varepsilon"^{exp}_M$ are the measured relative permittivity and dielectric loss of binary mixtures.

When comparing ideal and measured spectra, it is often useful to introduce a global parameter that measures the average deviation of the measured spectrum from the ideal one. Xiao et al.[101] defined the non-additivity parameter, which is the difference between theoretical and experimental results, to estimate the ideality of

mixtures. Following this idea, we introduce a relative non-additivity parameter, which is defined as the ratio of the root-mean-squared deviation of the experimental results from calculated results and the sum of experimental result, i.e.:

$$\Delta\varepsilon = \frac{\sqrt{\sum_i[\varepsilon_M^{exp}(\nu_i)-\varepsilon_M^{id}(\nu_i)]^2}}{\sum_i \varepsilon_M^{exp}(\nu_i)} = \frac{\sqrt{\sum_i[\varepsilon_E(\nu_i)]^2}}{\sum_i \varepsilon_M^{exp}(\nu_i)}, \qquad (4\text{-}7)$$

where $\varepsilon$ may, alternatively, indicate either $\varepsilon'$ or $\varepsilon''$.

### 4.3.2. Relative Permittivity and Dielectric Loss Spectra
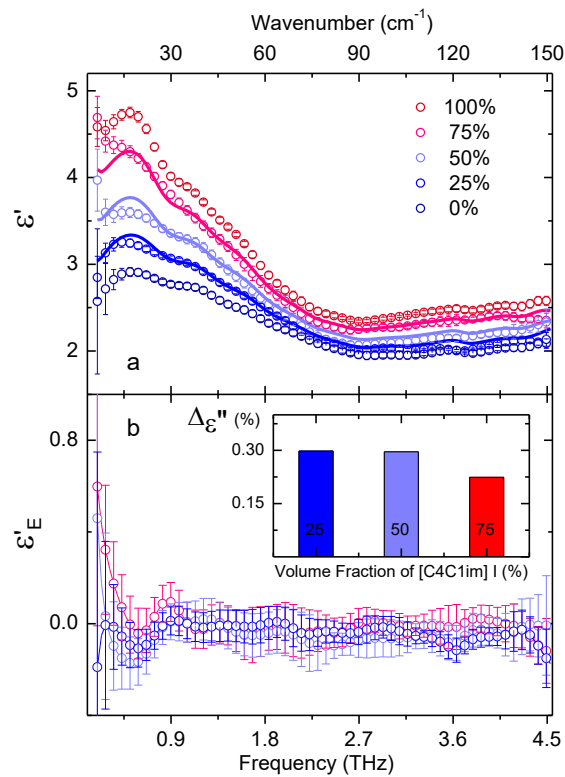


**Figure 4-1.** (a) Relative permittivity spectra of binary mixtures of [C4C1im]I and [C4C1im][NTf2]. Circles represent measured spectra, solid lines indicate ideal spectra as calculated with Eq.(4-3). Different colors stand for various volume fractions of [C4C1im]I as reported in the legend. (b) Excess relative permittivity spectra. Inset: Relative non-additivity parameter versus volume fractions of [C4C1im]I.

In **Figure 4-1** (a) the relative permittivity spectra of different mixtures of [C4C1im]I and [C4C1im][NTf2] are plotted. In the figure, the dark red and dark blue open circles represent the measured spectra of neat [C4C1im]I and [C4C1im][NTf2], respectively. The shading colors (light red, violet and light blue) open circles represent

the measured spectra obtained with volume fractions of [C4C1im]I equal to 0.756, 0.467, 0.232, all measured with ±0.002 accuracy. In the following, we will refer for simplicity to round numbers: 75%, 50% and 25% respectively. Solid lines represent the ideal spectra as calculated with Eq. (4-3) starting from the relative permittivities of neat [C4C1im]I and [C4C1im][NTf2], and using the only the measured pure sample spectra and the measured volume fractions.

The most prominent characteristic of **Figure 4-1** (a) is that the measured spectra overlap quite well with the ideal spectra without any additional adjustable parameters. This result demonstrates that the relative permittivity spectra of our ILs mixtures follow to a very good extent an ideal mixing law. It can be seen, at the lowest frequencies, the deviations from the ideal behavior increase. These bigger deviations may originate from different dynamic processes in different frequency regions. In addition, these deviations are better visible in the curve of excess relative permittivity shown in **Figure 4-1** (b): they could be the signature of non-ideal processes taking place in this range but, due to the high uncertainty of our spectra in this frequency range, further investigations by means of gigahertz standard dielectric spectroscopy[96] are required to clarify this issue.

In the inset of **Figure 4-1** (b), the relative non-additivity parameter calculated according to Eq. (4-7) for each relative permittivity spectrum is plotted as a function of the volume fraction of [C4C1im]I. We note that our spectra are reproduced by a linear mixing law with no adjustable parameters within less than 0.3% average deviation for every mixture.

**Figure 4-2** (a) shows the dielectric loss spectra. The colors, symbols and the lines have the same meaning as for the relative permittivity graphs. In **Figure 4-2** (a), we note again that the measured spectra are quite well reproduced by the ideal spectra. **Figure 4-2** (b) and the inset show the corresponding excess dielectric loss spectra and non-additivity parameter, respectively. Also in this case, both excess dielectric loss spectra and non-additivity parameter prove that the ideal mixing law is valid within a 1.5% deviation.
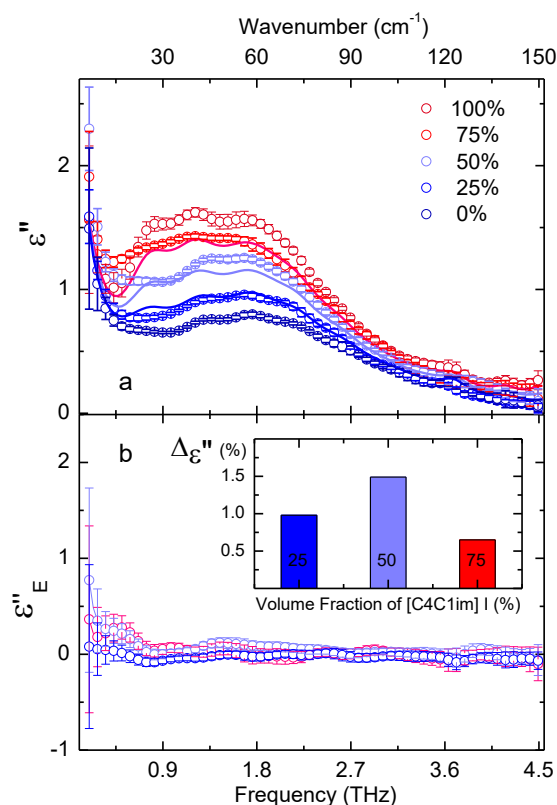
**Figure 4-2.** (a) Dielectric loss spectra of binary mixtures of [C4C1im]I and [C4C1im][NTf2]. Circles represent measured spectra, solid lines indicate ideal spectra as calculated with Eq.(4-4). Different colors stand for various volume fractions of [C4C1im]I as reported in the legend. (b) Excess relative permittivity spectra. Inset: Relative non-additivity parameter versus volume fractions of [C4C1im]I.

The observed ideal behavior of complex permittivity could be originated from the microstructure of ILs. Xiao et. al.[126] suggested that in ILs the anions and cations' imidazolium heads form polar regions while the alkyl chains of cations point toward each other forming nonpolar regions. Xiao et. al.[101] further investigated two binary mixtures, one comprising 3-methyl-1-pentylimidazolium bromide ([C5mim]Br) and 3-methyl-1-pentylimidazolium bis(trifluoromethanesulfonyl)imide ([C5mim][NTf2]) while another one comprising 3-methyl-1-pentylimidazolium hexafluorophosphate ([C5mim][PF6]) and 3-methyl-1-pentylimidazolium trifluoroacetate ([C5mim][TFA]). Their results showed that optical Kerr effect spectra for mixture of [C5mim]Br and [C5mim][NTf2] are nearly additive while nonadditive for mixture of [C5mim][PF6] and [C5mim][TFA]. They speculated in the mixture of [C5mim]Br and [C5mim][NTf2] the ionic networks are arranged as those in neat ILs for the reason that the size of anions

are different, while the ionic networks in mixtures of [C5mim][PF6] and [C5mim][TFA] are more random since the size of anions are comparable. Similarly, the ideal behavior of complex permittivity in our case is reasonable when conjecturing the ionic networks in mixtures of [C4C1im]I and [C4C1im][NTf2]are ordered as those in neat [C4C1im]I and [C4C1im][NTf2]. The idea of polar and nonpolar regions can also shed light on interpretation of mixing behavior in the case of mixture of ILs with water[111], and with acetonitrile[112]. The evidence of influence of the solvents on ionic networks are straightforward in research of contact ion pairs and solvent-separated ion pairs in mixtures of ILs and molecular solvents[127]. With the increasing dilution of ILs, contact ILs ion pairs can be separated. Thus the ionic networks will be modified.

### 4.3.3. Analysis of the Complex Permittivity

Dielectric loss spectra are commonly simulated by a combination of several oscillators. Chakraborty et al.[105] simulated the imaginary part of permittivity with four Lorentzian functions in their THz spectra of metallocenium ILs. Turton et al.[128] fitted the dielectric loss spectra with a combination of different kinds of functions from ~ 400 MHz to above 10 THz. In this section, we analyze our results by modeling the complex permittivity spectra with a suitable combination of damped harmonic oscillators. To fit the spectrum of a neat IL we use the following equation:

$$\tilde{\varepsilon} = \varepsilon_\infty + \sum_{j=1}^n \frac{S_j v_j^2}{v_j^2 - v^2 + i\gamma_j v} \ , \qquad\qquad (4\text{-}8)$$

where $\varepsilon_\infty$is the value of permittivity at infinite frequency, $S_j$ is the amplitude of the oscillator, $v_j$ is the resonance frequency, $\gamma_j$ is the damping constant and $v$ is the wave frequency. $\varepsilon_\infty$, $S_j$, and $v_j$ are the fitting adjustable parameters.

As shown in the above section, the complex permittivity of binary mixture of [C4C1im]I and [C4C1im][NTf2] follows with good approximation a linear mixing law as expressed by Eq. (4-2). Therefore, in first approximation, we can model the complex permittivity of a binary mixture with the following equation:

$$\tilde{\varepsilon}_M = \phi_A \varepsilon_A + \phi_B \varepsilon_B = \phi_A \left( \varepsilon_{A,\infty} + \sum_{j=1}^{n} \frac{S_{A,j} v_{A,j}^2}{v_{A,j}^2 - v^2 + i\gamma_{A,j}v} \right) + \phi_B \left( \varepsilon_{B,\infty} + \right.$$

$$\left. \sum_{j=1}^{n} \frac{S_{B,j} v_{B,j}^2}{v_{B,j}^2 - v^2 + i\gamma_{B,j}v} \right), \tag{4-9}$$

where $\phi_A$ and $\phi_B$ are fixed parameters as given by the measured volume fractions.

**Table 4-1.** Fit parameters of Eq. (4-9)[a].

| ionic liquids | [C4C1im]I | [C4C1im][NTf2] |
|:---:|:---:|:---:|
| $S_1$ | $3.0 \pm 0.6$ | $4.5 \pm 0.8$ |
| $v_1$ | $0.17 \pm 0.02$ | $0.11 \pm 0.03$ |
| $\gamma_1$ | $0.30 \pm 0.13$ | $0.14 \pm 0.04$ |
| $S_2$ | $0.9 \pm 0.4$ | $1.1 \pm 0.5$ |
| $v_2$ | $0.89 \pm 0.13$ | $0.7 \pm 0.4$ |
| $\gamma_2$ | $1.0 \pm 0.5$ | $2.1 \pm 0.6$ |
| $S_3$ | $1.5 \pm 0.3$ | $0.7 \pm 0.2$ |
| $v_3$ | $1.98 \pm 0.06$ | $2.13 \pm 0.11$ |
| $\gamma_3$ | $2.21 \pm 0.15$ | $2.3 \pm 0.3$ |
| $\varepsilon_\infty$ | $2.87 \pm 0.02$ | $2.20 \pm 0.02$ |

[a] The parameters are obtained by fitting together both the real and imaginary parts of the complex relative permittivity spectra of all neat components and their mixtures together. The errors are statistical errors given at a confidence level of 66% (one sigma). $v$ and $\gamma$ are in THz units.

In this work, we used a 'global fit' procedure that consists in fitting with a single choice of the parameters of the oscillators both the real and imaginary parts of the complex permittivities of all the mixtures, including neat ILs spectra. This makes the fit procedure more robust against experimental fluctuations. The fit is carried out by using a nonlinear least-square algorithm based on a $\chi^2$ criterion. By performing a $\chi^2$ test it turned out that three oscillators were sufficient to get a good fit of the spectrum of each neat IL without overestimating the number of fit parameters. The parameters obtained with the global fit procedure are listed in **Table 4-1**, while the fitted curves are shown in **Figure 4-3**.
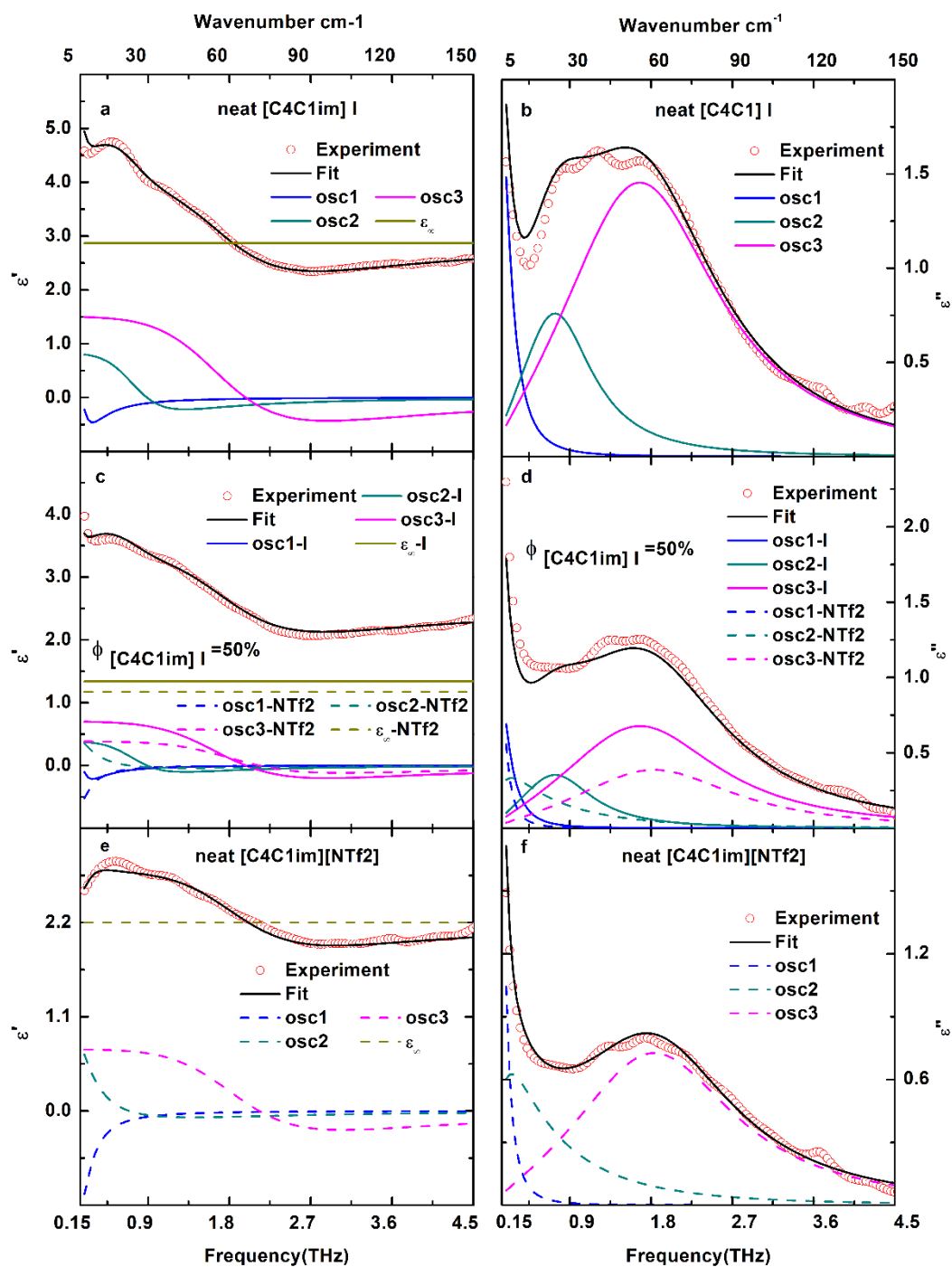
**Figure 4-3.** Relative permittivity spectra of neat [C4C1im]I (a), of a representative mixture with a volume fraction of [C4C1im]I equal to 50% (c), and [C4C1im][NTf2] (e). Dielectric loss spectra of neat [C4C1im]I (b), of a representative mixture with a volume fraction of [C4C1im]I equal to 50% (d), and [C4C1im][NTf2] (f). Red circles represent experimental data. Black solid line is the fitting curve resulting from Eq. (4-9). The curves representing each of the three oscillators are also reported with colored lines for neat [C4C1im]I (solid lines) and [C4C1im][NTf2] (dashed lines). The dark yellow solid and dashed straight lines indicate the value of $\varepsilon_\infty$ for neat [C4C1im]I and [C4C1im][NTf2], respectively. Note that the central frequencies do not coincide with the maximum of the resonances since the oscillators are asymmetric.

In **Figure 4-3** we plot the fitting curves for neat [C4C1im]I and [C4C1im][NTf2], and for one representative mixture with volume fraction of [C4C1im]I equal to 50%. The results for the other mixtures are reported in appendix.

The panels at the left of **Figure 4-3** report the real part of complex permittivity, while the corresponding imaginary parts are displayed in the panels at the right. Panels (a, c, e) of **Figure 4-3** display the relative permittivity spectra of neat [C4C1im]I, of a representative mixture with a volume fraction of [C4C1im]I equal to 50%, and neat [C4C1im][NTf2], respectively. The corresponding dielectric loss spectra are reported in the panels (b, d, f) of the same figure. In all panels the red open circles represent the experimental data. The black solid lines indicate the fits based on the model expressed by Eq.(4-9). The dark yellow solid and dashed lines represent the values of the infinite frequency permittivity for neat [C4C1im]I and [C4C1im][NTf2], respectively. The blue, dark cyan and magenta solid lines indicate respectively oscillator 1, 2 and 3, as listed in **Table 4-1**, giving the spectrum of neat [C4C1im]I while the blue, dark cyan and magenta dashed lines represent respectively oscillator 1, 2 and 3 contributing to the spectrum of neat [C4C1im][NTf2].

It is evident that for each neat component three oscillators are sufficient to reproduce the experimental data with reasonable accuracy. We would like to remark here that it is possible with our model to obtain better results when applied on the single curve, avoiding for instance the slight discrepancies observed in **Figure 4-3** (b, d), but the "global fit" procedure that we used here assure a very sound test bed for the model, far beyond what can be achieved by a single-curve fitting procedure, because all curves of the data-set are fitted together with a single choice of the parameters. For [C4C1im]I the three bands locate at approximately 0.17, 0.89 and 1.98 THz and 0.11, 0.70 and 2.13 THz for [C4C1im][NTf2]. We can tentatively assign the lowest band of both neat [C4C1im]I and [C4C1im][NTf2] to either rotational diffusion motion or to diffusive translational motion. This assumption is consistent with literature: Giraud et al.[129] modeled their optical heterodyne-detected Raman-induced Kerr effect spectra (OHD-RIKES) between ~30 GHz and ~6 THz by a sum of six Brownian oscillators. They assigned the lowest frequency band of different samples between ~0.05 and ~0.18 THz to rotational diffusion motion or to diffusive translational motion.

Furthermore Sonnleitner et al.[130] suggested that the mode in the 0.05-1 THz region is mainly related to translational motion.

Regarding the other two oscillators, they may correspond either to intermolecular motions or to librational motions. Giraud et al.[129] assumed their OHD-RIKES bands at approximately 0.9, 2, and 3 THz (~30, 65, and 100 cm$^{-1}$) are due to three different librational motions corresponding to three types of preferable locations of anions. Xiao et al.[131] similarly assigned their OHD-RIKES bands at approximately 0.9, 1.8, 3 and 5 THz (~30, 60, 100, and 170 cm$^{-1}$). Moreover, Stoppa et al.[132] assigned their bands at approximately 0.7 and 2.5 THz to cationic librational motions. In addition, Chakraborty et al.[105] fitted the imaginary part of dielectric permittivity obtained by THz spectroscopy and assigned the intermediate two bands to intermolecular motions which involve both cations and anions. Moreover they suggested the last band is due to librational motion. The assignment of intermolecular motions is also suggested by Yamamoto[109] and Yamada[108].

Of course these assignments must be taken with the necessary care, because when comparing different results the fitting functions and the number of fitting oscillators in the approximately same frequency region are different. However, it is widely agreed that the lowest band corresponds to rotational diffusion motion or to diffusive translational motion and the higher frequency bands is corresponding to intermolecular motions or to librational motions.

## 4.4. **CONCLUSION**

We have measured the complex permittivity spectra of five mixtures of [C4C1im]I and [C4C1im][NTf2], with volume fraction of [C4C1im]I equal to 25%, 50% and 75%, respectively. The spectra of the mixtures were compared with those calculated from the spectra of the neat components through Eq. (4-2), which describes a linear mixing law. The measured spectra are well described by this law within few percent accuracy.

Starting from this observation we have fitted our spectra with a linear combination of damped harmonic oscillators through a global fit procedure. This procedure allows an accurate characterization of the resonances present between

0.15 and 4.5 THz in our neat ILs. Then the lowest band of both the neat component ILs were tentatively assigned to rotational or translational motion, and the other two bands to intermolecular or librational motions in ILs.

In summary, the observation that the complex permittivity follows a linear mixing law is an important step to achieve a continuous tuning of the physicochemical properties of specific mixtures of these ILs, while the global fit method here presented may be useful for a robust estimate of the vibrational modes of other neat ILs.

# Chapter 5.    Broadband THz-TDS of Imidazolium-based ILs

## 5.1.  INTRODUCTION

Hydrogen bonds can be formed between cations and anions. Intermolecular interactions such as hydrogen bonds can affect the vibrations of C-H covalent bonds in cations. The intermolecular vibrations can be detected with far-infrared spectroscopy or THz-TDS while the vibrations of C-H covalent bonds can be detected with infrared (IR) spectroscopy. The existing literatures[94, 107, 133] on IR spectroscopy of imidazolium-based ILs have shown that the absorption peaks in the region from 2800 to 3000 cm$^{-1}$ (corresponding to 84-90 THz) are ascribed to asymmetric and symmetric C-H vibrations in the alkyl groups attached the imidazolium ring while the peaks in the 3000 - 3200 cm$^{-1}$ (corresponding to 90-96 THz) range are ascribed to C-H vibrations of imidazolium ring. Moreover, the crystal structures of this compound in the solid phase have attracted attention too. Monoclinic and orthorhombic crystal polymorphs of [C4C1im]Cl have been investigated by X-ray powder patterns and Raman spectroscopy[134]. Subsequently the crystal structure of monoclinic crystal of [C4C1im]Cl was determined independently by Saha et al.[135] and Holbrey et al.[136] It was found that in monoclinic crystal of [C4C1im]Cl the anions arrange as *zigzag* chains[137]. The elucidation of crystal structure is helpful to understand ILs in liquid state as the crystal lattice is still retained upon melting[138].

Intermolecular interactions are generally characterized by far-infrared spectroscopy and THz spectroscopy. Fumino et al.[139] studied the interactions between cations and anions in imidazolium-based ILs with far-infrared spectroscopy and they assigned the low-frequency band between 50 and 120 cm$^{-1}$ to the bending and stretching of the hydrogen bond between cations and anions. In 2012, Fumino et al.[140] measured the far-infrared spectra of tetramethylammonium nitrate ([(CH3)4N][NO3]) and trimethylammonium nitrate ([(CH3)3NH][NO3]) and observed that the far-infrared spectra of [(CH3)3NH][NO3] have a similar band to [(CH3)4N][NO3] at 100 cm$^{-1}$ but [(CH3)3NH][NO3] has an additional band located around 171 cm$^{-1}$. They attributed the band at 100 cm$^{-1}$ to librational motions and the band at 171 cm$^{-1}$ to

vibration of hydrogen bonds between cations and anions. Buffeteau et al.[141] measured the optical constants in mid- and far-infrared region and quantitatively evaluated the intramolecular and interionic vibrations.

In this chapter we address the problem of spectrally separate intra- and inter-molecular vibrational modes by measuring the absorption coefficients and refractive indices of four different imidazolium-based ILs with broadband THz time-domain spectroscopy (THz-TDS) based on the high energy laser-induced plasma THz source presented in chapter 2. To the best our knowledge investigation of ILs with broadband THz, which can reveal both intermolecular and intramolecular interactions and directly access both absorption coefficient and refractive index at the same time, has not been reported yet.

## 5.2. **MATERIALS AND EXPERIMENT**

The four ILs investigated in this chapter are 1-butyl-3-methylimidazolium bis(trifluoromethanesulfonyl)imide ([C4C1im][Ntf2]), 1-butyl-3-methylimidazolium tetrafluoroborate ([C4C1im][BF4]), 1-butyl-3-methylimidazolium iodide ([C4C1im]I) and 1-butyl-3-methylimidazolium chloride ([C4C1im]Cl). They have been purchased from Io-li-tec (http://www.iolitec.de/). The structures of the common cation and the four different anions are shown in **Scheme 4-1** presented in chapter 4. At room temperature [C4C1im]Cl is in solid state and therefore it was heated to melt and measured in its supercooled liquid state at room temperature. Before measurements, the ILs are purified in vacuum for 12 hours in order to remove water and other volatile impurities. All the measurements are conducted at ambient temperature and pressure.

In chapter 4 we investigated mixtures of [C4C1im][Ntf2] and [C4C1im]I with THz-TDS with 250-μm-<110> ZnTe which is capable of detect THz from ~0.1 to ~5 THz. In this chapter, we extended our available frequency range by means of a non-standard detection crystal: LAPC which is a mixture of dye and amorphous polycarbonate as described in chapter 2. The ILs were put into homemade liquid cells made of silicon windows with cell thickness ranging from ~40 to ~ 180 um. ILs samples having different thickness were measured and the absorption coefficient and the refractive index were

extracted by resorting to the Beer-Lambert law. This procedure makes the measurement less dependent on the cell thickness and hence the extraction of the complex refractive index more reliable. Details on the experimental set-up are presented in chapter 2 and the extraction of optical coefficients can be found in appendix.

## 5.3. EXPERIMENTAL RESULTS
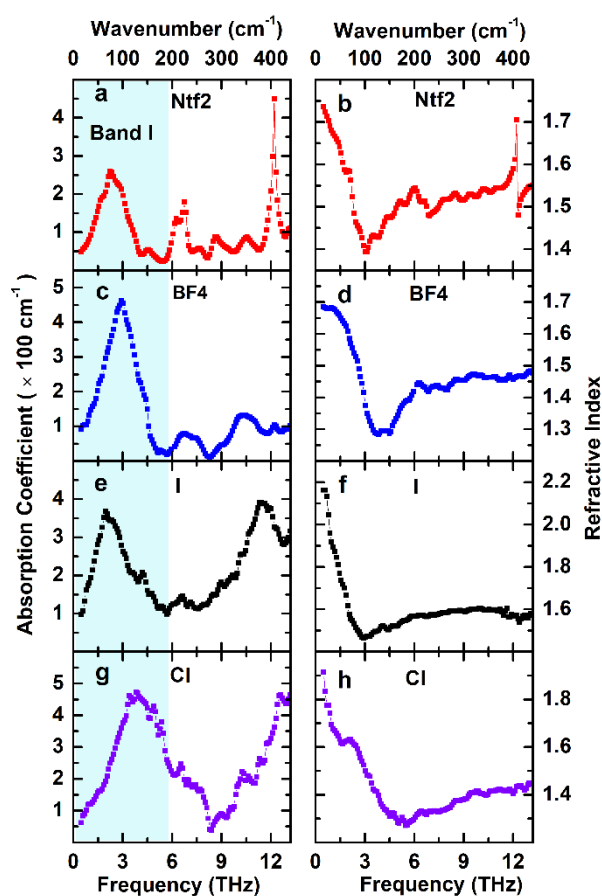


**Figure 5-1.** Absorption coefficient of [C4C1im][Ntf2] (a), of [C4C1im][BF4] (c), of [C4C1im]I (e) and [C4C1im]Cl (g). Refractive index of [C4C1im][Ntf2] (b), of [C4C1im][BF4] (d), of [C4C1im]I (f) and [C4C1im]Cl (h) from 0.5 to 13.2 THz. The intermolecular broad absorption band is highlighted and called band I.

The first row of **Figure 5-1** shows the absorption coefficient (a) and refractive index (b) of [C4C1im][Ntf2] as a function of frequency. In panel (a) it is seen that in the low frequency range, the absorption spectrum has a broad absorption band (band I) centered around 2.2 THz with a full width at half maximum (FWHM) approximately equal to 2.0 THz. In the frequency range around 6 THz the absorption of [C4C1im][Ntf2]

has a doublet structure with two peaks located at 6.2 and 6.8 THz, respectively. In the high frequency region of the spectrum the absorption displays a sharp and strong peak at 12.2 THz. Panel (b) of **Figure 5-1**shows the refractive index of [C4C1im][Ntf2]: it decreases from ~1.74 at 0.5 THz to reach a minimum at 3.0 THz corresponding to the minimum value of ~1.39, then the refractive index increases slowly with a small dip at around 6.8 THz with local minimum equal to ~1.47. A dramatic sharp change appears in the vicinity of 12.2 THz with a local maximum value equal to ~1.70 and local minimum equal to ~1.48.

The second row of **Figure 5-1**displays the absorption coefficient (c) and the refractive index (d) of [C4C1im][BF4]. The main feature of the absorption spectrum is that the band I is centered at 2.9 THz and the FWHM equals ~2.4 THz. Following band I the absorption coefficient spectrum of [C4C1im][BF4] has a small peak around 6.6 THz and another one around 10 THz. The magnitudes of these two peaks are much lower compared to band I. The main characteristic of the refractive index spectrum of [C4C1im][BF4] is its broad dip centered at ~3.0 THz with minimum value equal to ~1.27. In detail, the refractive index of [C4C1im][ BF4] first decreases from ~1.69 at 0.5 THz to ~1.3 at 3.0 THz, then increases up to ~1.45 at 6.0 THz. Finally, the refractive index still increases very slightly in the range from 6.0 to 13.2 THz.

The third row of **Figure 5-1** plots absorption coefficient (e) and refractive index (f) of [C4C1im]I as function of frequency from 0.5 to 13.2 THz. Band I in the absorption spectrum of I is centered at 2.9 THz and the FWHM is equal to ~2.7 THz in the low frequency range and another broad band centered at around 11 THz in the high frequency range. The refractive index of [C4C1im]I decreases from ~2.17 at 0.5 THz to a minimum of ~1.46 at 2.9 THz. From the minimum point the refractive index increases slowly to a shallow local maximum of ~1.6 at around 10.0 THz and then it decreases again slowly from the maximum value.

The fourth row of **Figure 5-1** shows the absorption coefficient (g) and refractive index (h) of [C4C1im]Cl from 0.5 to 13.2 THz. Band I of [C4C1im]Cl is much broader compared to the spectra of the other three ILs. The peak of band I is at ~3.9 THz with FWHM equal to ~3.5 THz. Following band I in the low frequency range the absorption coefficient keeps increasing from ~36.7 cm$^{-1}$ around 8.3 THz to ~470.0 cm$^{-1}$ at 13.2 THz.

The refractive index shown in panel (h) first decreases from ~1.91 at 0.5 THz to a minimum at 5.5 THz with minimum value equal to ~1.27 and then increases slowly up to ~1.45 at 13.2 THz.

## 5.4. **DISCUSSION**

### **5.4.1.** Assignment of Absorption Bands

**Table 5-1**. Values of peak frequency ($\nu_p$), the peak absorption intensity ($\alpha_p$) and FWHM of band I, the frequency of minimum refractive index ($\nu_{min}$), the molecular weight, the antisymmetric vibrational wavenumber of HC(4)-HC(5) ($\omega_{AS}$) and $1/\sqrt{\mu}$ for [C4C1im][Ntf2], [C4C1im][BF4], [C4C1im]I and [C4C1im]Cl.

| ILs | $\nu_p$ (THz) | $\alpha_p$ (cm⁻¹) | FWHM (cm⁻¹) | $\nu_{min}$ (THz) | Molecular Weight | $\omega_{AS}$ (cm⁻¹)[a] | $1/\sqrt{\mu}$ [b] |
|-----|-----|-----|-----|-----|-----|-----|-----|
| Ntf2 | 2.2 | 260.2 | 2.0 | 3.0 | 419.36 | 3122 | 0.138 |
| BF4 | 2.9 | 460.7 | 2.4 | 3.8 | 226.02 | 3120 | 0.153 |
| I | 1.9 | 367.6 | 2.7 | 2.9 | 266.12 | 3078 | 0.14 |
| CL | 3.9 | 470.5 | 3.5 | 5.5 | 174.67 | 3040 | 0.2 |

[a] The values are estimated from literatures[107-108]. Here the antisymmetric vibrational wavenumber of HC(4)-HC(5) is taken as indicator of the strength of hydrogen bond.

[b] The values are taken from reference[107]. Only the methylimidazolium-ring part of cation is considered when calculating $1/\sqrt{\mu}$. As different lengths of side chains nearly don't affect the intermolecular vibration frequencies, it is assumed that the side chains don't contribute to the reduced mass.

The main parameters of the absorption band extracted from the spectra are peak frequency ($\nu_P$), peak absorption intensity ($\alpha_p$), FWHM of band I and the frequency of minimum refractive index ($\nu_{min}$). These four parameters together with the molecular weight, the antisymmetric vibrational wavenumber of HC(4)-HC(5) ($\omega_{AS}$) and $1/\sqrt{\mu}$, where $\mu$ is reduced mass, for the four investigated ILs are listed in **Table 5-1**. $\omega_{AS}$ and $1/\sqrt{\mu}$ will be discussed in detail below.

There is a quite large literature[106-109, 142] discussing the dynamic behavior of ILs in the THz frequency range. According to the investigation in chapter 4 the broad

absorption band in low frequency range from 0.15 to 4.5 THz can be attributed to intermolecular interactions of the ILs.

In chapter 4 we investigated mixtures of [C4C1im][Ntf2] and [C4C1im]I and we simulated the complex permittivity of all mixtures of different volume fractions with a single model. We found that, for each mixture, a combination of three oscillators can fit the experimental results with good approximation. We assigned the lowest-frequency oscillator to rotational diffusion motion and/or diffusive translational motion while the other two oscillators to intermolecular motions.

The assignment of the lowest-frequency oscillator is in good agreement with previous works, while the assignment of the other two oscillators is controversial. Giraud et al.[129] fitted the time-resolved Kerr-effect spectra of five different imidazolium-based ILs with several Brownian oscillators and attributed the first overdamped Brownian oscillator to rotational diffusive motions. Meanwhile, Giraud et al. ascribed the following three Brownian oscillators which appear at the same frequencies around 0.9, 2, and 3 THz (~30, 65, and 100 cm$^{-1}$) to librational motions. Xiao and his coworkers[101] described the main band of optical Kerr effect spectra of ILs with a sum of a low-frequency component, an intermediate-frequency component, and a high-frequency component and they assigned the high-frequency component to librational motion of cation. Stoppa et al.[132] used a combination of four components to depict the dielectric spectra of ILs and ascribed the Debye component at ~0.6 THz and the damped harmonic oscillator at ~2.5 THz to cation libration. Fumino et al.[139,143] ascribed the absorption band below 150 cm$^{-1}$ (4.5 THz) to the bending and stretching of hydrogen bonds formed between the cations and anions. In summary, it is possible to safely conclude that the broad band I of the four investigated ILs originates from intermolecular motions.

Now we turn our attention on the absorption bands in the higher frequency region. To highlight the absorption bands and the corresponding refractive index in this region, the high frequency range of [C4C1im][Ntf2] is plotted again in **Figure 5-2**. In panel (a) of **Figure 5-2** the double peaks (band II) located at 6.2 and 6.8 THz, respectively, stem from the wagging mode of the O-S-O group in the anion of [C4C1im][Ntf2]. This assignment agrees with the explanation by Wulf et al.[144] In

addition, similar intramolecular absorption peaks are also described by Buffeteau et al[141]. According to the vibrational frequencies listed in literature[145] the absorption peak at 12.2 THz (band III) should be also attributed to the same wagging mode.
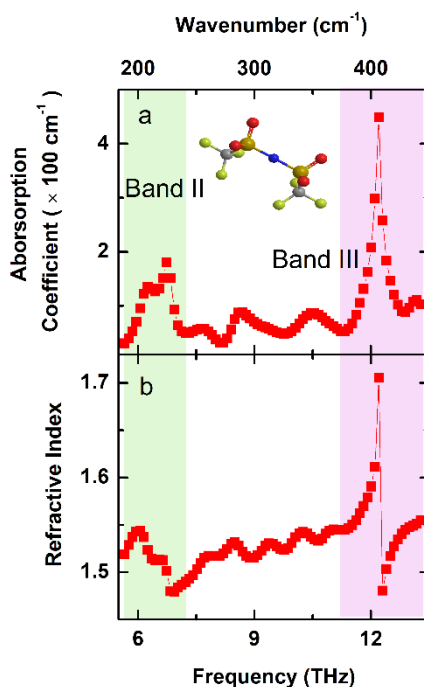


**Figure 5-2.** Absorption coefficient (a) and refractive index (b) of [C4C1im][Ntf2] in high frequency range. Two main absorption bands are found. Band II is a doublet whose peaks locate at 6.2 and 6.8 THz. Band III is an intense sharp peak whose peak locates at 12.2 THz. In refractive index spectrum a dramatic change appears at 12.2 THz.

Apart from the aforementioned peaks, in panel (a) of **Figure 5-2** there are other weak peaks in the absorption spectrum of [C4C1im][Ntf2]. These absorption bands may originate from torsion, twist and bend motions of the groups in cation and/or anion as shown by ab initio calculation done by Heimer et al.[146] For example, Fumino et al.[144] assigned the absorption band at about 270 $cm^{-1}$ to out-of-plane bending mode of CH3-C(2). To consolidate the assignment of all these peaks ab initio calculations[146-147] are necessary. The small absorption bands of [C4C1im][BF4] in the high frequency region can be similarly assigned to torsion, twist and bend motions of the groups in cation. Compared to the absorption spectra of ILs with molecular anions ([C4C1im][Ntf2] and [C4C1im][BF4]), the absorption spectra of ILs with halogen anions have broad absorption band in the high frequency region. We can only speculate that

the broad absorption bands in the high frequency region may originate from the skeletal vibrational modes of the imidazolium ring and it seems that the halogen anions enhance and broaden the absorption band in this region.

### 5.4.2. Peak Frequency of Band I and Refractive Index
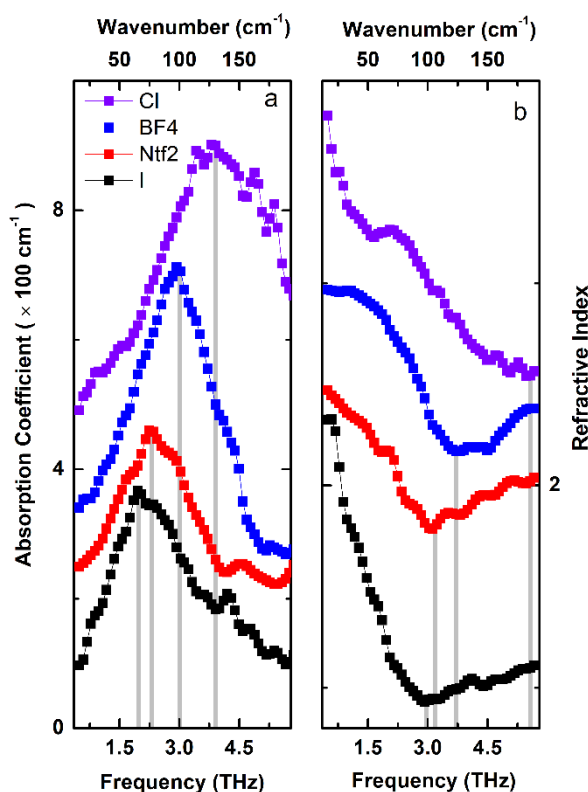


**Figure 5-3.** Absorption coefficient (a) and refractive index (b) in low frequency range. $\nu_P$ and $\nu_{min}$ are highlighted with gray bar. $\nu_P$ of band I is 1.9, 2.2, 2.9 and 3.9 THz for [C4C1im]I, [C4C1im][Ntf2], [C4C1im][BF4] and [C4C1im]Cl respectively. $\nu_{min}$ is 2.9, 3.0, 3.8 and 5.5 THz for [C4C1im]I, [C4C1im][Ntf2], [C4C1im][BF4] and [C4C1im]Cl respectively.

In this subsection we introduce reduced mass $\mu$ and the antisymmetric vibrational wavenumber of HC(4)-HC(5) ($\omega_{AS}$) to discuss $\nu_P$ of band I. In several reports[107-108, 139, 148], the peak frequency of band I was discussed by using approximation of harmonic oscillator which can be expressed with the following formula

$$\nu_p = (k/\mu)^{1/2}, \tag{5-1}$$

where

$$1/\mu = 1/\mu_{cation} + 1/\mu_{anion}. \tag{5-2}$$
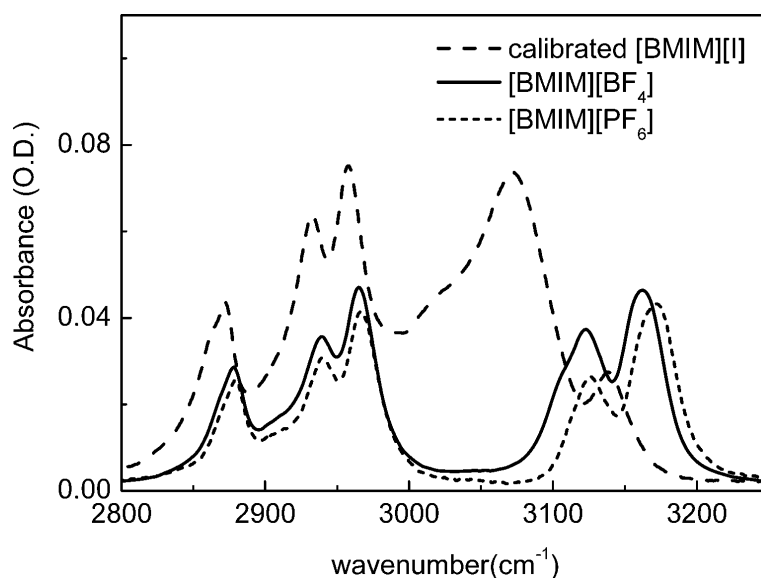


**Figure 5-4.** Attenuated total reflection infrared (ATR-IR) spectra of [C4C1im]I (dashed line), [C4C1im][BF4] (solid line), and [C4C1im][PF6] (dotted line) in the C-H vibration frequency range. Adapted from "Structures of Ionic Liquids with Different Anions Studied by Infrared Vibration Spectroscopy", by Jeon et al., 2008, The Journal of Physical Chemistry B, 112, 4735-4740.Copyright 2008 by "American Chemical Society".

In the above equations k is the "spring" constant, $\mu_{cation}$ and $\mu_{anion}$ denote mass of cation and anion, respectively. In ILs the hydrogen atom attached directly to the imidazolium ring can form hydrogen bond with anions. The hydrogen bond affects C-H vibrations and result in balance between hydrogen bond and intramolecular C-H interaction. This balance make it possible to use C-H vibrational frequency as indicator of hydrogen bond strength. Here we select $\omega_{AS}$ as indicator. An example of infrared spectroscopy of C-H vibrations of ILs is shown in **Figure 5-4**. In the figure, C-H vibration bands of [C4C1im]I are greatly red-shifted compared with [C4C1im][BF4].

From Eq. (5-1) it is clear that both $k$ and $\mu$ affect $\nu_P$. Fumino et al.[148] found the reduced mass and force constant contribute to the frequency shift of $\nu_P$ nearly in the same manner. We will discuss the effects $k$ and $\mu$ on $\nu_P$.
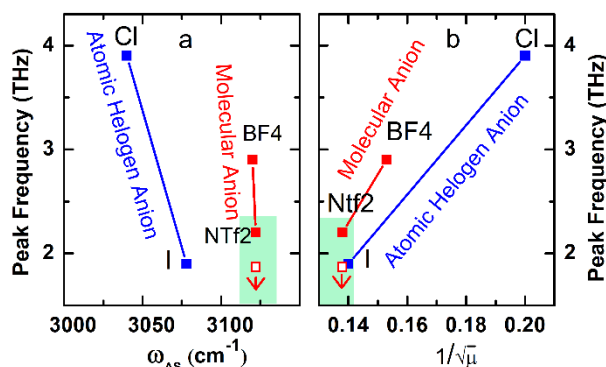
**Figure 5-5.** Peak frequency ($\nu_P$) of band I as function of antisymmetric vibrational wavenumber of HC(4)-HC(5) ($\omega_{AS}$) (a), $\nu_P$ of band I as function of $1/\sqrt{\mu}$ (b). The lines in panel (a) and (b) are guide for eyes. Comparison of expected and experimental $\nu_P$ of [C4C1im][Ntf2] is highlighted. Open square symbol is upper limit of expected $\nu_P$. Arrows indicate expected $\nu_P$ of [C4C1im][Ntf2] should be smaller than upper limit.

Fumino et al.[139] proposed the balance relationship between the hydrogen bond of $^+C - H \cdots A^-$ and the covalent bond of C-H. An enhancement of the hydrogen bond is accompanied by a reduction of the strength of the C-H interaction and vice versa. An enhancement of the hydrogen bond leads to a blue shift of the intermolecular vibration frequency whereas a reduction of the C-H interaction strength leads to a red-shift of the frequency of the C-H vibrational modes. As a result, a blue-shift of the intermolecular vibrations is expected to accompany the red-shift of the C-H vibration frequency. The C-H vibrational modes can be measured by IR spectroscopy in the wavenumber region from 2800 to 3300 cm$^{-1}$. The reported data showed that the expected relation between the blue-shift of intermolecular vibrations and the red-shift of the C-H vibration holds for ILs with molecular anions[139] as well as for ILs with atomic halogen anions[108]. However, this relation is broken when comparing ILs containing molecular anions and ILs containing halogen anions. As shown in panel (a) of **Figure 5-5**, $\nu_P$ of [C4C1im]I is smaller than $\nu_P$ of [C4C1im][Ntf2] although the $\omega_{AS}$ of [C4C1im]I red shifts by ~ 44 cm$^{-1}$.

Panel (b) of **Figure 5-5** plots the relationship of $\nu_P$ and $1/\sqrt{\mu}$. It can be found that $\nu_P$ of [C4C1im][Ntf2] is bigger than $\nu_P$ of [C4C1im]I although $1/\sqrt{\mu}$ of [C4C1im][Ntf2] is smaller. The discrepancy between $\nu_P$ and $\omega_{AS}$ or the discrepancy between the $\nu_P$ and $1/\sqrt{\mu}$ alone cannot draw a conclusion of violation of Eq. (5-1) because $k$ and $\mu$

may not contribute equivalently to $\nu_P$. In the case of [C4C1im][Ntf2] and [C4C1im]I, both blue-shifted $\omega_{AS}$ (smaller $k$) and smaller $1/\sqrt{\mu}$ of [C4C1im][Ntf2] predict red-shifted $\nu_P$ for [C4C1im][Ntf2] according to Eq. (5-1) when compared with [C4C1im]I. However, our experimental results show that $\nu_P$ of [C4C1im][Ntf2] is blue shifted as shown in panel (a) of **Figure 5-3**.

[C4C1im][Ntf2] and [C4C1im]I are the perfect example to show violation of Eq. (5-1) because both blue-shifted $\omega_{AS}$ (smaller $k$) and smaller $1/\sqrt{\mu}$ predict same frequency shift tendency. In contrast, other cases don't predict same frequency shift tendency. For example blue-shifted $\omega_{AS}$ (smaller $k$) of [C4C1im][BF4] predicts red-shifted $\nu_P$ but bigger $1/\sqrt{\mu}$ predicts blue-shifted $\nu_P$ when compared with [C4C1im]I.

In order to quantitively compare the expected and experimental $\nu_P$ of [C4C1im][Ntf2] we calculated the upper limit of expected $\nu_P$ by assuming $k$ of [C4C1im][Ntf2] is same as [C4C1im]I. The calculated result is shown as red open square symbol in **Figure 5-5** where the comparison of expected and experimental $\nu_P$ of [C4C1im][Ntf2] is highlighted with light green shadows. It is clear that even the upper limit of expected $\nu_P$ of [C4C1im][Ntf2] is smaller than $\nu_P$ of [C4C1im]I. The expected $\nu_P$ of [C4C1im][Ntf2] should be smaller that upper limit since $k$ of [C4C1im][Ntf2] is much smaller than that of [C4C1im]I ($\omega_{AS}$ of [C4C1im][Ntf2] is much bigger). The arrows in **Figure 5-5** are intended to show that expected $\nu_P$ is smaller than its upper limit.

It is well demonstrated that the hydrogen bond affects band I[143-144]. The effect is usually explained with Eq. (5-1) which successfully predicts the frequency shift of band I when only considering ILs with halogen anions[108] or ILs with molecular anions[107]. However, in our case, considering only the hydrogen bond is insufficient. We need to account other factors to explain the violation of Eq. (5-1). Libration is one of the most common vibrations in ILs and well investigated but not considered in Eq. (5-1). It is most likely that the librational motions and hydrogen bond have same variation tendency with different anions in ILs containing halogen anions or molecular anions. And the contribution ratio of libration and hydrogen bond to band I is similar in ILs based on halogen anions or ILs based on molecular anions. Thus, Eq. (5-1) can explain

the frequency shift of band I even though Eq. (5-1) is only intended to account for hydrogen bond. In our case, violation of Eq. (5-1) happens probably because the contribution ratio of librational motions and hydrogen bond in ILs based on halogen anions is different from that in ILs based on molecular anions. The different contribution ratios may stem from different molecular arrangement of ILs. Xiao et al.[126] showed that different ILs can form different networks and Jeon et.al[133] suggested the microscopic structure is different in [C4C1im][BF4] and [C4C1im]I.

Finally we discuss the refractive index spectra of [C4C1im][Ntf2], [C4C1im][BF4], [C4C1im]I and [C4C1im]Cl. In the refractive index spectra plotted in panel (b), (d), (f) and (h) of **Figure 5-1**, each refractive spectrum curve has a minimum point, $\nu_{min}$, highlighted in panel (b) of **Figure 5-3**. It is shown that $\nu_{min}$ shifts in the same direction as $\nu_P$. Moreover, $\nu_{min}$ is greater than $\nu_P$ for each sample. As a result, minimum of refractive index appears at higher frequency compared with the maxima points in absorption spectra. Each refractive index for the four ILs first decrease from their value at the lowest frequency to the minimum point and then increase to a relatively stable level with the notable exception of the intramolecular vibrational modes of the anion in [C4C1im][Ntf2], which contribute significantly to its refractive index resulting in a dramatic change of the refractive index as shown in panel (b) of **Figure 5-2**. Apart from the dramatic change in the refractive index of [C4C1im][Ntf2] the overall tendencies of all the refractive index spectra are similar.

### 5.4.3. FWHM and Peak Intensity of Band I

The FWHM of band I is 2.0, 2.4, 2.7 and 3.5 THz for [C4C1im][Ntf2], [C4C1im][BF4], [C4C1im]I and [C4C1im]Cl, respectively. Panel (a) of **Figure 5-6** plots the relationship between FWHM of band I and $\nu_P$. It can be seen that the FWHM for ILs with halogen anions is enhanced compared to ILs with molecular anions. The FWHM of [C4C1im]I is much larger than FWHM of [C4C1im][Ntf2] and [C4C1im][BF4] even though $\nu_P$ of [C4C1im]I is lower.
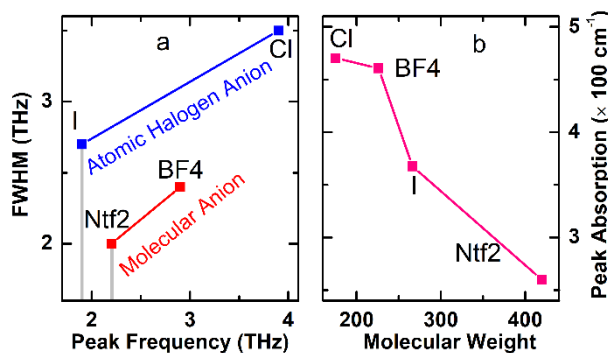
**Figure 5-6.** FWHM of band I as function of peak frequency (a) and peak absorption intensity of band I as function of molecular weight (b). The lines in the figure are guide for eyes. FWHM of [C4C1im]I is bigger than that of both [C4C1im][Ntf2] and [C4C1im][BF4] although $\nu_P$ of [C4C1im]I is smaller.

Shirota and Castner[149] compared the optical Kerr spectra of 1-methoxyethylpyridinium dicyanoamide (MOEPy$^+$/DCA$^-$) with the optical Kerr spectra of analogous isoelectronic neutral binary mixture of 1-methoxyethylbenzene and dicyanomethane (MOEBz/DCM). They found the FWHM of optical Kerr spectrum of MOEPy$^+$/DCA$^-$ in the low frequency region is broader than that of MOEBz/DCM. Meanwhile, the peak of optical Kerr spectrum of MOEPy$^+$/DCA$^-$ in the low frequency region appears at higher frequency compared with MOEBz/DCM. Xiao et al[101] suggested the FWHM of the Kerr spectrum reflects the strength of the interionic interactions. However, the FWHM of [C4C1im]I is much bigger than FWHM of both [C4C1im][Ntf2] and [C4C1im][BF4]. This discrepancy can be similarly interpreted with the same explanation provided above for the violation of Eq. (5-1). The enhancement of FWHM of band I with halogen anions probably stems from the different molecular arrangements and different librational motions between the ILs containing molecular anions and the ILs containing atomic halogen anions. On the other hand, we can say that the discrepancy between the FWHM and $\nu_P$ provides a further evidence for our explanation of the origin of violation of Eq. (5-1).

Panel (b) of **Figure 5-6** plots the relation between the peak absorption intensity ($\alpha_p$) of band I and molecular weight. It is clearly shown that $\alpha_p$ decreases with the increase of molecular weight of ILs. Thus, $\alpha_p$ increases with $1/\sqrt{\mu}$. A similar result has been reported by Yamada and his coworkers[107-108] on imidazolium-based ILs paired with molecular anions and halogen anions. They found that the absorption intensity

normalized by molar concentration at the peak of the absorption band in the lowest frequency region is approximately inversely proportional to the molecular weight of the ionic pairs of ILs. This tendency is reasonable because the molecular weight of ionic pairs is physically related to the size of the ion pairs and the distance of ion pairs[107]. Small molecular weight usually correspond to small volume of ion pairs. In a given volume there are more small ion pairs, which results in higher absorption intensity.

## 5.5. **CONCLUSION**

We investigated imidazolium-based ILs of [C4C1im][Ntf2], [C4C1im][BF4], [C4C1im]I and [C4C1im]Cl with broadband THz spectroscopy in the frequency region from 0.5 to 13.2 THz. We first discussed the assignment of the absorption bands. Then we focused on band I in the lowest frequency region. We discussed the peak frequency, bandwidth (FWHM), peak absorption intensity of band I. We also discussed the refractive index spectra. With broadband THz technology we can record the intermolecular vibrational modes and intramolecular vibrational modes at the same time, making straightforward any relative comparison of the intensity peaks.

We have found that band I dominating the lowest frequency region is broad for all the investigated ILs. The peak absorption intensity $\alpha_p$ of band I increases inversely with molecular weight and consequently increases with $1/\sqrt{\mu}$. However, the shift of peak frequency $\nu_P$ neither vary with antisymmetric vibrational wavenumber of HC(4)-HC(5) $\omega_{AS}$ nor with $1/\sqrt{\mu}$ as expected. True violation of Eq. (5-1) is confirmed when comparing $\nu_P$ with both $\omega_{AS}$ and $1/\sqrt{\mu}$ for [C4C1im][Ntf2] and [C4C1im]I. This violation may originate from the different molecular arrangements and/or librational motions that are present in ILs containing molecular anions as compared to those containing atomic halogen anions. An unexpected behavior of the FWHM of band I as a function of $\nu_P$ is also unveiled. The FWHM for ILs with halogen anions is larger than that of ILs with molecular anions. This anomalous behavior further supports the explanation provided for the violation of Eq. (5-1). In the high frequency region, a doublet whose peaks are located at 6.2 and 6.8 THz and an intense sharp peak at 12.2 THz are clearly displayed in the absorption spectrum of [C4C1im][Ntf2] besides other

small peaks. The doublet and the intense peak at 12.2 THz origin in the wagging mode of the O-S-O group in the anion. For [C4C1im][BF4] there are only some small peaks in the high frequency region. There are broad absorption bands in the high frequency region for [C4C1im]I and [C4C1im]Cl. The broad absorption bands in the high frequency region for [C4C1im]I and [C4C1im]Cl probably origin in the skeletal vibrational modes of the imidazolium ring. All the refractive index spectra of the investigated ILs have a minimum point, $\nu_{min}$, which increases with $\nu_P$. $\nu_{min}$ appears at higher frequencies as compared to $\nu_P$. In addition, the overall variation of the refractive index is similar for all the ILs. However, it is worth noting that the strong intramolecular vibrations in anion of [C4C1im][Ntf2] result in dramatic changes in its refractive index spectrum. In particular, the intense intramolecular vibrational mode at 12.2 THz leads to a singularity in the refractive index spectrum.

# Chapter 6.    THz-Pump / SHG-Probe

## 6.1.  INTRODUCTION

Up to now, THz is widely used in terahertz time-domain spectroscopy (THz-TDS) and time-resolved THz spectroscopy (TRTS). Wald et al.[150] added an additional laser to pump $YBa_2Cu_3O_{7-\delta}$ based on the traditional THz emission spectroscopy to measure the time-resolved evaluation of the hot carrier excitation and relaxation. Shi et al.[151] researched optical pump effect on THz emission from unbiased semi-conducting GaAs with experimental scheme similar to that used by Wald et al.[150] In their research, Shi et al. found the transient photoconductivity induced by pump pulses affects temporal waveform of terahertz radiation pulse. Li et al.[152] investigated carrier dynamics and terahertz conductivity in optically pumped ZnSe nanocrystal with THz-TDS. There are also some reports on research using THz as pump. Thompson et al.[153] found transient insulator-to-metal transition triggered by high-field THz pulse in a nanoantenna patterned vanadium dioxide thin film. Bowlan et al.[154] used THz to resonantly drive phonon mode in in the topological insulator $Bi_2Se_3$ and probed the structural dynamics induced by THz using SHG. Baierl et al.[155] used THz magnetic fields to drive magnon resonances in nickel oxide and probed the induced dynamics. In this chapter we pump quartz with intensive broadband THz and probe the resulting effects induced by THz with SHG.

## 6.2.  EXPERIMENT

The setup of experiment is shown in **Figure 2-1** presented in chapter 2. The detail configuration of the pump/probe part is shown in the inset of **Figure 2-1**. In the setup, the sample is pumped with intensive broadband THz generated in laser-induced plasma via four-wave-mixing process coupling the fundamental laser and its second harmonic wave. Meanwhile the laser beam in the probe arm impinges on the sample collinear with THz wave. The second harmonic generation (SHG) of the fundamental probe is detected by photomultiplier and the wavelength of the SHG is selected by a monochromator. In order to investigate the effects of polarization of both THz and probe on SHG a THz polarizer is inserted in the THz arm and a half wave plate is

inserted in the probe arm to change polarizations. We carried out THz-Pump/SHG-Probe experiment on 500 µm X- and Y-cut quartz and discussed the results of Y-cut quartz in detail. The time-dependent SHG signal is recorded by a photomultiplier at different time delay between the probe pulse and THz pulse, which is similar to the coherent THz detection with air sensor[67].

## 6.3. **RESULTS AND DISCUSSION**

### **6.3.1.** Effect of Cut Direction
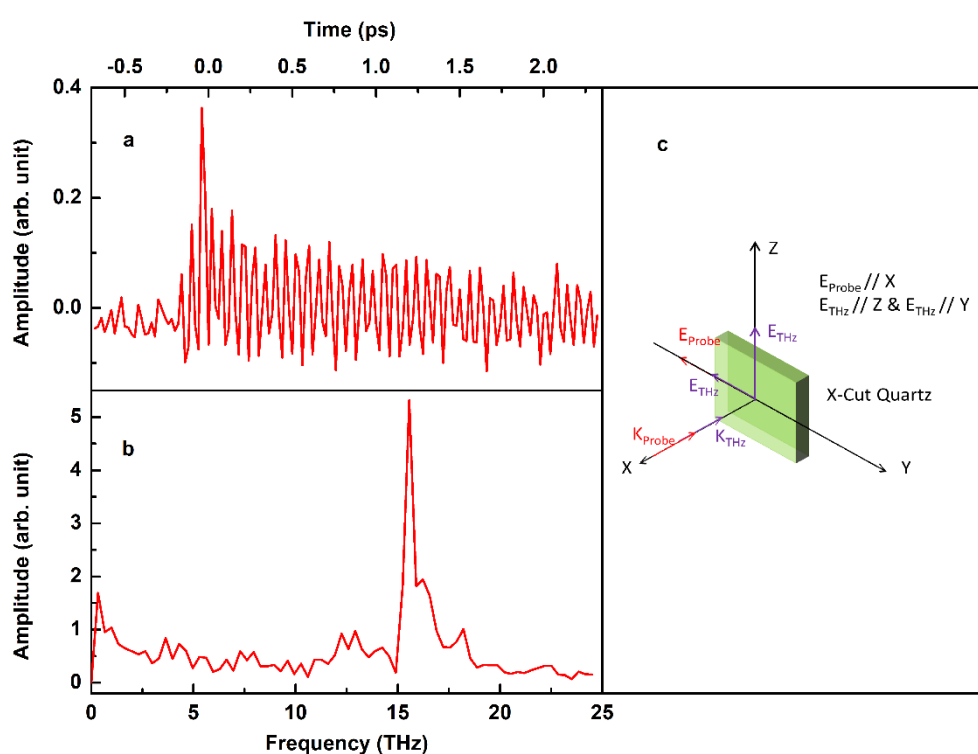


**Figure 6-1.** Time-domain signal of SHG from 500 µm X-cut quartz (a) and its Fourier transformation (b). The relation of THz polarization, probe polarization and orientation of X-cut quartz is shown in panel (c) and monochromator is at 400 nm.

Panel (a) and (b) of **Figure 6-1** respectively show time-dependent SHG signal at wavelength of 400 nm and its Fourier transformation. The experiment is conducted with THz having polarization components both parallel and orthogonal to Z axis of the sample. The polarization of probe is parallel to Y axis. The relation of THz polarization, probe polarization and sample orientation is shown in panel (c). Sample thickness is 500 µm. The time in panel (a) is the time delay between probe pulse and THz pulse.

THz pulse locates at time equal to zero. The time delay of probe pulse with respect to THz pulse is realized by moving the delay line shown in the setup presented in chapter 2. It is clear that the time-dependent SHG has obvious oscillations in panel (a) of **Figure 6-1**. The Fourier transformation of time-dependent signal shown in panel (b) has a prominent peak around 16 THz.
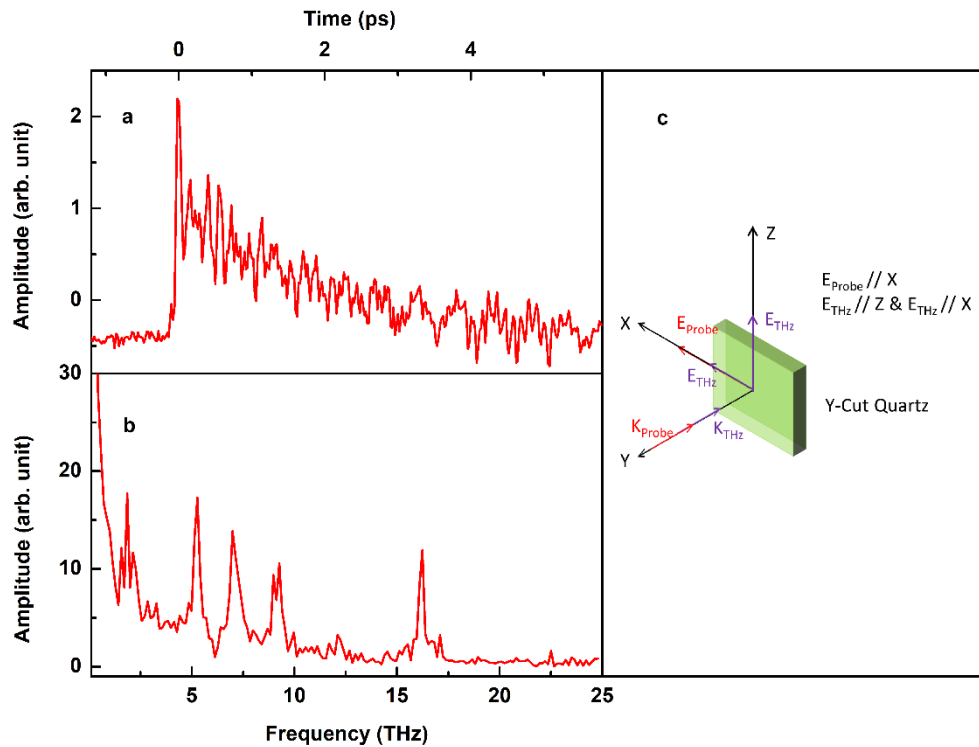


**Figure 6-2.** Time-domain signal of SHG from 500 μm Y-cut quartz (a) and its Fourier transformation (b). The relation of THz polarization, probe polarization and orientation of Y-cut quartz is shown in panel (c) and monochromator is at 400 nm.

Panel (a) and (b) of **Figure 6-2** respectively plot time–dependent SHG and its Fourier transformation in Y-cut quartz. THz has one polarization component parallel to X axis and another one parallel to Z axis. Polarization of probe is parallel to X axis. The relation of THz polarization, probe polarization and sample orientation is shown in panel (c). Monochromator is at 400 nm and sample thickness is 500 μm. Time-dependent signal shown in panel (a) increases quickly to maximum at time equal to zero and then relaxes slowly to zero with obvious oscillations. The frequency-domain signal shown in panel (b) has obvious peaks around 2.1, 5.2, 7 9.2 and 16.1 THz.

We also measured Z-cut sample but no oscillation is observed. In addition, we also measured samples having different thicknesses and no obvious effect of thickness on SHG is found. In the following we focus on the effect of THz pump on SHG in Y-cut quartz with thickness of 500 μm.

### 6.3.2. SHG at Different Wavelengths
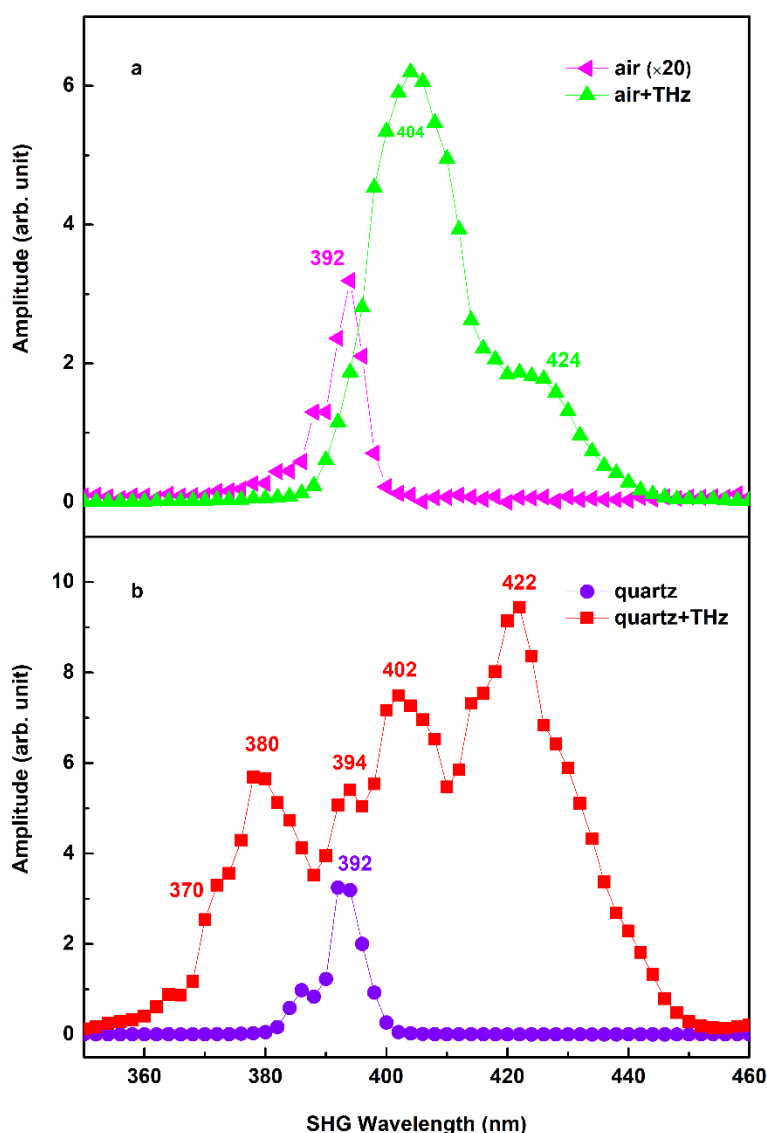


**Figure 6-3.** Spectra of SHG generated in air with and without THz (a): in air without THz (full magenta triangular symbol), in air with THz (full green triangular symbol). Spectra of SHG generated in quartz with and without THz (b): in quartz without THz (full blue circular symbol), and in quartz with THz (full red square symbol). THz pump polarization, probe polarization and orientation of the sample are same as those shown in panel (c) of **Figure 6-2.**

To deepen the investigation we made a spectral analysis of the SHG light emitted in air and Y-cut quartz with and without THz by recording the photomultiplier output versus the monochromator wavelength. Full green triangular symbol and magenta triangular symbol in panel (a) of **Figure 6-3** respectively show the spectra of SHG generated in air with and without THz. Red square symbol and blue circular symbol in panel (b) of **Figure 6-3** respectively show the spectra of SHG generated in quartz with and without THz. The spectrum of SHG generated in air without THz has only one peak around 392 nm while the spectrum of SHG generated in air with THz has a broader red-shifted peak around 404 nm and a shoulder around 424 nm. Compared with the spectrum of SHG in air without THz, the spectrum of SHG in air with THz shows enhanced intensity, wider bandwidth and red-shifted peak. Similar to the spectrum of SHG generated in air without THz, the spectrum of SHG generated in quartz without THz has only one peak at 392 nm. However, the spectrum of SHG generated in quartz with THz is absolutely different to the spectrum of SHG generated in air with THz. The spectrum of SHG generated in quartz with THz has 4 peaks around 380, 394, 402 and 422 nm and a shoulder around 370 nm. Compared with the spectrum of SHG in quartz without THz, the spectrum of SHG in quartz with THz presents enhanced intensity, wider bandwidth and red-shifted peak.

In order to investigate the oscillations of SHG at different wavelengths we recorded SHG signals at several wavelengths versus the time delay between THz pulse and probe pulse. Panel (a) of **Figure 6-4** plots signal of SHG versus time delay at different wavelengths of SHG and panel (b) shows the Fourier transformation of each signal in panel (a). In panel (a) it is shown that the curves of 395, 400, 405 and 410 nm increase very quickly at time equal to zero. The curves of 395, 400, 405 nm have oscillations following the peak at time equal to zero and the signal intensity decreases with time while the curve of 410 nm has no clear oscillation. Compared to the other curves in panel (a), the curves of 385 and 390 nm have only oscillations. Fourier transformations of the signals are plotted in panel (b). Signal of 410 nm has no clear peak in high frequency range. Curve of 405 nm has all peaks shown in other curves at 2.1, 5.2, 7, 9.2 and 16.2 THz. Peak at 2.1 THz shows in all the curves. Peak at 16.2 THz shows in curves of 395, 400 and 405 nm. Peak at 9.2 THz shows in curves of 385, 390,

400 and 405 nm. Peak at 7 THz shows only in curves of 400 and 405 nm while peak at 5.2 THz shows only in curve of 395 and 400 nm.
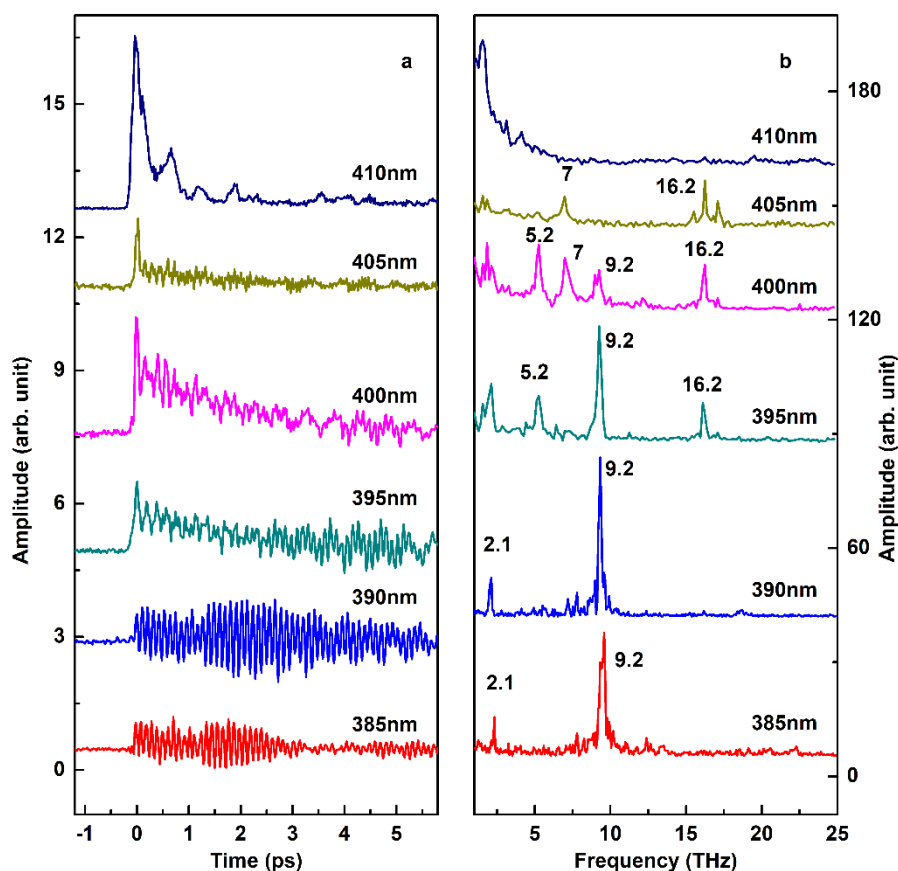


**Figure 6-4.** Time-domain signal of SHG (a) at different wavelength in the range from 385 to 415 nm with step of 5 nm. Fourier transformation results (b) of each signal in time domain at different wavelengths. Numbers in panel (b) are frequencies in THz unit. THz pump polarization, probe polarization and orientation of the sample are same as those shown in panel (c) of **Figure 6-2**

As the experiments were carried out in air. The SHG can also be generated in air via four-wave-mixing process coupling THz and probe beams. To confirm the phenomena found in **Figure 6-4** are originated in quartz we compared typical signals in the presence of THz at wavelengths of 385 and 405 nm obtained in air with and without quartz at the sample position. Figure 6-5 shows the comparison. The time-domain signals at 385 nm in panel (a) display that the SHG from quartz has clear oscillations and the signal of air is nearly null. Panel (b) shows that the signal of quartz at wavelength of 405 nm has oscillations while that of air has no oscillations. Panel (c) and (d) clearly show the oscillations in quartz in frequency domain while no oscillation

is observed in air. This comparison clearly shows that the oscillations observed **Figure 6-4** are generated in quartz.
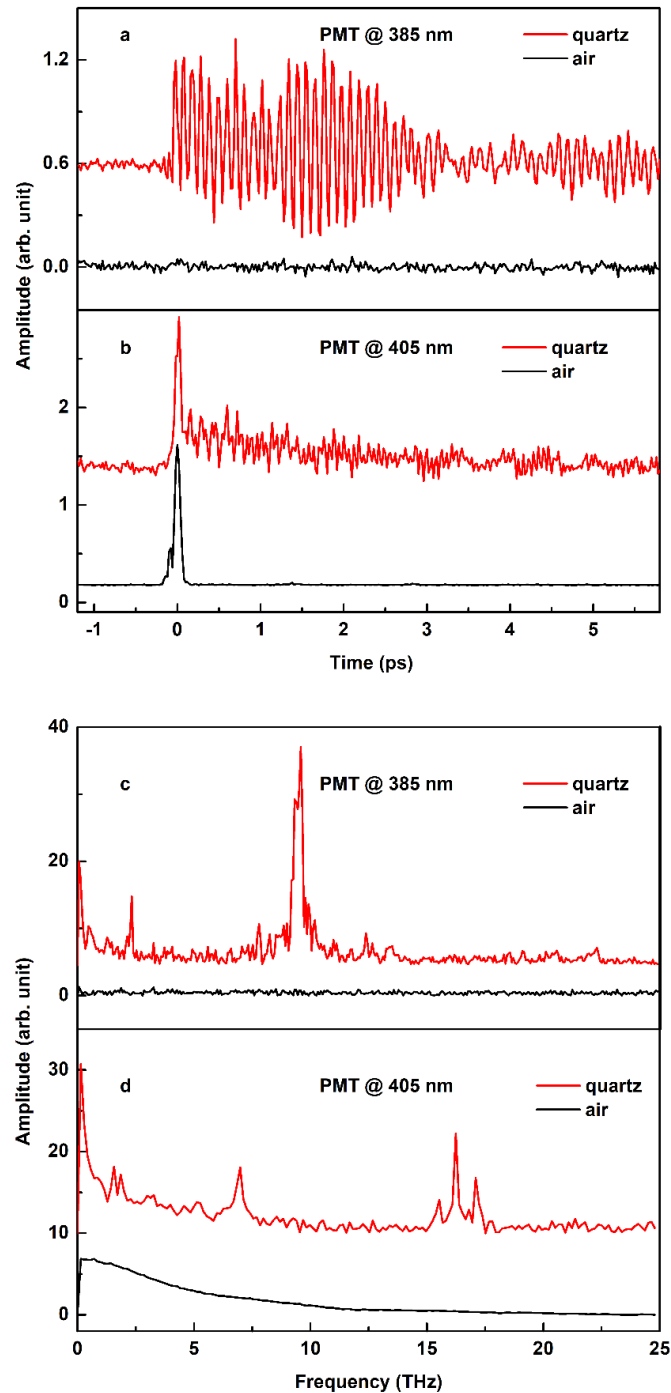


Figure 6-5. Comparison of SHG generated in quartz and air with THz at 385 nm in time domain (a) and frequency domain (c). Comparison of SHG generated in quartz and air with THz at 405 nm in time domain (b) and frequency domain (b). THz pump polarization, probe polarization and orientation of the sample are same as those shown in panel (c) of **Figure 6-2.**

Plendl et al.[156] reported far infrared spectra of $SiO_2$ polymorphs and found that absorption bands of quartz locate at 25.5, 37.6 and 77.6 µm (~ 11.7, 7.97, 3.87 THz) which are different to the oscillation frequencies found in this chapter. It seems that the oscillations found in this chapter don't result directly from phonons. However, it is possible that the oscillations stem from processes coupling more than one phonons similar to hyper-Raman scattering[157].

### 6.3.3. Effect of Probe Power on SHG
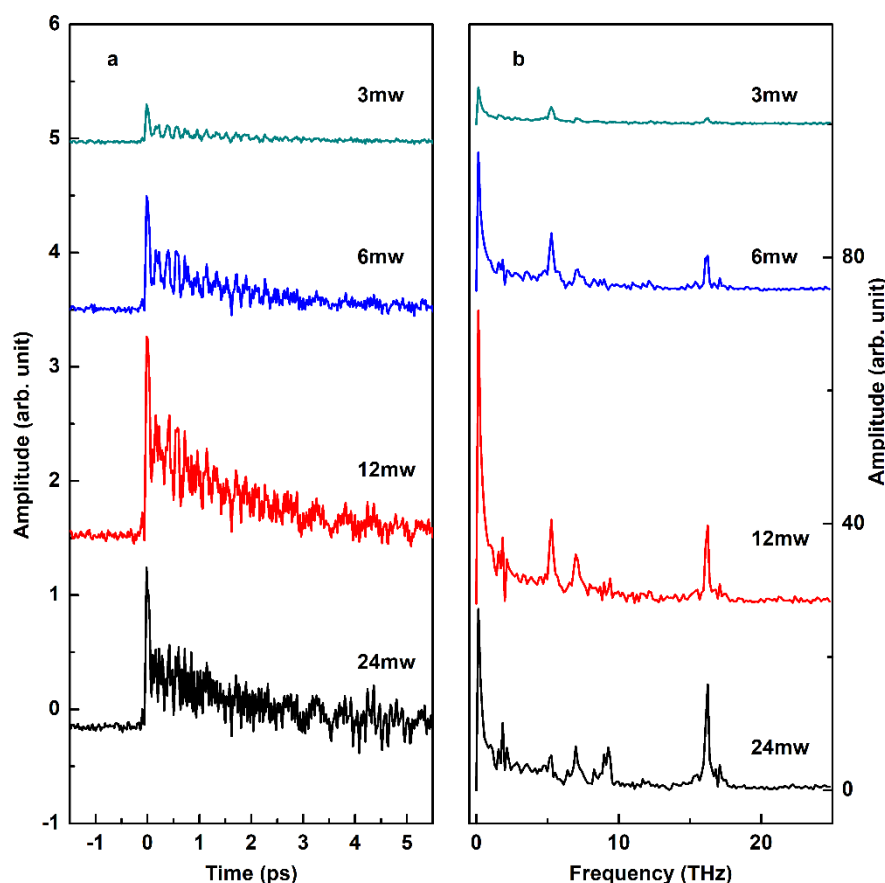


**Figure 6-6.** Effect of probe power on SHG. Intensity of SHG versus time delay (a) in time domain and its Fourier transformation (b) in frequency domain with probe power equal to 3, 6, 12and 24 mW respectively. THz pump polarization, probe polarization and orientation of the sample are same as those shown in panel (c) of **Figure 6-2**.

**Figure 6-6** shows the time-domain signal of SHG recorded with monochromator at 400 nm and probe power equal to 3, 6, 12and 24 mW respectively. The measurements are carried out with same THz pump polarization, probe polarization and orientation of the sample as those shown in panel (c) of **Figure 6-2**. It can be found

that there is no other effect except for the reduction of magnitude of the signals with decreasing probe power.

Panel (a) of **Figure 6-7** plots the SHG spectra with THz power equal to 64 µW and probe power equal to 6, 12 and 24 mW. It can be observed that the magnitudes of the spectra scale down with decreasing probe power. We speculated that the two central peaks in the spectra result from four-wave–mixing process coupling one THz photon and two fundamental probe photons while the peaks located at the two sides stem from five-wave-mixing process coupling two THz photon and two fundamental probe photons. In both of these two schemes, the intensity of SHG will vary quadratically with probe power.
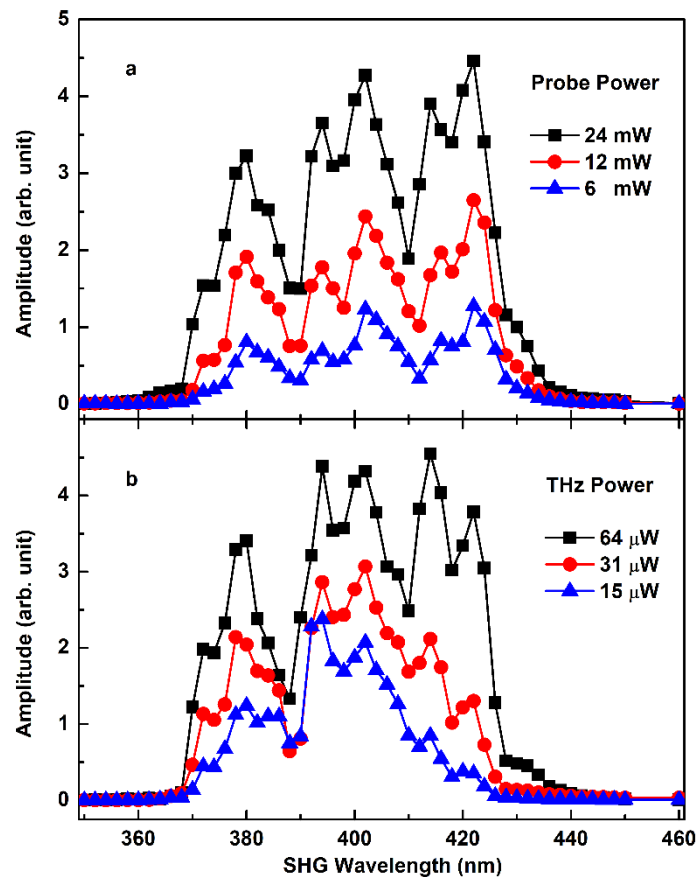


**Figure 6-7.** Spectra of SHG with THz power equal to 64 µW and probe power equal to 6, 12, 24 mW (a) and spectra of SHG with probe power equal to 24 mW and THz power equal to 15, 31, 64 µW. THz pump polarization, probe polarization and orientation of the sample are same as those show in panel (a) of **Figure 6-2**.

Panel (b) of **Figure 6-7** draws the SHG spectra with probe power equal to 24 mW and THz power equal to 15, 31 and 64 µW. THz power is reduced by inserting silicon wafers in the THz beam. In contrast with panel (a) where at different wavelength the magnitude decrease in the same manner, the spectra in panel (b) reduces in different ways in shorter, central and longer wavelength ranges. The speculation of four-wave–mixing process in central wavelength range and five-wave-mixing process at sides can explain the different variation tendencies of SHG versus THz power in different SHG wavelength ranges. According to the speculation the central part of SHG spectra varies linearly with THz power while quadratically at the two sides.

### 6.3.4. Effect of Polarization of THz on SHG
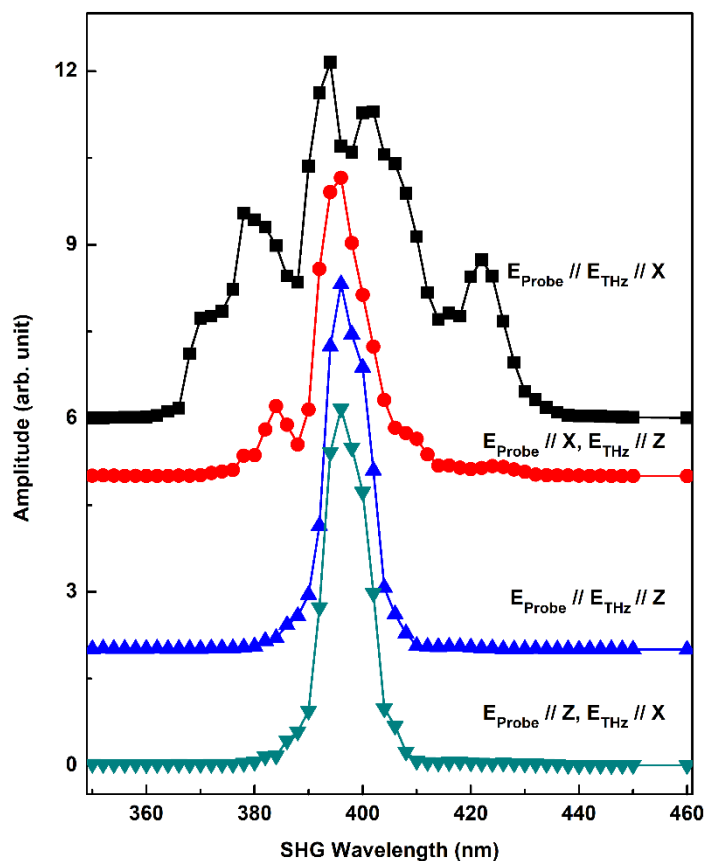


**Figure 6-8.** Spectrum of SHG with $E_{Probe}$ // $E_{THz}$ // X (full black square symbol) as shown in panel (a) of **Figure 6-9,** with $E_{Probe}$ // X and $E_{THz}$ // Z (full red circular symbol) as shown in panel (a) of **Figure 6-10**, with $E_{Probe}$ // $E_{THz}$ // Z (full blue triangular symbol) and with $E_{Probe}$ // Z and $E_{THz}$ // X (full dark cyan triangular symbol).
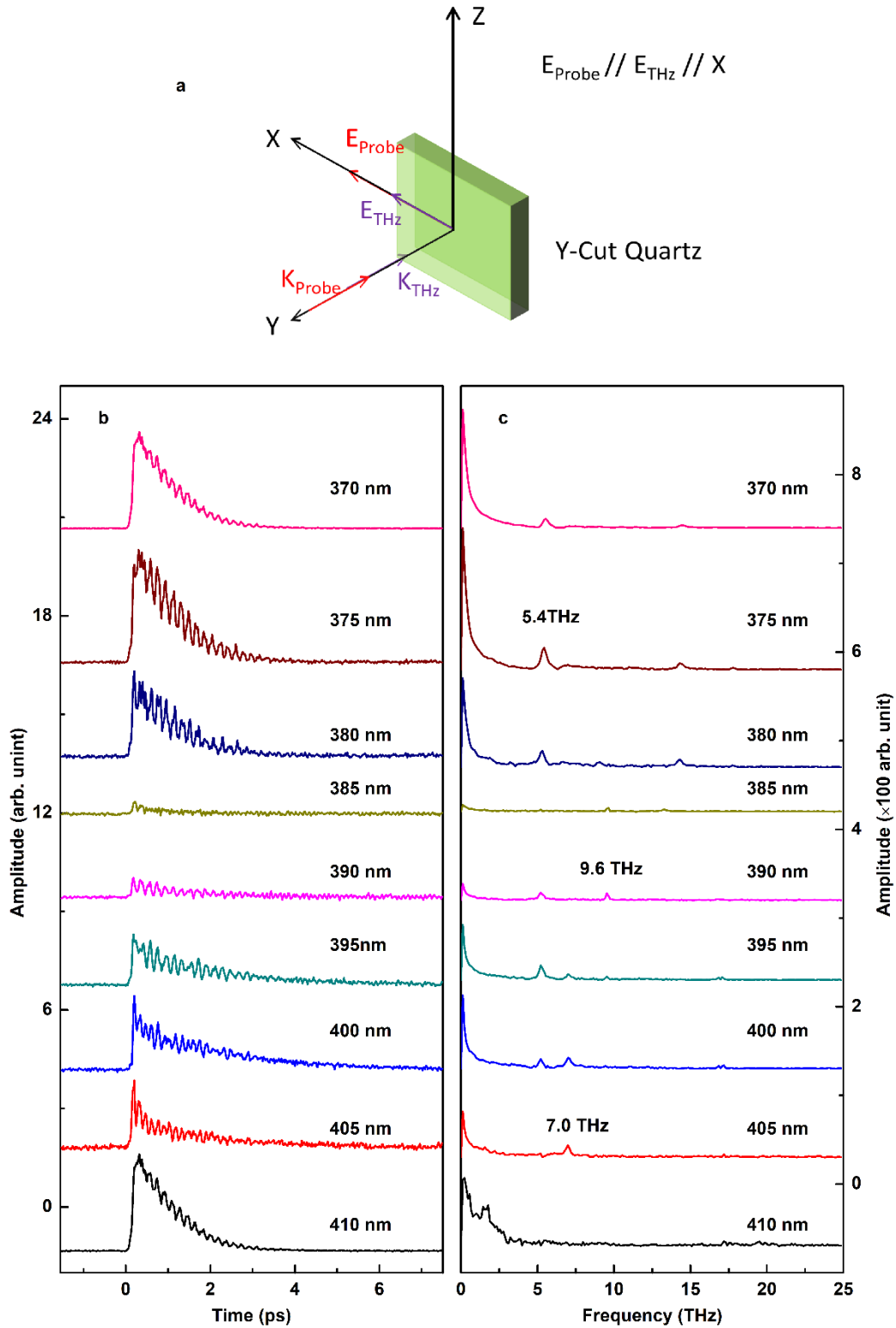
**Figure 6-9.** SHG at different wavelengths with THz pump polarization, probe polarization and orientation of the sample shown in panel (a). Time-domain signal of SHG (b) at different wavelength in the range from 370 to 410 nm with step of 5 nm. Fourier transformation (c) of each signal in time domain at different wavelengths. Numbers in panel (c) are frequencies in THz unit.
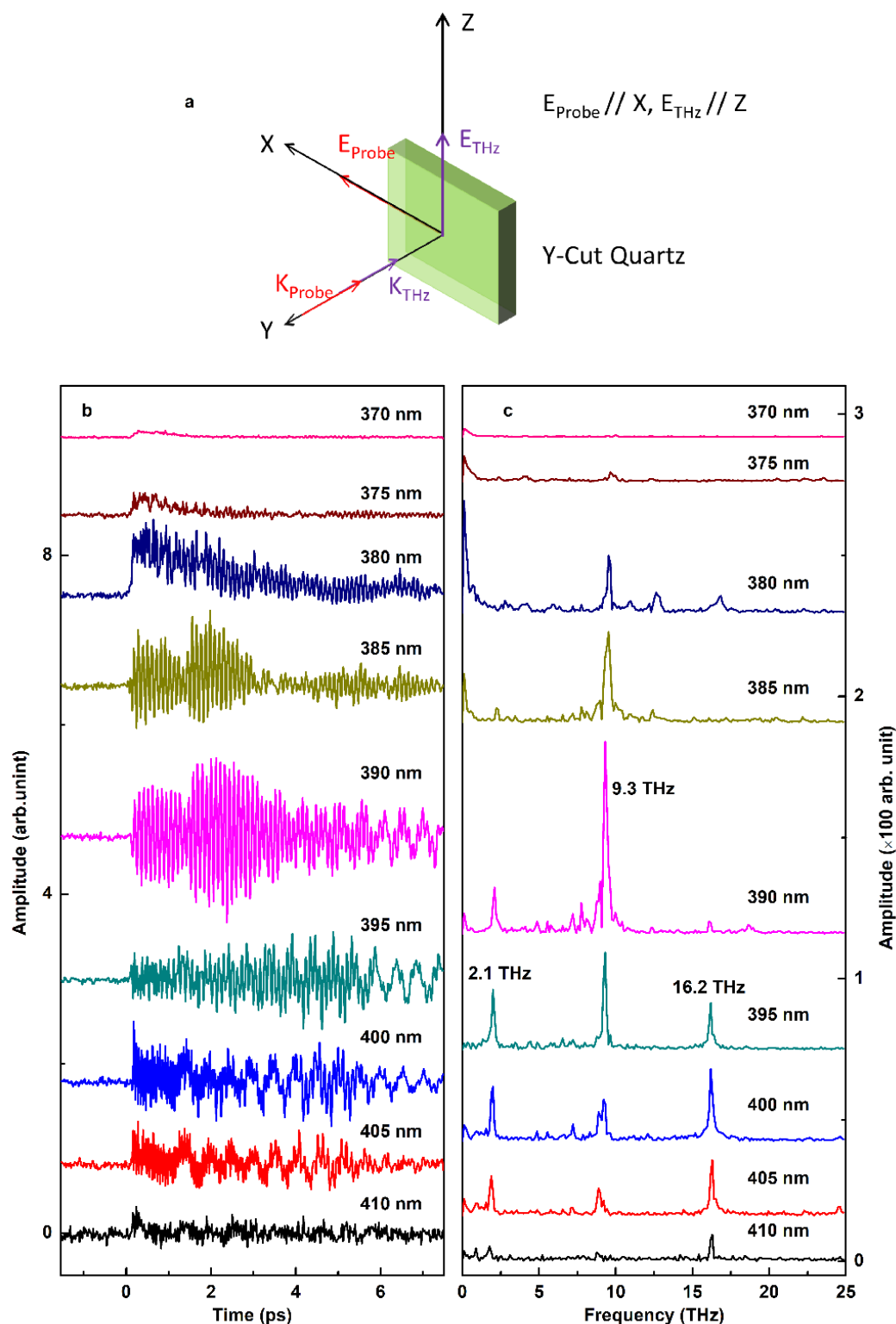
**Figure 6-10.** SHG at different wavelengths with THz pump polarization, probe polarization and orientation of the sample shown in panel (a). Time-domain signal of SHG (b) at different wavelength in the range from 370 to 410 nm with step of 5 nm. Fourier transformation (c) of each signal in time domain at different wavelengths. Numbers in panel (c) are frequencies in THz unit.**Figure 6-8** shows the spectra of SHG with different compositions of THz

polarization, probe polarization and sample orientation. It is shown that the spectrum of SHG with $E_{Probe}$ // $E_{THz}$ // X has widest bandwidth and more peaks. The spectrum of SHG with $E_{Probe}$ // X and $E_{THz}$ // Z has an intensive peak at ~ 392 nm and a much less intensive peak at ~ 383 nm. The spectra with $E_{THz}$ // Z and $E_{THz}$ // X have only one similar peak at ~ 392 nm when $E_{Probe}$ is parallel to Z axis.

**Figure 6-9** draws temporal SHG signals at different wavelengths in panel (b) and their Fourier transformations in panel (c) with THz polarization, probe polarization and orientation of sample shown in panel (a). The signals in panel (b) of **Figure 6-9** increase very quickly at time equal to zero and then relax slowly to zero with oscillations.

Panel (a) of **Figure 6-10** shows the relations of THz polarization, probe polarization and sample orientation. Panel (b) and (c) of **Figure 6-10** respectively plot temporal SHG signals at different wavelengths and their Fourier transformations. In contrast with the curves shown in panel (b) of **Figure 6-9**, panel (b) of **Figure 6-10** shows that oscillation is the dominant characteristic for each curve. In **Figure 6-10**, both the time-domain curves in panel (b) and frequency-domain curves in panel (c) indicate that the intensity of oscillation is strongest around 390 nm, which is different to the case of panel (b) of **Figure 6-9** where the signal at 390 nm is the weakest one. In panel (c) of **Figure 6-10** the peaks are located at ~ 2.1, 9.3 and 16.2 which are also different to those found in **Figure 6-9** where the peaks are at ~ 5.4, 7.0 and 9.6 THz.

In addition, we also recorded the SHG signals versus time delay with $E_{Probe}$ // Z composed with either $E_{THz}$ // Z or $E_{THz}$ // X and didn't found neither oscillation in time domain nor peak in frequency domain.

## 6.4. **THZ SPECTROSCOPY OF QUARTZ**

In this subsection, we show THz-TDS results of Y-cut quartz to compare the frequencies of oscillations found above with central frequencies of THz absorption bands. As the power spectrum is enough to show THz absorptions we herein focus on the power spectrum obtained with THz-TDS. Same to the spectroscopy of imidazolium-based ILs in chapter 5, THz-TDS results of quartz presented in this chapter are also obtained with LAPC detector. In the above section we found that THz

polarization has effects on the time-dependent SHG. In the THz-TDS of Y-cut quartz we carried out the experiment with configurations of $E_{THz}$ // Z and $E_{THz}$ // X.
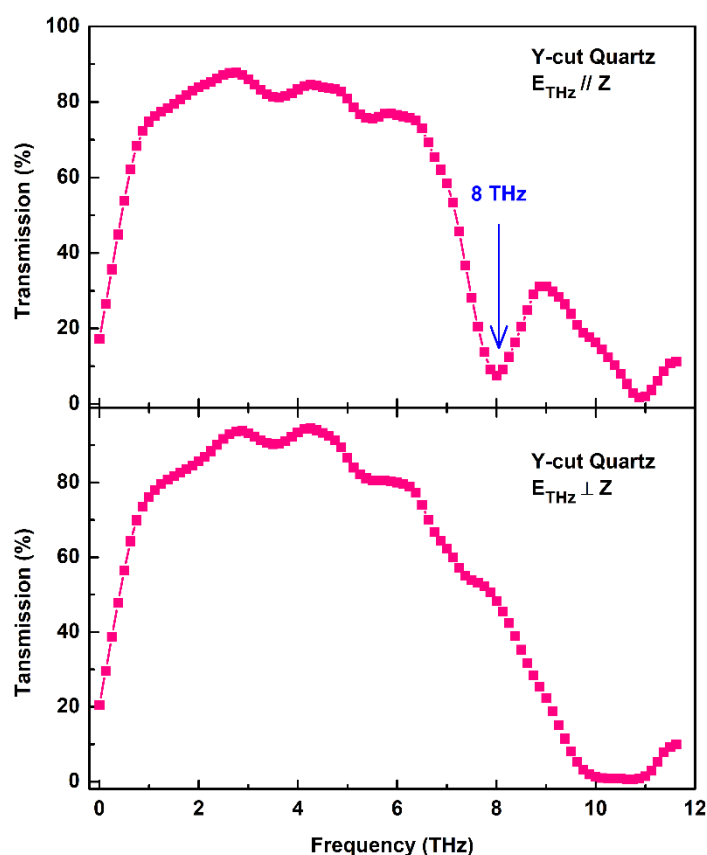


**Figure 6-11.** THz power transmission percentage in Y-cut quartz with $E_{THz}$ // Z (a) and $E_{THz}$ // X (b). Z and X are axes of Y-cut quartz as shown in panel (c) of **Figure 6-2**.

Panel (a) and (b) of **Figure 6-11** respectively plot THz power transmission percentage in Y-cut quartz with $E_{THz}$ // Z and $E_{THz}$ // X. It is clear from the figure that Y-cut quartz is very transparent to THz in the range from ~1 to 7 THz for both the configurations of $E_{THz}$ // Z and $E_{THz}$ // X. The most obvious difference between the curve of $E_{THz}$ // Z and that of $E_{THz}$ // X is that the curve of $E_{THz}$ // Z has a deep dip at 8 THz which is absent in the curve of $E_{THz}$ // X. Similar absorption difference due to different compositions between the polarization of electromagnetic wave and crystal axes is reported by Plendl et al.[156]

The frequency of absorption found in THz-TDS of Y-cut quartz doesn't show direct relation with the oscillation frequencies of time-dependent SHG found in THz-

pump/SHG-probe experiment. Thus, other physical processes such as possible hyper-Raman scattering[157] should be considered to explain the oscillations in time-dependent SHG signals.

## 6.5. **CONCLUSION**

In this chapter we carried out THz pump / SHG-probe experiment with quartz. We found that THz pump can activate oscillations in quartz. We also found the SHG generated in quartz increases with increasing power of probe and THz. The spectra of SHG in quartz pumped with THz show greatly enhanced bandwidth and intensity. THz polarization has obvious effect on SHG. THz with polarization parallel to Z axis of Y-cut quartz can trigger intensive oscillations. In Y-cut quartz pumped by THz with polarization parallel to X axis the SHG increases quickly and then relaxes slowly with less intensive oscillations. The power transmission spectrum of Y-cut quartz with $E_{THz}$ // Z has a deep dip at 8 THz which is absent in the case of $E_{THz}$ // X.

# Appendix A

## A1     DATA EXTRACTION

The electric field of THz as a function of time is directly measured through electro-optical sampling. The amplitude and phase of the THz wave in the frequency domain is then obtained through Fourier transformation. Aimed at singling out the sole contribution to the complex refractive index of the ionic liquid from the cell windows, samples of vary thickness were prepared and compared as explained below. For each mixture we measured samples with three different thicknesses.

The complex refractive index can be written as

$$\tilde{n}(v) = n(v) + i\kappa(v), \tag{A6-1}$$

where $v$ is the frequency, $n(v)$ denotes the usual refractive index, and $\kappa(v)$ indicates the extinction coefficient. It is straightforward to demonstrate that the following equations, relating $n(v)$ and $\kappa(v)$ to a variation of the sample thickness $\delta d$, apply in general[158]:

$$n(v) = \frac{\phi(v, d+\delta d) - \phi(v,d)}{2\pi v \delta d} \cdot c + n_0 = \frac{\Delta\phi(v)}{2\pi v \delta d} \cdot c + n_0, \tag{A6-2}$$

$$\kappa(v) = \frac{lnE(v,d) - lnE(v,d+\delta d)}{2\pi v \delta d} \cdot c = \frac{\Delta lnE(v)}{2\pi v \delta d} \cdot c, \tag{A6-3}$$

where $\phi$ and $E$ indicate the phase and amplitude of the THz optical field. $d$ is the thickness of the cell, $c$ is the velocity of light in vacuum, and $n_0$ is the refractive index of air. Both $\phi$ and $E$ are functions of frequency and thickness of the cell. $\Delta\phi$ and $\Delta lnE$ indicate respectively the variations of the phase and of the natural logarithm of $E$ corresponding to a variation of the sample thickness.

Once the complex refractive index is obtained, the complex permittivity can be calculated with the following formula:

$$\tilde{\varepsilon}(v) = \tilde{n}(v)^2. \tag{A6-4}$$

By using some algebra, the relative permittivity $\varepsilon'$ and the dielectric loss $\varepsilon''$ are finally given by the following formulas:

$$\varepsilon'(v) = n(v)^2 - \kappa(v)^2 \,, \qquad\qquad\qquad \text{(A6-5)}$$

$$\varepsilon''(v) = -2n(v)\kappa(v) \,, \qquad\qquad\qquad \text{(A6-6)}$$

After obtaining the complex refractive index, the absorption coefficient can be calculated with the following formula:

$$\alpha(v) = \frac{4 \times \pi \times v}{c} \times \kappa(v) \,. \qquad\qquad\qquad \text{(A7)}$$

## A2     RELATIVE PERMITTIVITY SPECTRA OF 75% AND 25% [C4C1IM]I
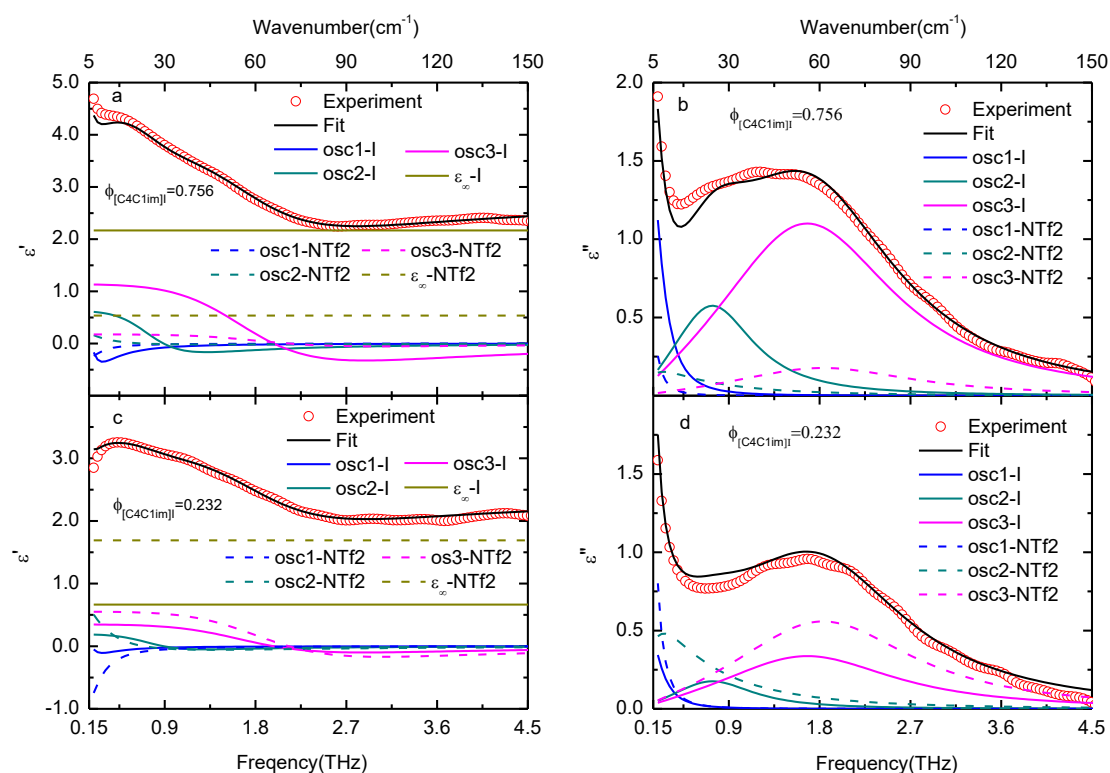


Figure A1. Relative permittivity spectra of the mixtures with a volume fraction [C4C1im]I equal to 75% (a) and 25% (c), and corresponding dielectric loss spectra (b, d). Red open circles represent experimental data. Black solid line is the fitting curve resulting from the overlap of six damped harmonic oscillators found for the two neat components. The single curves of the six oscillators are also shown in the figures with colored solid and dashed lines for neat [C4C1im]I and [C4C1im][NTf2], respectively. The colors are blue, cyan and magenta for the first, second and third oscillator, respectively. The dark yellow solid and dashed line indicates the value of $\varepsilon_\infty$ for neat [C4C1im]I and [C4C1im][NTf2], respectively. Note that the central frequencies do not coincide with the maximum of the resonances since the oscillators are asymmetric.

# Summary and Outlook

In this dissertation we first generally introduced THz technology and then we presented the generation of intensive broadband THz source based on laser induced plasma in air. We also presented THz detection with ZnTe having thickness of 250 μm and 500 μm, 30 μm Z-cut GaSe, LAPC and incoherent detection with air sensor. Then we developed a precise contactless method to measure micro-distance with THz pulse. We investigated the behavior of complex permittivity of ionic liquids mixtures and conducted broadband THz spectroscopy on imidazolium-based ionic liquids. Finally, we conducted THz-pump/second-harmonic-probe experiment in quartz.

In chapter 2 we presented THz source capable of delivering THz pulses having 1 MV/cm peak field amplitude and a ~30 THz bandwidth. We detected the THz pulse with different sensors including ZnTe, GaSe, LAPC and air sensor. The bandwidth detected by 500 μm ZnTe is narrow due to phase mismatch. Effect of absorption of phonon at 5.3 THz is found in detection with 250 μm ZnTe. GaSe is capable of detecting THz up to ~30 THz but the detection in the vicinity around 6.5 THz is negatively affected by phonon modes in the crystal. LAPC is capable of detecting THz up to around 17 THz without any gap.

In chapter 3 we developed a precise contactless micro-distance measurement method using THz pulse. We also compared the ability of PMT and ZnTe to measure micro-distance and found there is nearly no difference between the measurements with ZnTe and PMT when measuring bigger distances. The difference between ZnTe and PMT appears when measuring smaller distances. PMT is capable of measuring distance down to ~20 $\mu m$ due to short and unipolar pulse obtained with PMT. Comparison of distance measurement in nitrogen and in air with ZnTe revealed that reflected THz pulses can be directly shown in nitrogen while additional analysis is necessary to show reflected pulses in air. The comparison between PMT and ZnTe and comparison of ZnTe in nitrogen and air suggest that PMT has the advantages including the ability to measure micro-distance down to ~20 $\mu m$ and immunity to water vaper absorption in air.

In chapter 4, we fitted complex permittivity spectra of all ionic liquid mixtures with a linear combination of damped harmonic oscillators. Single simulation model allows an accurate characterization of the vibration modes present between 0.15 and 4.5. We assigned the lowest-frequency band to rotational or translational motion, and the other two bands to intermolecular or librational motions in ionic liquids. Furthermore, we observed that the complex permittivity obeys a linear mixing law, which can be applied to tune the physicochemical properties of specific mixtures of ionic liquids.

In chapter 5 we found that broad intermolecular vibration band dominants the lowest frequency region. The peak absorption intensity of intermolecular vibration band increases inversely with molecular weight. Unexpected relation between the shift of peak frequency with the ability to form hydrogen bond of anions is found. In addition, an unexpected behavior of the FWHM of intermolecular absorption band versus peak frequency? $?_P$ is also unveiled. The FWHM for ILs with halogen anions is larger than that of ILs with molecular anions. A doublet with peaks located at 6.2 and 6.8 THz and an intense sharp peak at 12.2 THz present in the absorption spectrum of [C4C1im][Ntf2]. The doublet and the intense peak at 12.2 THz origin in the wagging mode of the O-S-O group in the anion. All the refractive index spectra of the investigated ILs have a minimum point whose frequency increases with peak frequency of intermolecular absorption band. Strong intramolecular vibrations in anion of [C4C1im][Ntf2] result in dramatic changes in its refractive index spectrum.

In chapter 6, we observed that THz pump can trigger oscillation in quartz. We also found the intensity of SHG radiated form quartz increases with increasing power of probe and THz. The spectra of SHG in quartz pumped with THz show greatly enhanced bandwidth and intensity. THz polarization has obvious effect on the oscillations of SHG signal. THz polarization has obvious effect on SHG. THz with polarization parallel to Z axis of Y-cut quartz can trigger intensive oscillations. In Y-cut quartz pumped by THz with polarization parallel to X axis the SHG increases quickly and then relaxes slowly with less intensive oscillations. The power transmission spectrum of Y-cut quartz with $E_{THz}$ // Z has a deep dip at 8 THz which is absent in the case of $E_{THz}$ // X.

We already observed some interesting phenomena in both THz-TDS of ionic liquids and THz-pump/SHG-probe experiment of quartz. However, there is still room to improve the experiment. First of all, ultra-broadband THz-TDS is desired to observe more intramolecular vibration in ILs. It is necessary to expand the detected THz band to achieve this aim. There are three prospective methods to expand THz detection band. The first one is to upgrade the air detection method to air biased coherent detection. It is also possible to develop other new broadband THz detection methods such detection with THz induced second harmonic generation in amorphous silicon and detection with laser-poled dye molecules. To understand the physical processes of the oscillations observed in quartz additional experiments are desired.

Furthermore, to understand better the inter- and intra-molecular vibration modes of ILs more data of ILs composed by different kinds of cations and anions are in need. Broadband THz-TDS of other ILs such as pyridinium-based ILs and halometallate ILs are also planned in the future research.

# Acknowledgment

I enjoyed my PhD research experience in the department of University of Naples Federico II. After 3-year study and research I learnt a lot of novel interesting things in my research field and broadened my scientific visions. During my PhD experience I received many supports from professors, friends and my family.

First of all, I would like to express my sincere appreciation to Professor Lorenzo Marrucci for giving me the opportunity to join his outstanding research group and access the cutting edge facilities.

I would like to express my sincere gratitude to Dr. Domenico Paparo for his valuable suggestions, supports and guidance throughout the duration of my research. I would like also to thank Dr. Rubano Andrea for training me with valuable experimental techniques and giving me valuable advices and encouragements. I also thank all the other members of our research group, the visiting students, the bachelor and master students who did their theses in our group.

I would like to thank Professor Salvatore Amoruso for lending me the pump and vacuum chamber to purify ionic liquids and sharing other tools. I also thank Dr. Sam Sudhakaran, Dr. Jijil JJ Nivas and Dr. Elaheh Allahyari for being my best friends. I really enjoyed spending the lunch break together with them. I also enjoyed every talk we had. I am grateful to my flatmates, Dr. Anoop KK, Prof. Yuntao He, Prof. Zhengming Song, Dr. Changbo Song, Dr. Suping Zhao and Mrs. Yachen Wang. I thank as well my friends Dr. Yue Yu, Dr. Shutong He, Dr. Xianghui Kong, Dr. Chengkai Qu, Prof. Shuang Liu and Mrs. Song Zeng for their support and suggestions. I thank my friend Valentina Salviato for her continuous care dating back to my exchange student experience at University of Padova in 2012. I would like also to thank Dr. Xuan Wang for his guidance in my contributions to the activities hold by Chinese Students and Scholars Union in Italy and my other coworkers in Chinese Students and Scholars Union in Italy, Zhiheng Wang, Mr. Jian Xiao and Yaoxuan Xie.

I am very grateful to Mr. Guido Celentano, secretary of physics department of University of Naples Federico II. Mr. Guido Celentano is very kind and helpful to all of

us PhD students and he is always ready to help us whenever we need to obtain documents from government offices.

Finally, I'd like to give my special tanks to my parents, sisters and brother for their endless love, care, sacrifice, encouragement and support. With the care and love from my family I always feel happy in my life and motivated in my work.

# Reference

(1)     Sizov, F.; Rogalski, A., THz detectors. *Progress in Quantum Electronics* **2010,** *34* (5), 278-347.

(2)     Baxter, J. B.; Guglietta, G. W., Terahertz Spectroscopy. *Anal. Chem.* **2011,** *83* (12), 4342-4368.

(3)     Schall, M.; Walther, M.; Uhd Jepsen, P., Fundamental and second-order phonon processes in CdTe and ZnTe. *Phys. Rev. B* **2001,** *64* (9), 094301.

(4)     Ro/nne, C.; Thrane, L.; Åstrand, P.-O.; Wallqvist, A.; Mikkelsen, K. V.; Keiding, S. r. R., Investigation of the temperature dependence of dielectric relaxation in liquid water by THz reflection spectroscopy and molecular dynamics simulation. *J. Chem. Phys.* **1997,** *107* (14), 5319-5331.

(5)     Arikawa, T.; Nagai, M.; Tanaka, K., Characterizing hydration state in solution using terahertz time-domain attenuated total reflection spectroscopy. *Chem. Phys. Lett.* **2008,** *457* (1), 12-17.

(6)     Nagai, M.; Yada, H.; Arikawa, T.; Tanaka, K., Terahertz time-domain attenuated total reflection spectroscopy in water and biological solution. *Int. J. Infrared Milli. Waves* **2006,** *27* (4), 505-515.

(7)     Walther, M.; Fischer, B. M.; Uhd Jepsen, P., Noncovalent intermolecular forces in polycrystalline and amorphous saccharides in the far infrared. *Chem. Phys.* **2003,** *288* (2), 261-268.

(8)     Allis, D. G.; Fedor, A. M.; Korter, T. M.; Bjarnason, J. E.; Brown, E. R., Assignment of the lowest-lying THz absorption signatures in biotin and lactose monohydrate by solid-state density functional theory. *Chem. Phys. Lett.* **2007,** *440* (4), 203-209.

(9)     Korter, T. M.; Plusquellic, D. F., Continuous-wave terahertz spectroscopy of biotin: vibrational anharmonicity in the far-infrared. *Chem. Phys. Lett.* **2004,** *385* (1), 45-51.

(10)    Zhang, H.; Siegrist, K.; Plusquellic, D. F.; Gregurick, S. K., Terahertz Spectra and Normal Mode Analysis of the Crystalline VA Class Dipeptide Nanotubes. *J. Am. Chem. Soc.* **2008,** *130* (52), 17846-17857.

(11)    Beard, M. C.; Turner, G. M.; Schmuttenmaer, C. A., Measuring Intramolecular Charge Transfer via Coherent Generation of THz Radiation. *J. Phys. Chem. A* **2002,** *106* (6), 878-883.

(12)    Groeneveld, R. H. M.; Grischkowskyt, D., Picosecond time-resolved far-infrared experiments on carriers and excitons in GaAs–AlGaAs multiple quantum wells. *J. Opt. Soc. Am. B* **1994,** *11* (12), 2502-2507.

(13)    Kaindl, R. A.; Carnahan, M. A.; Hagele, D.; Lovenich, R.; Chemla, D. S., Ultrafast terahertz probes of transient conducting and insulating phases in an electron-hole gas. *Nature* **2003,** *423* (6941), 734-738.

(14)    Leinß, S.; Kampfrath, T.; v.Volkmann, K.; Wolf, M.; Steiner, J. T.; Kira, M.; Koch, S. W.; Leitenstorfer, A.; Huber, R., Terahertz Coherent Control of Optically Dark Paraexcitons in ${\mathrm{Cu}}_{2}\mathbf{O}$. *Phys. Rev. Lett.* **2008,** *101* (24), 246401.

(15)    Danielson, J. R.; Lee, Y.-S.; Prineas, J. P.; Steiner, J. T.; Kira, M.; Koch, S. W., Interaction of Strong Single-Cycle Terahertz Pulses with Semiconductor Quantum Wells. *Phys. Rev. Lett.* **2007,** *99* (23), 237401.

(16)    Cole, B. E.; Williams, J. B.; King, B. T.; Sherwin, M. S.; Stanley, C. R., Coherent manipulation of semiconductor quantum bits with terahertz radiation. *Nature* **2001,** *410* (6824), 60-63.

(17)    Huber, R.; Tauser, F.; Brodschelm, A.; Bichler, M.; Abstreiter, G.; Leitenstorfer, A., How many-particle interactions develop after ultrafast excitation of an electron-hole plasma. *Nature* **2001,** *414* (6861), 286-289.

(18)    Libon, I. H.; Baumgärtner, S.; Hempel, M.; Hecker, N. E.; Feldmann, J.; Koch, M.; Dawson, P., An optically controllable terahertz filter. *Appl. Phys. Lett.* **2000,** *76* (20), 2821-2823.

(19)    Chatterjee, S.; Grunwald, T.; Köhler, D.; Pierz, K.; Golde, D.; Kira, M.; Koch, S. W., THz measurements of the optical response in a two-dimensional electron gas. *Phys. Status Solidi C* **2009,** *6* (2), 453-456.

(20)    Auston, D. H.; Cheung, K. P.; Smith, P. R., Picosecond photoconducting Hertzian dipoles. *Appl. Phys. Lett.* **1984,** *45* (3), 284-286.

(21)    Kitaeva, G. K., Terahertz generation by means of optical lasers. *Laser Phys. Lett.* **2008,** *5* (8), 559.

Reference

(22)    Vieweg, N.; Mikulics, M.; Scheller, M.; Ezdi, K.; Wilk, R.; Hübers, H. W.; Koch, M., Impact of the contact metallization on the performance of photoconductive THz antennas. *Opt. Express* **2008,** *16* (24), 19695-19705.

(23)    Kasai, S.; Katagiri, T.; Takayanagi, J.; Kawase, K.; Ouchi, T., Reduction of phonon resonant terahertz wave absorption in photoconductive switches using epitaxial layer transfer. *Appl. Phys. Lett.* **2009,** *94* (11), 113505.

(24)    Blanchard, F.; Razzari, L.; Bandulet, H. C.; Sharma, G.; Morandotti, R.; Kieffer, J. C.; Ozaki, T.; Reid, M.; Tiedje, H. F.; Haugen, H. K., et al., Generation of 1.5 µJ single-cycle terahertz pulses by optical rectification from a large aperture ZnTe crystal. *Opt. Express* **2007,** *15* (20), 13212-13220.

(25)    Löffler, T.; Hahn, T.; Thomson, M.; Jacob, F.; Roskos, H. G., Large-area electro-optic ZnTe terahertz emitters. *Opt. Express* **2005,** *13* (14), 5353-5362.

(26)    Schneider, A.; Stillhart, M.; Günter, P., High efficiency generation and detection of terahertz pulses using laser pulses at telecommunication wavelengths. *Opt. Express* **2006,** *14* (12), 5376-5384.

(27)    Takayuki, S.; Takuya, A.; Koji, S.; Hirohisa, U.; Chiko, O.; Kodo, K., Terahertz-Wave Generation Using a 4-Dimethylamino- N -methyl-4-stilbazolium tosylate Crystal Under Intra-Cavity Conditions. *Appl. Phys. Express* **2008,** *1* (4), 042002.

(28)    Kouji, N.; Takumi, A.; Yoshiki, M.; Atsushi, S.; Kazuhiro, A.; Hiromasa, I.; Hiroaki, M., Efficient Terahertz-Wave Generation Using a 4-Dimethylamino- N -methyl-4-stilbazolium Tosylate Pumped by a Dual-Wavelength Neodymium-Doped Yttrium Aluminum Garnet Laser. *Appl. Phys. Express* **2012,** *5* (11), 112401.

(29)    Morris, J. R.; Shen, Y. R., Far-infrared generation by picosecond pulses in electro-optical materials. *Opt. Commun.* **1971,** *3* (2), 81-84.

(30)    Yang, K. H.; Richards, P. L.; Shen, Y. R., Generation of Far‐Infrared Radiation by Picosecond Light Pulses in LiNbO3. *Appl. Phys. Lett.* **1971,** *19* (9), 320-323.

(31)    Hirori, H.; Doi, A.; Blanchard, F.; Tanaka, K., Single-cycle terahertz pulses with amplitudes exceeding 1 MV/cm generated by optical rectification in LiNbO3. *Appl. Phys. Lett.* **2011,** *98* (9), 091106.

(32)    Hoffmann, M. C.; Yeh, K.-L.; Hebling, J.; Nelson, K. A., Efficient terahertz generation by optical rectification at 1035 nm. *Opt. Express* **2007,** *15* (18), 11706-11713.

(33)     Hamster, H.; Sullivan, A.; Gordon, S.; White, W.; Falcone, R. W., Subpicosecond, electromagnetic pulses from intense laser-plasma interaction. *Phys. Rev. Lett.* **1993,** *71* (17), 2725-2728.

(34)     Cook, D. J.; Hochstrasser, R. M., Intense terahertz pulses by four-wave rectification in air. *Opt. Lett.* **2000,** *25* (16), 1210-1212.

(35)     Dai, J.; Karpowicz, N.; Zhang, X. C., Coherent Polarization Control of Terahertz Waves Generated from Two-Color Laser-Induced Gas Plasma. *Phys. Rev. Lett.* **2009,** *103* (2), 023001.

(36)     Kim, K. Y.; Taylor, A. J.; Glownia, J. H.; Rodriguez, G., Coherent control of terahertz supercontinuum generation in ultrafast laser–gas interactions. *Nat. Photon.* **2008,** *2*, 605.

(37)     Rodriguez, G.; Dakovski, G. L., Scaling behavior of ultrafast two-color terahertz generation in plasma gas targets: energy and pressure dependence. *Opt. Express* **2010,** *18* (14), 15130-15143.

(38)     Kress, M.; Löffler, T.; Eden, S.; Thomson, M.; Roskos, H. G., Terahertz-pulse generation by photoionization of air with laser pulses composed of both fundamental and second-harmonic waves. *Opt. Lett.* **2004,** *29* (10), 1120-1122.

(39)     Kim, K. Y.; Glownia, J. H.; Taylor, A. J.; Rodriguez, G., Terahertz emission from ultrafast ionizing air in symmetry-broken laser fields. *Opt. Express* **2007,** *15* (8), 4577-4584.

(40)     Clerici, M.; Peccianti, M.; Schmidt, B. E.; Caspani, L.; Shalaby, M.; Giguère, M.; Lotti, A.; Couairon, A.; Légaré, F.; Ozaki, T., et al., Wavelength Scaling of Terahertz Generation by Gas Ionization. *Phys. Rev. Lett.* **2013,** *110* (25), 253901.

(41)     Jepsen, P. U.; Cooke, D. G.; Koch, M., Terahertz spectroscopy and imaging – Modern techniques and applications. *Laser Photonics Rev.* **2011,** *5* (1), 124-166.

(42)     Constable, E.; Lewis, R. A., Optical parameters of ZnTe determined using continuous-wave terahertz radiation. *J. Appl. Phys.* **2012,** *112* (6), 063104.

(43)     Wu, Q.; Zhang, X. C., Free‐space electro‐optic sampling of terahertz beams. *Appl. Phys. Lett.* **1995,** *67* (24), 3523-3525.

(44)     Jepsen, P. U.; Winnewisser, C.; Schall, M.; Schyja, V.; Keiding, S. R.; Helm, H., Detection of THz pulses by phase retardation in lithium tantalate. *Phys. Rev. E* **1996,** *53* (4), R3052-R3054.

(45)    Nahata, A.; Auston, D. H.; Heinz, T. F.; Wu, C., Coherent detection of freely propagating terahertz radiation by electro‐optic sampling. *Appl. Phys. Lett.* **1996,** *68* (2), 150-152.

(46)    Wu, Q.; Zhang, X. C., Ultrafast electro‐optic field sensors. *Appl. Phys. Lett.* **1996,** *68* (12), 1604-1606.

(47)    Gallot, G.; Zhang, J.; McGowan, R. W.; Jeon, T.-I.; Grischkowsky, D., Measurements of the THz absorption and dispersion of ZnTe and their relevance to the electro-optic detection of THz radiation. *Appl. Phys. Lett.* **1999,** *74* (23), 3450-3452.

(48)    Schall, M.; Jepsen, P. U., Freeze-out of difference-phonon modes in ZnTe and its application in detection of THz pulses. *Appl. Phys. Lett.* **2000,** *77* (18), 2801-2803.

(49)    Wu, Q.; Zhang, X.-C., 7 terahertz broadband GaP electro-optic sensor. *Appl. Phys. Lett.* **1997,** *70* (14), 1784-1786.

(50)    Han, P. Y.; Zhang, X.-C., Coherent, broadband midinfrared terahertz beam sensors. *Appl. Phys. Lett.* **1998,** *73* (21), 3049-3051.

(51)    Huber, R.; Brodschelm, A.; Tauser, F.; Leitenstorfer, A., Generation and field-resolved detection of femtosecond electromagnetic pulses tunable up to 41 THz. *Appl. Phys. Lett.* **2000,** *76* (22), 3191-3193.

(52)    Kübler, C.; Huber, R.; Tübel, S.; Leitenstorfer, A., Ultrabroadband detection of multi-terahertz field transients with GaSe electro-optic sensors: Approaching the near infrared. *Appl. Phys. Lett.* **2004,** *85* (16), 3360-3362.

(53)    Taschin, A.; Bartolini, P.; Tasseva, J.; Torre, R., THz time-domain spectroscopic investigations of thin films. *Measurement* **2017**, https://doi.org/10.1016/j.measurement.2017.05.074.

(54)    Jeon, T.-I.; Grischkowsky, D., Characterization of optically dense, doped semiconductors by reflection THz time domain spectroscopy. *Appl. Phys. Lett.* **1998,** *72* (23), 3032-3034.

(55)    Thrane, L.; Jacobsen, R. H.; Uhd Jepsen, P.; Keiding, S. R., THz reflection spectroscopy of liquid water. *Chem. Phys. Lett.* **1995,** *240* (4), 330-333.

(56)    Hideki, H.; Kumiko, Y.; Masaya, N.; Koichiro, T., Attenuated Total Reflection Spectroscopy in Time Domain Using Terahertz Coherent Pulses. *Jpn. J. Appl. Phys.* **2004,** *43* (10A), L1287.

(57)    Walther, M.; Fischer, B.; Schall, M.; Helm, H.; Jepsen, P. U., Far-infrared vibrational spectra of all-trans, 9-cis and 13-cis retinal measured by THz time-domain spectroscopy. *Chem. Phys. Lett.* **2000,** *332* (3), 389-395.

(58)    Laman, N.; Harsha, S. S.; Grischkowsky, D.; Melinger, J. S., 7 GHz resolution waveguide THz spectroscopy of explosives related solids showing new features. *Opt. Express* **2008,** *16* (6), 4094-4105.

(59)    Huang, Y.; Zhu, L.; Zhao, Q.; Guo, Y.; Ren, Z.; Bai, J.; Xu, X., Surface Optical Rectification from Layered MoS2 Crystal by THz Time-Domain Surface Emission Spectroscopy. *ACS Appl. Mater. Interfaces* **2017,** *9* (5), 4956-4965.

(60)    Hirakawa, K.; Wilke, I.; Yamanaka, K.; Roskos, H. G.; Voßbürger, M.; Wolter, F.; Waschke, C.; Kurz, H.; Grayson, M.; Tsui, D. C., Coherent submillimeter-wave emission from non-equilibrium two-dimensional free carrier plasmas in AlGa/AsGaAs heterojunctions. *Surf. Sci.* **1996,** *361* (Supplement C), 368-371.

(61)    Roskos, H. G.; Nuss, M. C.; Shah, J.; Leo, K.; Miller, D. A. B.; Fox, A. M.; Schmitt-Rink, S.; Köhler, K., Coherent submillimeter-wave emission from charge oscillations in a double-well potential. *Phys. Rev. Lett.* **1992,** *68* (14), 2216-2219.

(62)    Schmuttenmaer, C. A., Exploring Dynamics in the Far-Infrared with Terahertz Spectroscopy. *Chem. Rev.* **2004,** *104* (4), 1759-1780.

(63)    Nuss, M. C.; Auston, D. H.; Capasso, F., Direct Subpicosecond Measurement of Carrier Mobility of Photoexcited Electrons in Gallium Arsenide. *Phys. Rev. Lett.* **1987,** *58* (22), 2355-2358.

(64)    Zielbauer, J.; Wegener, M., Ultrafast optical pump THz‐probe spectroscopy on silicon. *Appl. Phys. Lett.* **1996,** *68* (9), 1223-1225.

(65)    Beard, M. C.; Turner, G. M.; Schmuttenmaer, C. A., Transient photoconductivity in GaAs as measured by time-resolved terahertz spectroscopy. *Phys. Rev. B* **2000,** *62* (23), 15764-15777.

(66)    Averitt, R. D.; Lobad, A. I.; Kwon, C.; Trugman, S. A.; Thorsmølle, V. K.; Taylor, A. J., Ultrafast Conductivity Dynamics in Colossal Magnetoresistance Manganites. *Phys. Rev. Lett.* **2001,** *87* (1), 017401.

(67)    Dai, J.; Xie, X.; Zhang, X. C., Detection of Broadband Terahertz Waves with a Laser-Induced Plasma in Gases. *Phys. Rev. Lett.* **2006,** *97* (10), 103903.

(68)    Karpowicz, N.; Dai, J.; Lu, X.; Chen, Y.; Yamaguchi, M.; Zhao, H.; Zhang, X.-C.; Zhang, L.; Zhang, C.; Price-Gallagher, M., et al., Coherent heterodyne time-domain spectrometry covering the entire "terahertz gap". *Appl. Phys. Lett.* **2008,** *92* (1), 011131.

(69)    Liu, J.; Dai, J.; Chin, S. L.; Zhang, X. C., Broadband terahertz wave remote sensing using coherent manipulation of fluorescence from asymmetrically ionized gases. *Nat. Photon.* **2010,** *4* (9), 627-631.

(70)    Liu, J.; Zhang, X. C., Terahertz-Radiation-Enhanced Emission of Fluorescence from Gas Plasma. *Phys. Rev. Lett.* **2009,** *103* (23), 235002.

(71)    Clough, B.; Liu, J.; Zhang, X. C., Laser-induced photoacoustics influenced by single-cycle terahertz radiation. *Opt. Lett.* **2010,** *35* (21), 3544-3546.

(72)    Wang, T.; Iwaszczuk, K.; Wrisberg, E. A.; Denning, E. V.; Jepsen, P. U., Linearity of Air-Biased Coherent Detection for Terahertz Time-Domain Spectroscopy. *J. Infrared Milli. Terahz. Waves* **2016,** *37* (6), 592-604.

(73)    Kampfrath, T.; Sell, A.; Klatt, G.; Pashkin, A.; Mährlein, S.; Dekorsy, T.; Wolf, M.; Fiebig, M.; Leitenstorfer, A.; Huber, R., Coherent terahertz control of antiferromagnetic spin waves. *Nat. Photon.* **2010,** *5*, 31.

(74)    Luca, G. D.; Rubano, A.; Gennaro, E. d.; Khare, A.; Granozio, F. M.; Uccio, U. S. d.; Marrucci, L.; Paparo, D., Potential-well depth at amorphous-LaAlO3/crystalline-SrTiO3 interfaces measured by optical second harmonic generation. *Appl. Phys. Lett.* **2014,** *104* (26), 261603.

(75)    Sinyukov, A. M.; Hayden, L. M., Efficient Electrooptic Polymers for THz Applications. *J. Phys. Chem. B* **2004,** *108* (25), 8515-8522.

(76)    Zheng, X.; McLaughlin, C. V.; Cunningham, P.; Hayden, L. M., Organic Broadband TeraHertz Sources and Sensors. *J. Nanoelectron. Optoelectron.* **2007,** *2* (1), 58-76.

(77)    Zheng, X.; Sinyukov, A.; Hayden, L. M., Broadband and gap-free response of a terahertz system based on a poled polymer emitter-sensor pair. *Appl. Phys. Lett.* **2005,** *87* (8), 081115.

(78)    Chen, C.-W.; Tang, T.-T.; Lin, S.-H.; Huang, J. Y.; Chang, C.-S.; Chung, P.-K.; Yen, S.-T.; Pan, C.-L., Optical properties and potential applications of ε-GaSe at terahertz frequencies. *J. Opt. Soc. Am. B* **2009,** *26* (9), A58-A65.

(79)    Liu, K.; Xu, J.; Zhang, X.-C., GaSe crystals for broadband terahertz wave detection. *Appl. Phys. Lett.* **2004,** *85* (6), 863-865.

(80)    Berkovic, G.; Shafir, E., Optical methods for distance and displacement measurements. *Adv. Opt. Photon.* **2012,** *4* (4), 441-471.

(81)    Amann, M.-C.; Bosch, T. M.; Lescure, M.; Myllylae, R. A.; Rioux, M. In *Laser ranging: a critical review of unusual techniques for distance measurement*, SPIE: 2001; p 10.

(82)    Alzahrani, K.; Burton, D.; Lilley, F.; Gdeisat, M.; Bezombes, F.; Qudeisat, M., Absolute distance measurement with micrometer accuracy using a Michelson interferometer and the iterative synthetic wavelength principle. *Opt. Express* **2012,** *20* (5), 5658-5682.

(83)    Massa, J. S.; Buller, G. S.; Walker, A. C.; Cova, S.; Umasuthan, M.; Wallace, A. M., Time-of-flight optical ranging system based on time-correlated single-photon counting. *Appl. Opt.* **1998,** *37* (31), 7298-7304.

(84)    Besl, P. J., Active, optical range imaging sensors. *Machine Vis. Apps.* **1988,** *1* (2), 127-152.

(85)    Määttä, K.; Kostamovaara, J.; Myllylä, R., Profiling of hot surfaces by pulsed time-of-flight laser range finder techniques. *Appl. Opt.* **1993,** *32* (27), 5334-5347.

(86)    Hallett, J. P.; Welton, T., Room-Temperature Ionic Liquids: Solvents for Synthesis and Catalysis. 2. *Chem. Rev.* **2011,** *111* (5), 3508-3576.

(87)    Jin, L.; Howlett, P. C.; Pringle, J. M.; Janikowski, J.; Armand, M.; MacFarlane, D. R.; Forsyth, M., An organic ionic plastic crystal electrolyte for rate capability and stability of ambient temperature lithium batteries. *Energy Environ. Sci.* **2014,** *7* (10), 3352-3361.

(88)    Banerjee, A.; Scott, R. W. J., Optimization of transition metal nanoparticle-phosphonium ionic liquid composite catalytic systems for deep hydrogenation and hydrodeoxygenation reactions. *Green Chem.* **2015,** *17* (3), 1597-1604.

(89)    González, R.; Bartolomé, M.; Blanco, D.; Viesca, J. L.; Fernández-González, A.; Battez, A. H., Effectiveness of phosphonium cation-based ionic liquids as lubricant additive. *Tribol. Int.* **2016,** *98*, 82-93.

(90)    Chatel, G.; Pereira, J. F. B.; Debbeti, V.; Wang, H.; Rogers, R. D., Mixing ionic liquids - "simple mixtures" or "double salts"? *Green Chem.* **2014,** *16* (4), 2051-2083.

(91)     Clough, M. T.; Crick, C. R.; Grasvik, J.; Hunt, P. A.; Niedermeyer, H.; Welton, T.; Whitaker, O. P., A physicochemical investigation of ionic liquid mixtures. *Chem. Sci.* **2015,** *6* (2), 1101-1114.

(92)     Diedrichs, A.; Gmehling, J., Measurement of heat capacities of ionic liquids by differential scanning calorimetry. *Fluid Phase Equilib.* **2006,** *244* (1), 68-77.

(93)     Cha, S.; Kim, D., Anion exchange in ionic liquid mixtures. *Phys. Chem. Chem. Phys.* **2015,** *17* (44), 29786-29792.

(94)     Yamada, T.; Tominari, Y.; Tanaka, S.; Mizuno, M., Infrared Spectroscopy of Ionic Liquids Consisting of Imidazolium Cations with Different Alkyl Chain Lengths and Various Halogen or Molecular Anions with and without a Small Amount of Water. *J. Phys. Chem. B* **2017,** *121* (14), 3121-3129.

(95)     Berg, R. W., Raman Spectroscopy and Ab-Initio Model Calculations on Ionic Liquids. *Monatsh. Chem.* **2007,** *138* (11), 1045-1075.

(96)     Hunger, J.; Stoppa, A.; Schrödle, S.; Hefter, G.; Buchner, R., Temperature Dependence of the Dielectric Properties and Dynamics of Ionic Liquids. *ChemPhysChem* **2009,** *10* (4), 723-733.

(97)     Mizoshiri, M.; Nagao, T.; Mizoguchi, Y.; Yao, M., Dielectric permittivity of room temperature ionic liquids: A relation to the polar and nonpolar domain structures. *J. Chem. Phys.* **2010,** *132* (16), 164510.

(98)     Schrödle, S.; Annat, G.; MacFarlane, D. R.; Forsyth, M.; Buchner, R.; Hefter, G., High Frequency Dielectric Response of the Ionic Liquid N-Methyl-N-ethylpyrrolidinium Dicyanamide. *Aust. J. Chem.* **2007,** *60* (1), 6-8.

(99)     Sonnleitner, T.; Turton, D. A.; Hefter, G.; Ortner, A.; Waselikowski, S.; Walther, M.; Wynne, K.; Buchner, R., Ultra-Broadband Dielectric and Optical Kerr-Effect Study of the Ionic Liquids Ethyl and Propylammonium Nitrate. *J. Phys. Chem. B* **2015,** *119* (29), 8826-8841.

(100) Shirota, H., Intermolecular/Interionic Vibrations of 1-Methyl-3-n-octylimidazolium Tetrafluoroborate Ionic Liquid and Benzene Mixtures. *J. Phys. Chem. B* **2013,** *117* (26), 7985-7995.

(101) Xiao, D.; Rajian, J. R.; Hines, L. G.; Li, S.; Bartsch, R. A.; Quitevis, E. L., Nanostructural Organization and Anion Effects in the Optical Kerr Effect Spectra of Binary Ionic Liquid Mixtures. *J. Phys. Chem. B* **2008,** *112* (42), 13316-13325.

(102)   Castner, E. W.; Wishart, J. F.; Shirota, H., Intermolecular Dynamics, Interactions, and Solvation in Ionic Liquids. *Acc. Chem. Res.* **2007,** *40* (11), 1217-1227.

(103)   Xiao, D.; Hines Jr, L. G.; Holtz, M. W.; Song, K.; Bartsch, R. A.; Quitevis, E. L., Effect of cation symmetry on the low-frequency spectra of imidazolium ionic liquids: OKE and Raman spectroscopic measurements and DFT calculations. *Chem. Phys. Lett.* **2010,** *497* (1–3), 37-42.

(104)   Villar-Garcia, I. J.; Lovelock, K. R. J.; Men, S.; Licence, P., Tuning the electronic environment of cations and anions using ionic liquid mixtures. *Chem. Sci.* **2014,** *5* (6), 2573-2579.

(105)   Chakraborty, A.; Inagaki, T.; Banno, M.; Mochida, T.; Tominaga, K., Low-Frequency Spectra of Metallocenium Ionic Liquids Studied by Terahertz Time-Domain Spectroscopy. *J. Phys. Chem. A* **2011,** *115* (8), 1313-1319.

(106)   Wulf, A.; Fumino, K.; Ludwig, R.; Taday, P. F., Combined THz, FIR and Raman Spectroscopy Studies of Imidazolium-Based Ionic Liquids Covering the Frequency Range 2–300 cm−1. *ChemPhysChem* **2010,** *11* (2), 349-353.

(107)   Yamada, T.; Tominari, Y.; Tanaka, S.; Mizuno, M., Terahertz and Infrared Spectroscopy of Room-Temperature Imidazolium-Based Ionic Liquids. *J. Phys. Chem. B* **2015,** *119* (51), 15696-15705.

(108)   Yamada, T.; Tominari, Y.; Tanaka, S.; Mizuno, M.; Fukunaga, K., Vibration Modes at Terahertz and Infrared Frequencies of Ionic Liquids Consisting of an Imidazolium Cation and a Halogen Anion. *Materials* **2014,** *7* (11), 7409.

(109)   Yamamoto, K.; Tani, M.; Hangyo, M., Terahertz Time-Domain Spectroscopy of Imidazolium Ionic Liquids. *J. Phys. Chem. B* **2007,** *111* (18), 4854-4859.

(110)   Almeida, H. F. D.; Canongia Lopes, J. N.; Rebelo, L. P. N.; Coutinho, J. A. P.; Freire, M. G.; Marrucho, I. M., Densities and Viscosities of Mixtures of Two Ionic Liquids Containing a Common Cation. *J. Chem. Eng. Data* **2016,** *61* (8), 2828-2843.

(111)   Koeberg, M.; Wu, C.-C.; Kim, D.; Bonn, M., THz dielectric relaxation of ionic liquid:water mixtures. *Chem. Phys. Lett.* **2007,** *439* (1–3), 60-64.

(112)   Asaki, M. L. T.; Redondo, A.; Zawodzinski, T. A.; Taylor, A. J., Dielectric relaxation and underlying dynamics of acetonitrile and 1-ethyl-3-methylimidazolium triflate mixtures using THz transmission spectroscopy. *J. Chem. Phys.* **2002,** *116* (23), 10377-10385.

(113)   Fumino, K.; Bonsa, A.-M.; Golub, B.; Paschek, D.; Ludwig, R., Non-Ideal Mixing Behaviour of Hydrogen Bonding in Mixtures of Protic Ionic Liquids. *ChemPhysChem* **2015,** *16* (2), 299-304.

(114)   Stoppa, A.; Buchner, R.; Hefter, G., How ideal are binary mixtures of room-temperature ionic liquids? *J. Mol. Liq.* **2010,** *153* (1), 46-51.

(115)   Sengwa, R. J.; Choudhary, S.; Khatri, V., Microwave dielectric spectra and molecular relaxation in formamide–N,N-dimethylformamide binary mixtures. *Spectrochim. Acta A: Mol. Biomol. Spectrosc.* **2011,** *82* (1), 279-282.

(116)   Jouyban, A.; Soltanpour, S.; Chan, H.-K., A simple relationship between dielectric constant of mixed solvents with solvent composition and temperature. *Int. J. Pharm.* **2004,** *269* (2), 353-360.

(117)   Buep, A. H., Dielectric properties of binary systems 10. Ideal dielectric behavior and excess dielectric properties. *J. Mol. Liq.* **1992,** *51* (3–4), 279-306.

(118)   Buep, A. H.; Baron, M., Dielectric properties of binary systems. 7. Carbon tetrachloride with benzene, with toluene, and with p-xylene at 298.15 and 308.15 K. *J. Phys. Chem.* **1988,** *92* (3), 840-843.

(119)   Rivas, M. A.; Iglesias, T. P., On permittivity and density of the systems (tetraglyme + dimethyl or diethyl carbonate) and the formulation of Δε in terms of volume or mole fraction. *J. Chem. Thermodyn.* **2007,** *39* (12), 1546-1556.

(120)   Rivas, M. A.; Iglesias, T. P., On permittivity and density of the systems {triglyme + (dimethyl or diethyl carbonate)} and formulation of Δε in terms of volume or mole fraction. *J. Chem. Thermodyn.* **2008,** *40* (7), 1120-1130.

(121)   BUEP, A. H., Dielectric properties of liquid systems: the ideal complex permittivity in liquid mixtures. *Turk. J. Phys.* **2010,** *33* (5), 243-248.

(122)   Iglesias, T. P.; Reis, J. C. R.; Fariña-Busto, L., On the definition of the excess permittivity of a fluid mixture. II. *J. Chem. Thermodyn.* **2008,** *40* (9), 1475-1476.

(123)   Reis, J. C. R.; Iglesias, T. P.; Douheret, G.; Davis, M. I., The permittivity of thermodynamically ideal liquid mixtures and the excess relative permittivity of binary dielectrics. *Phys. Chem. Chem. Phys.* **2009,** *11* (20), 3977-3986.

(124)   Bosch, S.; Ferré-Borrull, J.; Leinfellner, N.; Canillas, A., Effective dielectric function of mixtures of three or more materials: a numerical procedure for computations. *Surf. Sci.* **2000,** *453* (1–3), 9-17.

(125)   Sihvola, A. H.; Kong, J. A., Effective permittivity of dielectric mixtures. *IEEE Trans. Geosci. Remote Sens.* **1988,** *26* (4), 420-429.

(126)   Xiao, D.; Rajian, J. R.; Li, S.; Bartsch, R. A.; Quitevis, E. L., Additivity in the Optical Kerr Effect Spectra of Binary Ionic Liquid Mixtures: Implications for Nanostructural Organization. *J. Phys. Chem. B* **2006,** *110* (33), 16174-16178.

(127)   Fumino, K.; Stange, P.; Fossog, V.; Hempelmann, R.; Ludwig, R., Equilibrium of Contact and Solvent-Separated Ion Pairs in Mixtures of Protic Ionic Liquids and Molecular Solvents Controlled by Polarity. *Angew. Chem. Int. Ed.* **2013,** *52* (47), 12439-12442.

(128)   Turton, D. A.; Hunger, J.; Stoppa, A.; Hefter, G.; Thoman, A.; Walther, M.; Buchner, R.; Wynne, K., Dynamics of Imidazolium Ionic Liquids from a Combined Dielectric Relaxation and Optical Kerr Effect Study: Evidence for Mesoscopic Aggregation. *J. Am. Chem. Soc.* **2009,** *131* (31), 11140-11146.

(129)   Giraud, G.; Gordon, C. M.; Dunkin, I. R.; Wynne, K., The effects of anion and cation substitution on the ultrafast solvent dynamics of ionic liquids: A time-resolved optical Kerr-effect spectroscopic study. *J. Chem. Phys.* **2003,** *119* (1), 464-477.

(130)   Sonnleitner, T.; Turton, D. A.; Waselikowski, S.; Hunger, J.; Stoppa, A.; Walther, M.; Wynne, K.; Buchner, R., Dynamics of RTILs: A comparative dielectric and OKE study. *J. Mol. Liq.* **2014,** *192*, 19-25.

(131)   Xiao, D.; Rajian, J. R.; Cady, A.; Li, S.; Bartsch, R. A.; Quitevis, E. L., Nanostructural Organization and Anion Effects on the Temperature Dependence of the Optical Kerr Effect Spectra of Ionic Liquids. *J. Phys. Chem. B* **2007,** *111* (18), 4669-4677.

(132)   Stoppa, A.; Hunger, J.; Buchner, R.; Hefter, G.; Thoman, A.; Helm, H., Interactions and Dynamics in Ionic Liquids. *J. Phys. Chem. B* **2008,** *112* (16), 4854-4858.

(133)   Jeon, Y.; Sung, J.; Seo, C.; Lim, H.; Cheong, H.; Kang, M.; Moon, B.; Ouchi, Y.; Kim, D., Structures of Ionic Liquids with Different Anions Studied by Infrared Vibration Spectroscopy. *J. Phys. Chem. B* **2008,** *112* (15), 4735-4740.

(134)   Hayashi, S.; Ozawa, R.; Hamaguchi, H.-o., Raman Spectra, Crystal Polymorphism, and Structure of a Prototype Ionic-liquid [bmim]Cl. *Chem. Lett.* **2003,** *32* (6), 498-499.

(135)   Saha, S.; Hayashi, S.; Kobayashi, A.; Hamaguchi, H.-o., Crystal Structure of 1-Butyl-3-methylimidazolium Chloride. A Clue to the Elucidation of the Ionic Liquid Structure. *Chem. Lett.* **2003,** *32* (8), 740-741.

(136)   Holbrey, J. D.; Reichert, W. M.; Nieuwenhuyzen, M.; Johnson, S.; Seddon, K. R.; Rogers, R. D., Crystal polymorphism in 1-butyl-3-methylimidazolium halides: supporting ionic liquid formation by inhibition of crystallization. *Chem. Commun.* **2003**, 10.1039/B304543A (14), 1636-1637.

(137)   Katayanagi, H.; Hayashi, S.; Hamaguchi, H.-o.; Nishikawa, K., Structure of an ionic liquid, 1-n-butyl-3-methylimidazolium iodide, studied by wide-angle X-ray scattering and Raman spectroscopy. *Chem. Phys. Lett.* **2004,** *392* (4–6), 460-464.

(138)   Chiappe, C., Nanostructural Organization of Ionic Liquids: Theoretical and Experimental Evidences of the Presence of Well Defined Local Structures in Ionic Liquids. *Monatsh. Chem.* **2007,** *138* (11), 1035-1043.

(139)   Fumino, K.; Wulf, A.; Ludwig, R., The Cation–Anion Interaction in Ionic Liquids Probed by Far-Infrared Spectroscopy. *Angew. Chem. Int. Ed.* **2008,** *47* (20), 3830-3834.

(140)   Fumino, K.; Reichert, E.; Wittler, K.; Hempelmann, R.; Ludwig, R., Low-Frequency Vibrational Modes of Protic Molten Salts and Ionic Liquids: Detecting and Quantifying Hydrogen Bonds. *Angew. Chem. Int. Ed.* **2012,** *51* (25), 6236-6240.

(141)   Buffeteau, T.; Grondin, J.; Danten, Y.; Lassègues, J.-C., Imidazolium-Based Ionic Liquids: Quantitative Aspects in the Far-Infrared Region. *J. Phys. Chem. B* **2010,** *114* (22), 7587-7592.

(142)   Mou, S.; Rubano, A.; Paparo, D., Complex Permittivity of Ionic Liquid Mixtures Investigated by Terahertz Time-Domain Spectroscopy. *J. Phys. Chem. B* **2017,** *121* (30), 7351-7358.

(143)   Fumino, K.; Wulf, A.; Ludwig, R., Strong, Localized, and Directional Hydrogen Bonds Fluidize Ionic Liquids. *Angew. Chem. Int. Ed.* **2008,** *47* (45), 8731-8734.

(144)   Wulf, A.; Fumino, K.; Ludwig, R., Spectroscopic Evidence for an Enhanced Anion–Cation Interaction from Hydrogen Bonding in Pure Imidazolium Ionic Liquids. *Angew. Chem. Int. Ed.* **2010,** *49* (2), 449-453.

(145)   Paschoal, V. H.; Faria, L. F. O.; Ribeiro, M. C. C., Vibrational Spectroscopy of Ionic Liquids. *Chem. Rev.* **2017,** *117* (10), 7053-7112.

(146)    Heimer, N. E.; Del Sesto, R. E.; Meng, Z.; Wilkes, J. S.; Carper, W. R., Vibrational spectra of imidazolium tetrafluoroborate ionic liquids. *J. Mol. Liq.* **2006,** *124* (1), 84-95.

(147)    Carper, W. R.; Langenwalter, K.; Nooruddin, N. S.; Kullman, M. J.; Gerhard, D.; Wasserscheid, P., Aggregation Models of Potential Cyclical Trimethylsulfonium Dicyanamide Ionic Liquid Clusters. *J. Phys. Chem. B* **2009,** *113* (7), 2031-2041.

(148)    Fumino, K.; Fossog, V.; Wittler, K.; Hempelmann, R.; Ludwig, R., Dissecting Anion–Cation Interaction Energies in Protic Ionic Liquids. *Angew. Chem. Int. Ed.* **2013,** *52* (8), 2368-2372.

(149)    Shirota, H.; Castner, E. W., Physical Properties and Intermolecular Dynamics of an Ionic Liquid Compared with Its Isoelectronic Neutral Binary Solution. *J. Phys. Chem. A* **2005,** *109* (42), 9388-9392.

(150)    Wald, H.; Seidel, P.; Tonouchi, M., Pump-and-probe terahertz method to investigate YBa2Cu3O7−δ thin films. *Phys. C* **2002,** *367* (1), 308-316.

(151)    Shi, Y.-L.; Zhou, Q.-L.; Zhang, C.-L., Transient surface photoconductivity of GaAs emitter studied by terahertz pump-emission spectroscopy. *Chinese Phys. B* **2009,** *18* (10), 4515.

(152)    Li, G.; Xue, X.; Lin, X.; Yuan, S.; Tang, N.; Chu, F.; Cui, H.; Ma, G., Evolution of terahertz conductivity in ZnSe nanocrystal investigated with optical-pump terahertz-probe spectroscopy. *Appl. Phys. A* **2014,** *116* (1), 45-50.

(153)    Thompson, Z. J.; Stickel, A.; Jeong, Y.-G.; Han, S.; Son, B. H.; Paul, M. J.; Lee, B.; Mousavian, A.; Seo, G.; Kim, H.-T., et al., Terahertz-Triggered Phase Transition and Hysteresis Narrowing in a Nanoantenna Patterned Vanadium Dioxide Film. *Nano Lett.* **2015,** *15* (9), 5893-5898.

(154)    Bowlan, P.; Bowlan, J.; Trugman, S. A.; Valdés Aguilar, R.; Qi, J.; Liu, X.; Furdyna, J.; Dobrowolska, M.; Taylor, A. J.; Yarotski, D. A., et al., Probing and controlling terahertz-driven structural dynamics with surface sensitivity. *Optica* **2017,** *4* (3), 383-387.

(155)    Baierl, S.; Mentink, J. H.; Hohenleutner, M.; Braun, L.; Do, T. M.; Lange, C.; Sell, A.; Fiebig, M.; Woltersdorf, G.; Kampfrath, T., et al., Terahertz-Driven Nonlinear Spin Response of Antiferromagnetic Nickel Oxide. *Phys. Rev. Lett.* **2016,** *117* (19), 197201.

(156)    Plendl, J. N.; Mansur, L. C.; Hadni, A.; Brehat, F.; Henry, P.; Morlot, G.; Naudin, F.; Strimer, P., Low temperature far infrared spectra of SiO2 polymorphs. *J. Phys. Chem. Solids* **1967,** *28* (8), 1589-1597.

(157)    Denisov, V. N.; Mavrin, B. N.; Podobedov, V. B., Hyper-Raman scattering by vibrational excitations in crystals, glasses and liquids. *Phys. Rep.* **1987,** *151* (1), 1-92.

(158)    Tielrooij, K. J.; Paparo, D.; Piatkowski, L.; Bakker, H. J.; Bonn, M., Dielectric Relaxation Dynamics of Water in Model Membranes Probed by Terahertz Spectroscopy. *Biophys. J.* **2009,** *97* (9), 2484-2492.